The Relationship between Hemodynamics and Intracranial Carotid Artery Calcification: A Pilot Computational Study

Paris Celie

Delft University of Technology

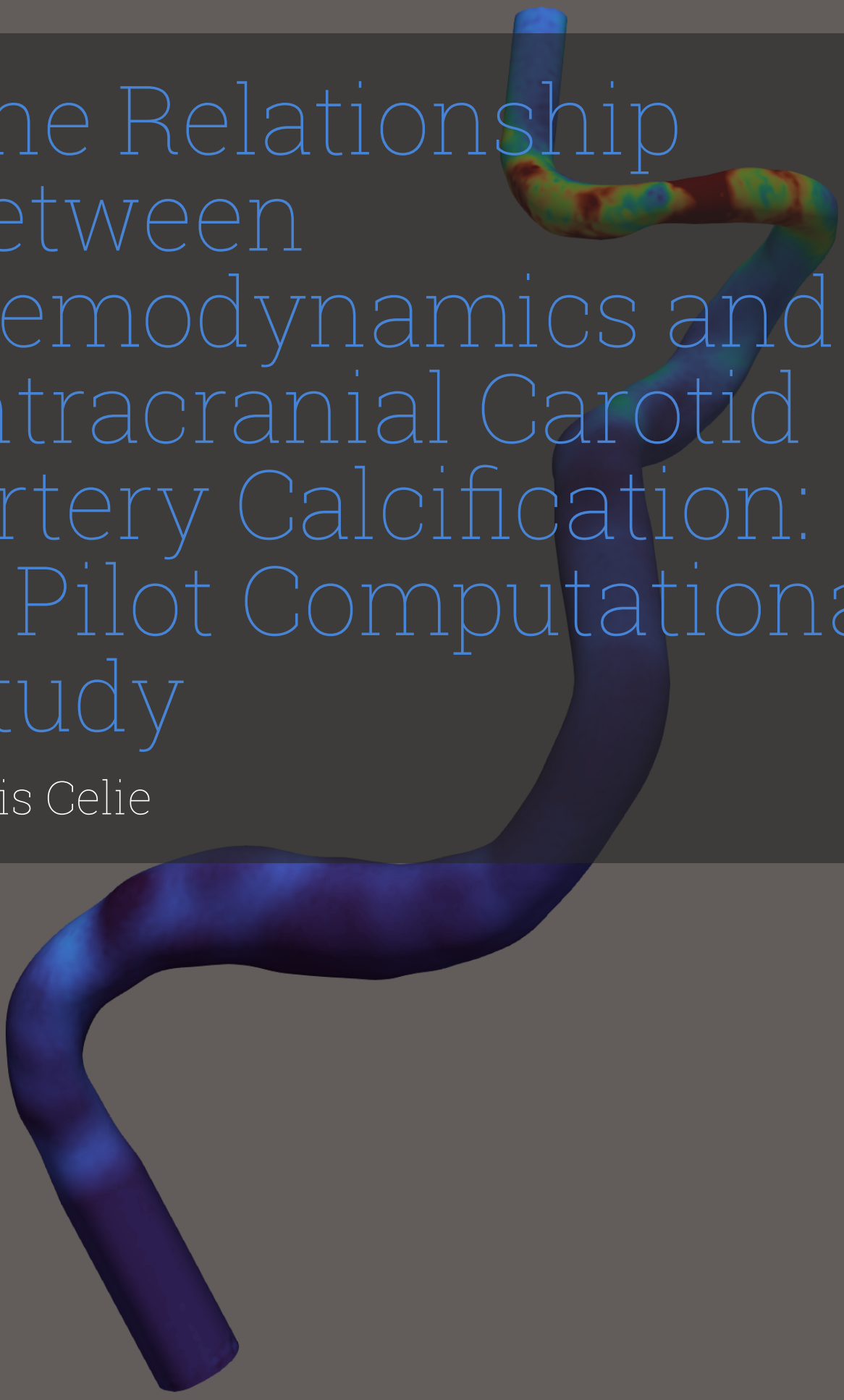

TU Delft

The Relationship between Hemodynamics and Intracranial Carotid Artery Calcification: A Pilot Computational Study

by

Paris Celie

In partial fulfilment of the requirements of
Master of Science in Biomedical Engineering, Track Medical Devices
at the Delft University of Technology, to be defended publicly on Tuesday June 9, 2026 at 14:00

Assessment committee

Chair:	A. Akylidiz
Members:	F. Fontana
	S. Pirola

Supervisors

Daily supervisor:	F. Fontana
Responsible supervisor:	A. Akyildiz
Date:	June, 2026
Faculty:	Faculty of Mechanical Engineering, Delft

TU Delft

Abstract

Background: Intracranial carotid artery calcification (ICAC) is associated with an increased risk of stroke, dementia, and cognitive decline. While disturbed hemodynamics have been linked to vascular pathologies such as atherosclerosis, a potential association with the development of ICAC has not been extensively studied yet. This pilot computational study investigated whether local hemodynamic parameters are associated with areas prone to develop calcification in the intracranial internal carotid artery (ICA).

Methods: Computed tomography angiography (CTA) data from the Erasmus Stroke Study database were used to reconstruct pre-calcification luminal geometries of intracranial carotid arteries. Twenty-three arteries with a stenosis degree $\geq 70\%$ were initially selected. Eight representative arteries were chosen for lumen reconstruction, which were comparable to the stenosed subset in terms of size and calcium burden. Reconstructions were realised using contour rescaling, interpolation, and contour-copying techniques. Computational fluid dynamics simulations were performed in reconstructed healthy lumen models using FEBio. Time-averaged wall shear stress (TAWSS), oscillatory shear index (OSI), and relative residence time (RRT) were calculated and mapped onto two-dimensional vessel representations. The hemodynamic parameters were compared between calcium-containing and calcium-free regions and across anatomical ICA segments (C2–C6).

Results: Simulations of six reconstructed arteries successfully converged to a solution. In these arteries, calcifications were predominantly located in the cavernous (C4) and clinoid segments (C5), while no calcifications were observed in the petrous segment (C2). Calcium-containing regions demonstrated a higher median TAWSS of 2.76 (IQR 2.48 – 3.34) Pa, compared to a median of 1.98 (IQR 1.23 – 2.63) Pa in calcium-free regions, corresponding to a 39.6% percentage change. In contrast, OSI and RRT were generally lower in calcium-containing regions. Calcium-containing regions had a median RRT of 0.43 (IQR 0.36 – 0.48), compared to a median RRT of 0.57 (IQR 0.45 – 0.88) in calcium-free regions. The median OSI was 0.74 x 10^{-3} (IQR 0.48 – 0.011 x 10^{-3}) in calcium-containing regions, while a value of 0.96 x 10^{-3} (IQR 0.72 – 1.1 x 10^{-3}) was found in the calcium-free regions. Segmental analysis showed that TAWSS increased towards the distal ICA segments, whereas RRT decreased downstream. The OSI values remained consistently low throughout the arteries.

Conclusions: This pilot study offers a pipeline to extract hemodynamic data from healthy ICA surrogates, derived from commonly available CTA images of patients with ICAC. The exploratory findings differed from classical atheroprone hemodynamic patterns characterised by low TAWSS, high OSI and low RRT. The contradictory results warrant further investigation. Larger studies with patient-specific boundary conditions are needed to further clarify a potential relationship between hemodynamics and ICAC.

Keywords: Intracranial carotid artery calcification; Computational fluid dynamics; Hemodynamics; Wall shear stress; Stroke; Cerebrovascular disease

Acknowledgements

With a bachelors degree on a topic that has a lot to do with the human body, but little with computational fluid dynamics, programming or discretisation meshes, I knew this thesis was going to be a challenge. In the end, I think it came together quite well. However, this would not have been possible without the support of the following people, who I would therefore like to express my thanks to.

First and foremost, I would like to thank my supervisors Federica and Ali for their invaluable insights and advice throughout my thesis project.
Federica, thank you for your time and dedication to spend almost every Tuesday morning on the meetings we had. Your guidance has helped me through this project and has led me in the right direction. I sometimes felt lost in all the new information I had to understand and process for this project. Luckily, I could rely on your guidance, which made some of the intimidating tasks more manageable. I have learned a lot from you and I hope that my thesis could help you with your own work, or at least inspire you in a way. I wish you all the best with the finalisation of your PhD!
Ali, thank you for taking the time to guide me and for providing your view on the project. Your suggestions were always helpful and gave me another way of thinking about some of the hurdles I encountered. You came up with solutions that felt refreshing to me. I valued the meetings with you highly, as you always reminded me to look at the bigger picture and take time to think about the project as a whole. This helped me to stay on track and work towards the thesis goal.

Secondly, I would like to thank my family, for supporting me throughout this project. You were always keen to hear about my project and supported me whenever I doubted my progress. Sometimes I felt a bit unsure about the management of this project, but thanks to your advice I knew how to move forward from such moments.

I would also like to thank my friends, especially Elisa, Noud and Tycho, with whom I could discuss my ups and downs during this project. Although we were working on our own projects, it was always nice to study together at our beloved 2wi. Studying together has helped me a lot to stay focussed and keep going. Special thanks to Noud, for brainstorming with me whenever I got stuck on a topic, your ideas and input were of great use.

Lastly, I would like to thank Hajo for being there whenever I needed it and assuring me that I was going to be fine. I know the topics of my thesis were sometimes a bit too niche, but thank you for listening to me about calcium, arteries and shear for the duration of this project.

Paris Celie
Delft, June 2026

Contents

List of Figures

List of Tables

Nomenclature

Abbreviations

Abbreviation	Definition
ACA	Anterior cerebral artery
CFD	Computational fluid dynamics
CFL	Courant–Friedrichs–Lewy
CTA	Computed tomography angiography
CCA	Common carotid artery
DM	Diabetes mellitus
EC	Endothelial cell
ESS	Erasmus Stroke Study
ICA	Internal carotid artery
ICAC	Intracranial carotid artery calcification
IEL	Internal elastic lamina
IMT	Intima-media thickness
IQR	Interquartile range
MCA	Middle cerebral artery
MRI	Magnetic resonance imaging
NO	Nitric oxide
OSI	Oscillatory shear index
RRT	Relative residence time
SD	Standard deviation
TAWSS	Time-averaged wall shear stress
VSMC	Vascular smooth muscle cell
WSS	Wall shear stress

Anatomical segments ICA

Segment	Name
C1	Cervical segment
C2	Petrous segment
C3	Lacerum segment
C4	Cavernous segment
C5	Clinoid segment
C6	Ophthalmic segment
C7	Communicating segment

Symbols

Symbol	Definition	Unit
P	Pressure	Pa
Q	Flow rate	m^3/s
R	Flow resistance	kg/m^4s
T	Duration of one cardiac cycle	s
v	Velocity	m/s
y	Distance from lumen centerline to arterial wall	m
κ	Bulk modulus	Pa
μ	Viscosity	Pa·s
ρ	Density	kg/m^3
$\vec{\tau}_w$	Wall shear stress vector	Pa
u	Axial component of the velocity vector	m/s

1

Introduction

1.1. Intracrancial carotid artery calcification

Arteriosclerosis of the intracranial arteries has been shown to negatively affect cognitive performance and to increase dementia risk [9][12]. Dementia results in difficulties with memory, problem-solving, language, and attention, and in a progressive stage, even the inability to perform daily tasks. Unfortunately, a person who lives from age 70 to age 80 with Alzheimer's dementia will spend an average of 40% of this time in the progressive stage. This means that the person is dependent on caregivers and that most of this time will be spent in a nursing home[3].

A specific manifestation of intracranial arteriosclerosis is intracranial carotid artery calcification (ICAC). As its name implies, ICAC is located in the intracranial part of the internal carotid artery (ICA). It involves the deposition of calcium within the vessel wall, resulting in calcified structures. In a cohort study of 2339 stroke-free and dementia-free participants, the presence of ICAC was associated with an increased risk of dementia[9]. In addition to its association with cognitive decline, ICAC has also been linked to cerebrovascular events. Bos et al. [13] performed a population-based cohort study and found that 75% of strokes were related to ICAC. Moreover, stroke risk increased with larger ICAC volumes. Since both stroke and dementia are associated with calcification of the intracranial arteries, substantial health benefits may be gained from preventing or treating ICAC.

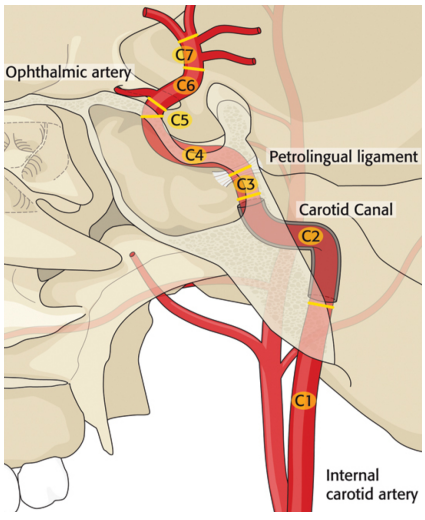

Figure 1.1: The internal carotid artery and the seven distinct segments highlighted in yellow. The segments as classified by Bouthillier originate at C1 and terminate at the bifurcation of segment C7. The segments are knows as the cervical (C1), petrous (C2), lacerum (C3), cavernous (C4), clinoid (C5), ophtalmic (C6), and communicating (C7) segments. The intracranial portion of the ICA begins at the petrous segment. Adapted from [35].

Shown in Figure 1.1, the ICA is an artery with a distinct shape consisting of multiple curved segments. Based on the various curves and the surrounding tissues, parts of the ICA have been categorised into seven anatomical segments, according to the Bouthillier classification [15]. The first segment is extracranial and is called the cervical segment (C1). After C1, the petrous segment (C2), located within the carotid canal of the temporal bone, follows. The lacerum segment (C3) is a short section, followed by the cavernous segment (C4). This segment is located within a highly curved region of the ICA, which has also been referred to as the carotid siphon. After C4, the ICA continues into the clinoid (C5), the ophtalmic (C6) and the communicating segment (C7). The communicating segment terminates at a bifurcation, from which the ICA supplies the anterior cerebral artery (ACA) and the middle cerebral artery (MCA), which together perfuse large regions of the brain.

When ICAC is present, calcified structures can be found within different layers of the vessel wall. Calcifications have been observed in the intima, media, the internal elastic lamina(IEL), and adventitia. The intimal subtype is generally considered a consequence of atherosclerosis and is characterised by progressive atherosclerotic lesions, eccentric plaques, and luminal stenosis[60] [22]. Shown in Figure 1.2, the eccentric arterial plaques associated with intimal calcification only affect one side of the vessel wall, leaving the opposite side unaffected. In contrast, the medial and IEL subtypes are less closely associated with atherosclerosis and are characterised by concentric calcifications. Concentric calcifications are evenly distributed along the entire circumference of the vessel wall, resulting in a uniform narrowing of the arterial lumen. Van den Beukel et al. investigated the intimal and IEL-based morphological subtypes in patients with intracranial ICA calcifications. They found that the IEL-related subtype was most prevalent and associated with the highest stroke risk[55].

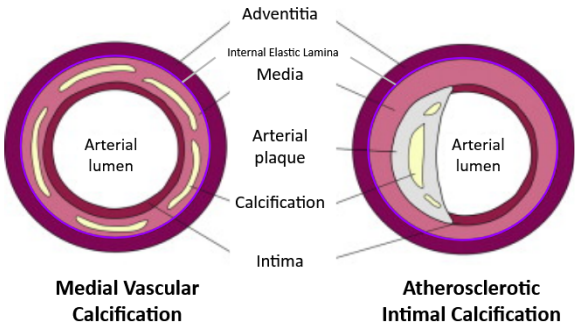

Figure 1.2: Two subtypes of arterial calcification. Medial vascular calcification is characterised by the deposition of calcium within the media, resulting in concentric calcification. Intimal calcification can be distinguished by calcified bodies within an atherosclerotic plaque located between the intima and the media. Adapted from [10].

1.2. Hemodynamics as a biomarker

Risk factors have been established that influence the onset of vascular diseases and related morbidities. Bos et al. identified risk factors for ICAC using patient data from the population-based Rotterdam Study [14]. They found that the prevalence of ICAC increased with age. In men, risk factors for ICAC were excessive alcohol intake and smoking, whereas Diabetes Mellitus (DM) and hypertension were strong risk factors in women. Different risk factors between the intimal and medial types of ICAC have been presented by Vos et al.[57]. While both subtypes were associated with age, pulse pressure and positive family history, only the medial subtype was associated with DM and previous vascular disease. Following the association between calcifications and age, the likelihood of calcifications increases when people get older. An early-biomarker, specific to ICAC, would aid in identifying people at risk before symptoms such as cognitive decline occur. This means that such a biomarker should be measurable before calcifications have been completely developed.

A potential biomarker for diseases of the intracranial arteries might be found in hemodynamics and its influence on vessel wall properties. Parameters involved in hemodynamics include blood flow, velocity profiles, and wall shear stress (WSS). Multiple in vitro studies have shown that disturbed and slow flow has an effect on the endothelial cells that form the inner layer of the arterial wall. Low shear stress disrupts endothelial alignment and function, leading to increased endothelial permeability, upregulation of adhesion molecules, and pro-inflammatory gene expression. These changes induce chronic inflam-

mation and lipid accumulation, which promotes plaque formation and progression [37]. In addition to its link to plaque formation, disruption of the endothelium has been associated with vascular calcification. Xu et al. highlighted the close interplay between endothelial cells and vascular smooth muscle cells (VSMCs). The medial layer of the arterial wall is composed of VSMCs, which role is to maintain the blood flow and pressure. In response to an altered hemodynamic environment, ECs transmit biochemical signals to VSMCs through intercellular crosstalk. This promotes an osteogenic transformation which supports vascular calcification [59].

From the WSS, other biomechanical markers can be derived, such as the time-averaged wall shear stress (TAWSS), the oscillatory shear index (OSI), and the relative residence time (RRT). These markers have been shown meaningful to quantify disturbed blood flow and its impact on the vessel wall. In the extracranial portion of the carotid artery, correlations have already been reported between atherosclerotic development and shear stress. For example, a cohort study of 48 participants investigated endothelial shear stress and plaque development at the common carotid artery (CCA) twelve years apart. Their findings showed that aging-related reduction of the shear stress independently predicted atherosclerosis development[16]. In addition, early findings by Gnasso et al. revealed a relation between intima-media thickness (IMT) and WSS at the CCA, which were inversely related[25]. Finally, results by Gallo et al. point out that an increased oscillatory shear index(OSI) is an early independent marker of atherosclerotic changes leading to intimal thickening at the carotid sinus[24]. Such studies show the potential of hemodynamic variables for the prediction of arterial wall thickening. However, most research has focused on atherosclerotic wall thickening in relation to hemodynamics at the extracranial portion of the carotid arteries. Studies on a potential role for hemodynamics in the onset of calcifications in the intracranial portion of the ICA are scarce.

Thus, to reveal whether hemodynamics are associated with ICAC, more research is necessary. To examine a possible connection between hemodynamics and ICAC, hemodynamic parameters should be quantified. Some hemodynamic parameters can be directly derived from in vivo measurements. Magnetic resonance imaging (MRI) allows for the measurement and visualisation of flow profiles and blood velocity in vivo. Using these values, the WSS and other shear stress-related parameters can be determined. Another possibility to investigate hemodynamics is through in silico studies, using computational fluid dynamics (CFD). With CFD, blood flow can be simulated in computational models derived from patient imaging data. 2D imaging data, such as images produced by computed tomography angiography (CTA), can be used to build the geometry of the desired artery. This model is then used to perform simulations of the blood flow, which allows for measurement of blood velocity, WSS, and flow patterns. When using CFD to study blood flow, the vascular wall is not incorporated into the model and only the fluid domain is modelled. To aid in the analysis, the assumption is made that the wall can be considered rigid. This implies that any form of force will not lead to deformation of the imaginary vascular wall. Without deformation, the lumen shape remains consistent at any moment of the simulation. Although this approach does not completely resemble the physiological effects, it has been shown that CFD analyses show similar results for the WSS when compared to MRI measurements [19].

1.3. Thesis goal

Currently, the amount of research on ICAC in relation to hemodynamics is limited. While multiple studies have investigated the relation between early wall thickening at the ICA and hemodynamics, most of them focussed on the extracranial portion, such as the ICA bifurcation. In addition, those studies related hemodynamics to atherosclerosis, and not calcifications specifically[49] [24]. Concerning the intracranial vasculature, various studies have examined the relation between the MCA and intracranial atherosclerotic disease. These studies often reported the hemodynamics in areas where stenoses were already present [18] [58]. A study on developing plaques and hemodynamics at the MCA has been performed [17], but similar to the aforementioned papers, this study only evaluated atherosclerotic disease.

Since the relation between hemodynamic parameters and ICAC is not yet widely investigated, this thesis explored a possible connection. To achieve this, a pipeline was developed to compute CFD simulations in the internal carotid artery of high-risk patients. The hemodynamic parameters were studied in areas where calcifications were known to develop. To specify the goal of the thesis, a research question was formulated:

To what extent are hemodynamic parameters, such as blood flow and properties related to wall shear stress, associated with the presence of ICAC?

2

Methods

2.1. Imaging data acquisition

Geometry data of calcified intracranial carotid arteries was retrieved from the Erasmus Stroke Study (ESS) database. The ESS is a clinical registry study of patients with neurovascular disease admitted to the Erasmus University Medical Center in Rotterdam, the Netherlands. Between 2005 and 2010, 943 patients were included. These patients presented with an ischemic stroke (n = 561) or a transient ischemic attack (n = 382). All patients had undergone CTA imaging of the intracranial carotid arteries as part of routine clinical care [7].

Berghout et al. [8] performed segmentation on the CTA images of 50 patients from the ESS registry. Reconstructions were completed for the left and right arteries for each patient, resulting in segmented lumen and calcium data of 100 arteries in total. In addition, the morphometry of the calcifications was studied. The data from the analyses was available for this thesis. Geometry data included maximum and minimum lumen diameters, the length of the segments C2 up to C6, and the tortuosity of each segment. Calcifications were present for all arteries, with stenosis ratios ranging from minimal to severe (10 – 90% of lumen area reduction). Data regarding the calcified bodies included the location within the artery, the size, and the shape of the bodies. In addition, 3D models were available for the lumens and the calcified bodies, separately.

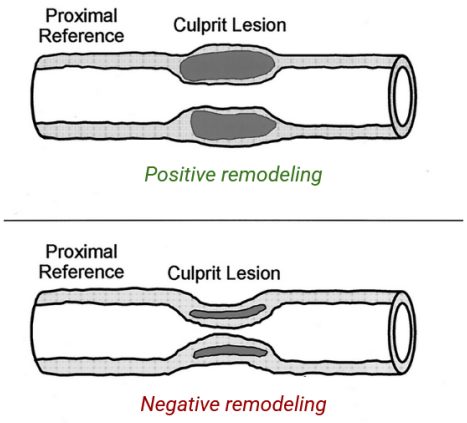

Figure 2.1: The effect of positive vs. negative remodeling in response to arteriosclerosis. Positive remodeling involves thickening of the vessel wall in the direction away from the centerline. Negative remodeling involves wall thickening towards the center line of the artery, leading to a substantial decrease in lumen area compared to the unaffected reference section. Adapted from[45].

A sub-selection of arteries was chosen for reconstruction. Only arteries containing $\geq 70\%$ stenosis were selected as candidates for reconstruction. This was based on the assumption that for lower stenosis

values, positive remodeling would be more dominant compared to negative remodeling. With positive remodeling, the vessel wall thickness increases in the outwards direction. Hence, the effect on the lumen area is not as pronounced, as shown in Figure 2.1. Since the lumen is only slightly affected in such a scenario, it is considered to be similar to a non-calcified lumen. For such arteries, reconstruction was deemed unnecessary. Thus, to see the full effect of the reconstructions, only arteries that demonstrated substantial negative remodeling were selected. Out of the 100 arteries, 23 arteries were selected as suitable candidates for reconstruction.

2.2. 3D artery geometry reconstruction

2.2.1. Pre-calcification lumen reconstruction

For each artery, the geometry data was processed using MATLAB[52]. Points were sampled along the centreline of the artery at a distance of 0.2 mm apart. At each sampled point, a three-dimensional plane perpendicular to the centreline was defined. The intersection between the lumen boundary surface and each plane generated contour points describing the lumen cross-section. Similarly, for the calcified bodies, three-dimensional planes perpendicular to the centreline of the artery were generated. Again, contour points at the intersections between the calcium surface and the planes were saved. In Figure 2.2, a calcified segment of an artery and the corresponding contours of the lumen and the calcium body are shown. Next, the data of the lumen and calcium contours were grouped to realise an array containing cross-sectional contour data for both the lumen and the calcium bodies combined.

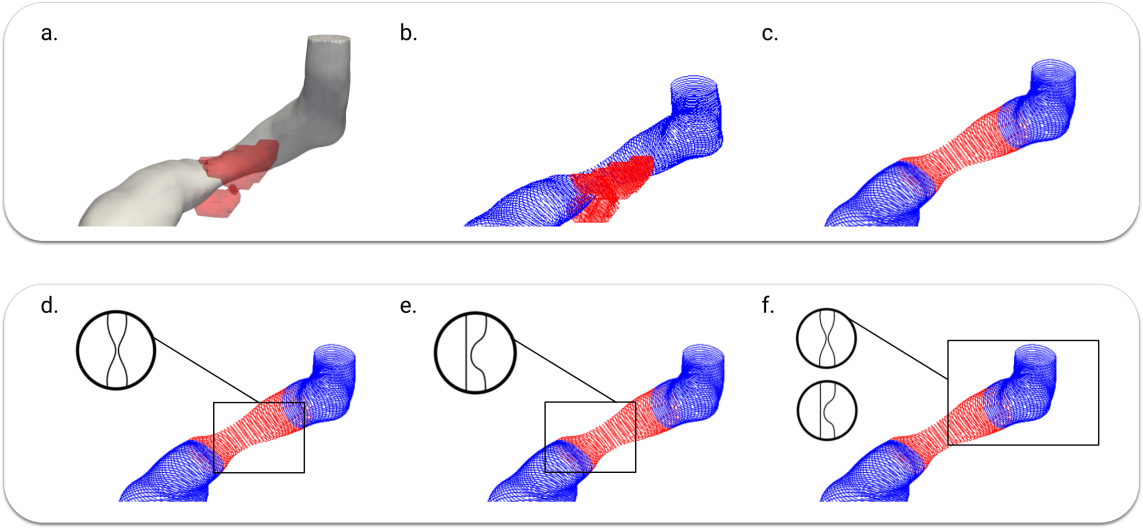

Figure 2.2: Pre-calcification lumen reconstruction. a) The lumen geometry is depicted in grey and the calcium body in red. For the lumen geometry cross-sectional contours were generated at a sampling distance of 0.2 mm apart. Cross-sectional contours were computed for the calcium bodies as well in a separate data array. b) The resulting lumen contours (blue) and the calcium body contours (red). c) The lumen contours that shared a plane with calcium contours were selected for reconstruction, shown in red. d) Method A1 was applied when concentric stenosis was present. e) Method A2 was applied when eccentric stenosis was present. f) Method A3 was applied when stenosis occurred at the terminal part of the artery.

From the combined data array, all lumen contours that shared a plane with calcium were selected. Due to the presence of calcium, this selection was different in size and shape compared to the remaining unaffected lumen. While unaffected contours were predominantly circular in shape, the affected ones resembled crescent-like shapes when eccentric calcifications were present. In addition, concentric calcifications resulted in narrowing of the luminal surface area of the affected contours. Therefore, the affected contours were classified as stenosed. To realise a pre-calcified version of the arteries, the stenosed contours were adjusted in shape and size to resemble the unaffected contours. Three different methods were used to perform the reconstruction, depending on the nature and the location of the calcification. Those methods were the following:

- **A1.** Resizing the stenosed contours to the surrounding unaffected contours.
- **A2.** Interpolating the surrounding unaffected contours to generate new contours.
- **A3.** Copying unaffected contours to replace the stenosed contours.

The stenosed 3D contours were transformed to 2D before any adjustments were made. Transformation from 3D to 2D was realised by multiplying the local contour data points with a transformation matrix. This matrix was composed of the normal and binormal vectors of the corresponding Frenet frame. The generated 2D contours were perpendicular to the centerline. These steps were performed because it enabled easier reconstruction, specifically in areas with high curvature. A schematic overview of the three approaches is shown in Figure 2.2, in the lower panel.

A1. Resizing the stenosed contours to the surrounding unaffected contours
This method used data from the contours upstream and downstream from the stenosed section of the artery. All individual lumen contours of the stenosed section were enlarged based on the magnitude of the surface area of the surrounding calcium-free ones.

To ensure a gradual transition between the reconstructed contours, the surface area used as a reference for enlargement changed based on the position of the lumen contour. Shown in Equation 2.1, a parameter t was introduced to determine the position of the stenosed contour relative to the upstream and downstream neighbours.

$$t = \frac{Id_c - Id_b}{Id_a - Id_b} \tag{2.1}$$

All lumen contours were assigned an id, starting from the first contour of the model up until the last. Here, Id_c represented the id of the stenosed contour, while Id_b and Id_a represented the id numbers of those downstream and upstream from the stenosis, respectively, as shown in Figure 2.3.

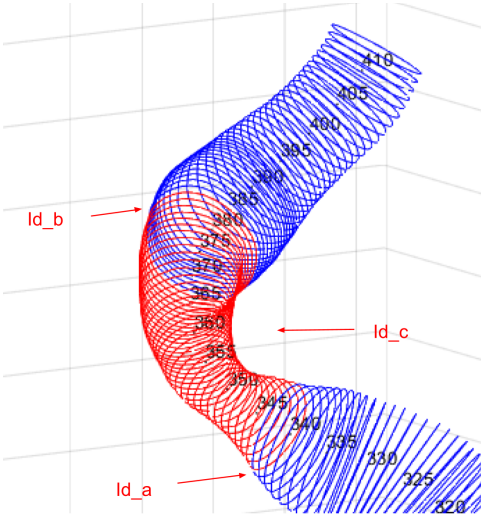

Figure 2.3: Id numbers were assigned to each contour. Id_a and Id_b were the first contours upstream and downstream from the stenosed region. With these as input, the contours in the stenosed region, assigned Id_c, were reconstructed to create pre-calcified versions.

With parameter t as an input value, the target size of the surface area for the stenosed contour was determined, described as A. In Equation 2.2, A_b and A_a corresponded with the surface areas of the downstream and upstream neighbours, respectively. A scale factor S was determined by finding the square root of A divided by A_c, with the latter representing the original size of the stenosed lumen surface area. Lastly, by multiplying the original shape with the scale factor, the final resized contour C was generated. Shown in Equation 2.4, the scaling factor was applied after the original stenosed version C_c was first translated to its centroid G_c.

These steps were performed for each individual stenosed lumen contour. Thus, while Id_b and Id_a were fixed, Id_c changed with each iteration. This resulted in a unique value for t and S per stenosed contour.

$$A = (1 - t) \cdot A_b + t \cdot A_a \tag{2.2}$$

$$S = \sqrt{\frac{A}{A_c}} \tag{2.3}$$

$$C = (C_c - G_c) \cdot S + G_c; \tag{2.4}$$

The resizing method was applied when the calcifications were predominantly of a concentric nature. The affected lumens were roughly the same shape as the surrounding unaffected area, but had a significant decrease in surface area. The stenosed contours retained their original shape after reconstruction.

A2. Interpolating the surrounding unaffected contours to generate new contours
For this method, the affected lumen contours were all completely replaced by newly generated versions. The shape as well as the size were adjusted to resemble the adjacent calcium-free contours. The downstream and upstream reference contours were first resampled to 100 points as a preparation for the interpolation. Point-wise linear interpolation was applied on the resampled downstream and upstream contours to create the reconstructed shapes.
Similar to the resizing method, a parameter t (Equation 2.1) was employed to indicate the relative position of the stenosed contour with respect to the surrounding calcium-free contours. This value was then directly used to generate a new 2D contour C based on the resampled data of the upstream and downstream contours, C_a and C_b:

$$C = (1 - t) \cdot C_b + t \cdot C_a \tag{2.5}$$

This method was employed when the shape of the calcified lumen deviated from the physiological circular shape. For example, when the stenosis was characterised by eccentric calcium deposition. For this method to be successful, the contours upstream and downstream from the stenosis had to be similar in shape. In addition, this method worked best when the stenosed section was located in a section of the artery with little curvature. High tortuosity and big differences in shape between the upstream and downstream contours complicated the use of this method. The success of the method was highly dependent on the alignment between the data points of the reference contours used for the reconstruction.

A3. Copying unaffected contours to replace the stenosed contours
The last method was applied when stenosis was found in the terminal sections of the artery. This method copied an unaffected contour close to the stenosed region and replaced all the stenosed contours with this calcium-free one. In contrast to approaches **A1** and **A2**, this approach only relied on one unaffected contour to perform the reconstruction. Hence, this method was preferred over **A1** and **A2** when calcium bodies were located in the terminal sections of the artery.

Having reconstructed the lumen shape, a surface was generated for the complete artery. The majority of the surface area was constructed in MATLAB, by generating faces between consecutive lumen contours. For the final adjustments, which involved joining surface segments together that failed to be reconstructed in MATLAB, the model was imported into MeshMixer[5]. In addition, any artefacts resulting from joining the surface segments were smoothed out. The completed models were saved as STL files. The final steps for the surface generation are shown in Figure 2.4.

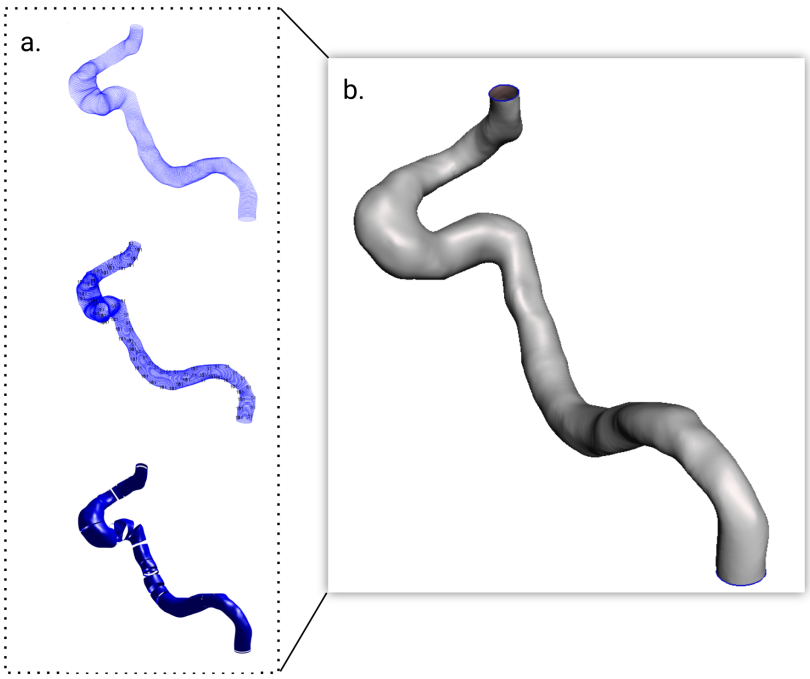

Figure 2.4: Generation of the lumen surface. a) After reconstruction, the lumen contours were first aligned, ensuring that the surface generation in MATLAB ran more smoothly. Having generated most of the lumen surface in MATLAB, an STL file was exported to MeshMixer. b) The final lumen surface was completed in MeshMixer. The separate sections were joined, and the overall surface was smoothed to clear out any artefacts.

2.3. Post-processing

2.3.1. CFD models

Software and solver

The CFD simulations were run in FEBio, a software tool specifically developed for nonlinear finite element analysis in biomechanics and biophysics[36]. In fluid mechanics problems, a non-linear system of equations has to be solved with each time step. To speed up the process of solving these equations, a quasi-Newton Broyden method is available in FEBio. With this method, the first iteration of each time step is solved using Newton's method, which is relatively time-consuming. The following iterations are solved with a Broyden update. This is computationally less expensive as it produces an approximation of the matrix solved by the first Newton iteration[4]. To optimise computational efficiency, the Broyden method was selected for all simulations.

Discretisation of the fluid domain

To discretise the continuous domain of the 3D models, a finite element mesh was created using a previously developed in-house MATLAB code. However, prior to discretisation, the generated surface models were first extended to facilitate the CFD simulations. The GIBBON toolbox [40] was used for both the construction of the mesh as well as the creation of the extensions.

The faces and vertices from the STL files were retrieved for each surface model. Extensions were included at the inlet and outlet of the models. The patchExtend function of the GIBBON toolbox was used, which extends the boundary surfaces of a geometry along the edges of those surfaces. The mean direction of the surface edges served as the direction for the extrusion. In this manner, the extensions aligned with the longitudinal direction of the artery. An inlet extension of 8 mm was included to ensure a fully developed flow. The length of the outlet extension was smaller, 5 mm. This was added to avoid divergence of the simulation.

Next, boundary layers were created for the model. The boundary layer (BL) mesh consisted of pentahedron elements. Pentahedra were chosen for their anisotropic properties, allowing for stretching

of the elements in the boundary layer region [26]. A mesh convergence analysis was performed to determine the appropriate mesh parameters (see Appendix B). For the BL mesh, a total of five layers were incorporated. A layer thickness of 0.1 mm was set, with a bias value of 2. This ensured that the boundary layers increased in thickness closer to the centre of the lumen.

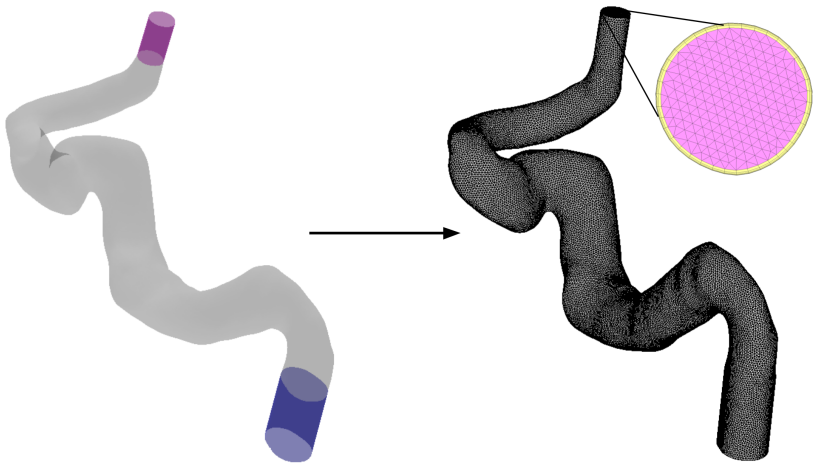

Figure 2.5: Discretisation of the fluid domain. An inlet extension (blue) and an outlet extension (magenta) were first created. Next, a hybrid mesh consisting of tetrahedral en pentahedron elements was constructed. The top right figure shows the cross-section of the meshed lumen, with the BL mesh in yellow and the remaining fluid mesh in magenta.

Finally, the inlet and outlet were capped and the remaining fluid domain was meshed. This mesh consisted of linear tetrahedral elements. Due to the complexity of the lumen shape, these elements were deemed the most suitable, given their ability to fill irregular geometries uniformly [26]. An average element edge length of 0.25 mm was selected for the tetrahedral elements. In Figure 2.5, the final meshed model is shown.

Time step

To obtain physically correct and stable results, the chosen time step could not be too large. A cut-off value of 1 for the Courant-Friedrichs-Lewy (CFL) number is commonly used in fluid dynamics software which is based on explicit solvers. By default, the fluid analyses in FEBio are run in dynamic mode which use an implicit time integration scheme. For implicit solvers, the limit on the CFL number is less strict [27]. Therefore, a time step of 0.001 seconds was chosen, which corresponded to a CFL number of 20. Smaller time steps did not show different results, while large time steps resulted in divergence (see Appendix C).

Material parameters

Blood is naturally a non-Newtonian fluid, with shear-thinning behaviour. At a lower shear rate, the viscosity of blood increases, while an increase in viscosity is seen at a higher shear rates [53]. However, to reduce computational costs, a Newtonian fluid model can be used in CFD analysis of blood flow. By using a Newtonian model, a constant viscosity is prescribed, which eliminates the need for additional computations. Previous studies have shown a negligible effect of blood rheology on WSS and helical flow [21] [23]. Hence, for the simulations, blood was modelled as an incompressible Newtonian fluid. The density (ρ) was prescribed at 1060 kg/m^3, with a constant viscosity (μ) of 3.5 x 10^{-3} Pa·s and a bulk modulus (k) of 2.2 x 10^9 Pa [21]. Since CFD analyses were performed, the walls of the artery were presumed to be rigid.

Boundary conditions

Boundary conditions were prescribed at the inlet, outlet, and lumen surface of the model. At the lumen surface, a no-slip boundary condition was applied, imposing zero fluid velocity at the external surface of the fluid domain.

A pulsatile velocity profile was prescribed at the inlet, based on an in vivo flow waveform reported by

Lee et al.[34]. The waveform was obtained from an average-sized internal carotid artery downstream of the carotid sinus. Prior to deriving the inlet velocity profile, a comparative analysis was performed to determine whether the flow magnitudes should be adjusted according to the inlet surface area of each artery (section A.3). Since this adjustment did not affect the resulting hemodynamic distributions, the original flow waveform was used directly. Velocity values were therefore calculated by dividing the flow rate by the inlet surface area of each individual artery.
The inlet condition was applied over two cardiac cycles, each with a duration of 0.88 s, corresponding to a heart rate of 68 beats per minute. To avoid an abrupt onset of flow at the start of the simulation, a 1-second sigmoid ramp function was applied. The resulting flow waveform used to derive the inlet velocity profiles is shown in Figure 2.6.

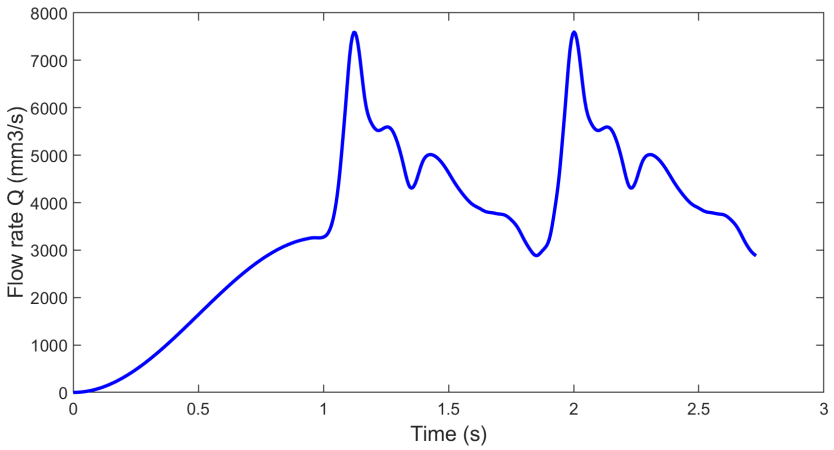

Figure 2.6: Blood flow curve over two cardiac cycles used to derive the inlet velocity for the simulations. A sigmoid function of one second ensured that the flow gradually reached the beginning of the first cycle. The curve was adapted from the average flow curve reported by Lee et al.[34].

Several outlet boundary conditions were evaluated to determine the most physiologically appropriate approach for the simulations (section A.1). Based on this analysis, a resistance-based outlet boundary condition was selected. The outlet pressure was prescribed as a time-varying quantity dependent on the flow resistance (R), the flow (Q) and the offset pressure (P_o), according to:

$$P = RQ + P_o \tag{2.6}$$

A resistance value of 6.67 x 10^8 kg/m^{4}s and an offset pressure of 10000 Pa were used. With these parameters, the simulated pressure ranged from 83 to 100 mmHg, shown in section A.1. These pressures where well in range of the physiological values of 80 – 120 mmHg between end-diastole and peak systole [39].

2.3.2. Hemodynamics

The CFD simulation results were imported into Paraview [2] to obtain the nodal wall shear stress values in x, y and z direction for every time step. These were used to generate the hemodynamic parameters of interest: TAWSS, OSI, and RRT.

Time-averaged wall shear stress

The TAWSS is derived from the WSS, which is calculated from the blood velocity gradient at the wall multiplied by the blood viscosity μ, shown in Equation 2.7. Where u indicates the axial component of the velocity vector and y indicates the distance from the centerline of the artery to the wall. The integral of the WSS magnitude over one cardiac cycle T, divided by T, gives the TAWSS (Equation 2.8).

$$WSS = \vec{\tau}_w = \mu \cdot \left(\frac{\partial u}{\partial y}\right)_{wall} \tag{2.7}$$

$$TAWSS = \frac{1}{T}\int_0^T |WSS|\,dt \tag{2.8}$$

Oscillatory shear index
The OSI is a measure to describe the deviation of the WSS from its mean direction within a cardiac cycle. It ranges from 0 to 0.5, where 0 indicates unidirectional flow and 0.5 indicates completely reversed flow [33]. The OSI is derived from the magnitude of the WSS vector and the WSS magnitude.

$$OSI = 0.5\left[1 - \left(\frac{\left|\int_0^T WSS\,dt\right|}{\int_0^T |WSS|\,dt}\right)\right] \tag{2.9}$$

Relative residence time
The relative residence time is computed from the TAWSS and the OSI. It is a measure to quantify the amount of time blood components, such as lipids and blood platelets, spend near the vascular wall. A high RRT would indicate that blood resides near the wall for a relatively long period of time.

$$RRT = \frac{1}{TAWSS(1-2OSI)} \tag{2.10}$$

2.3.3. Calcium location

To complement the hemodynamics, the models of the calcified arteries were analysed to identify areas in contact with calcium bodies. This calcium localisation was performed using an in-house developed MATLAB code. For each node of the lumen mesh, the smallest distance to nodes of the calcified bodies was registered. If calcium was not present, a zero distance was assigned to the lumen nodes. If calcium was present, the lumen nodes were a calcium distance assigned. Hence, lumen nodes with a distance greater than zero were an indication of calcium presence.

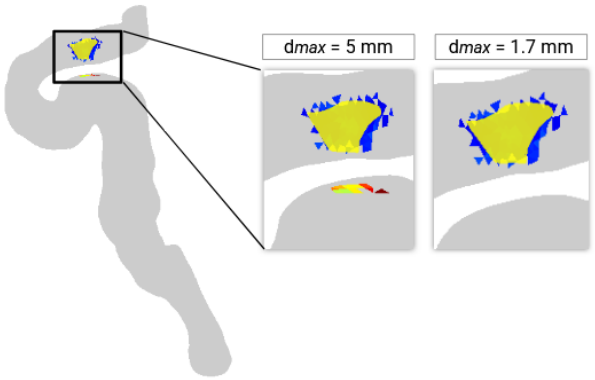

Figure 2.7: Process of calcium registration. The process of calcium detection involved finding the smallest distance between lumen nodes and calcium nodes. A maximum value for the distance (d_{max}) was set to account for the misclassification of calcium presence in areas where high curvature was present. When the maximum distance was too large (e.g. 5 mm), areas opposite the calcified area were misclassified.

Due to the high curvature of the arteries, lumen nodes far away from calcified bodies sometimes mistakenly registered the presence of calcium. To resolve this misclassification of calcium presence, a maximum distance of 1.7 mm between the lumen nodes and calcium nodes was prescribed, shown in Figure 2.7. Data about calcium presence were saved at the lumen nodes of the calcified artery. However, data of hemodynamic parameters were only available for the healthy model. Therefore, to facilitate statistical analysis, the calcium data were transferred to the lumen nodes of the healthy model. VMTK [29] was employed to project the data from the diseased artery model to the healthy artery model.

2.3.4. Creation of two-dimensional maps

For both the hemodynamic parameters and the calcium location, two-dimensional maps were created, shown in Figure 2.8. This step was performed to aid in the subsequent statistical analysis.

The 2D-maps were derived from the 3D models of the healthy arteries using VMTK. Each artery was virtually cut along the longitudinal direction, and two variables were created: the AbscissaMetric and AngularMetric. The Abscissametric defines the longitudinal axis of the 2D map, thus representing the y-axis. It was computed automatically from the curvilinear abscissa defined on the centerline of the artery. The range of the AbscissaMetric values is equal to the total length of the artery. The sector length in this direction was 0.8 mm. The AngularMetric accounted for the x-axis. It represented the circumferential coordinates of the artery around the centerline and spanned the interval $(-\pi, +\pi)$. The cross-sectional 0.8 mm slices were divided into eight angular sectors of 45 degrees.

The final 2D grid consisted of rectangular sectors of equal size. For all parameters, the sector average was used for further analyses. The approach was based on a previously developed in-house code, which was inspired by a method described by Hartman et al.[28].

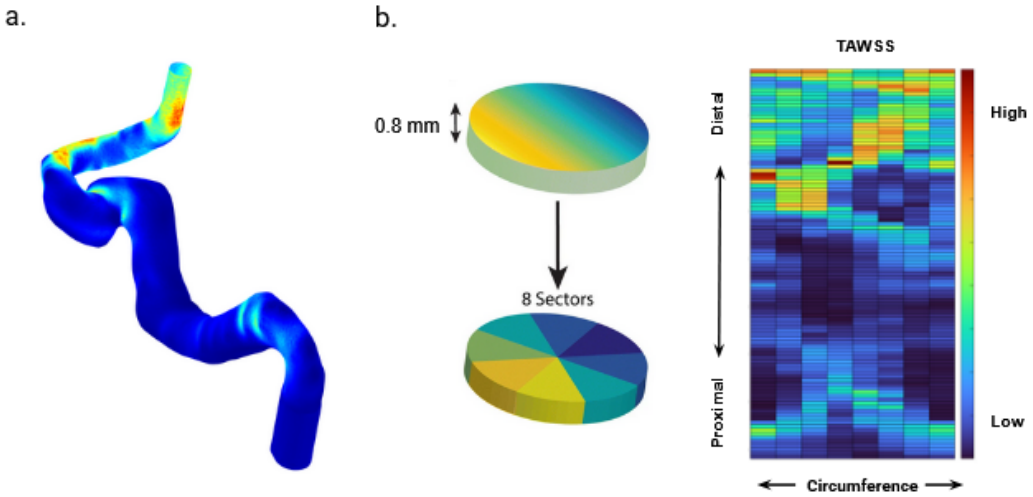

Figure 2.8: Creation of the two-dimensional map from a 3D model. a.) The 3D model with the TAWSS distribution mapped onto the lumen surface. b.) Slices with a thickness of 0.8 mm were created; each slice was then divided into eight sections at a 45-degree angle. The resulting rectangular sectors were plotted to create the 2D map. Here, the y-axis corresponded with the longitudinal direction and the x-axis corresponded with the circumferential direction of the artery, respectively. Grids were generated for all parameters of interest. Adapted from [28].

2.3.5. Data analysis

Data are presented as mean and standard deviation (SD) or median [interquartile range (IQR)] for continuous variables. Hemodynamics data are reported up to the 99th percentile to account for outliers.

In the primary analysis, differences in areas exposed to future calcium presence and areas without exposure were examined. This was realised by grouping the 2D sector data, resulting in a calcium-free group and a calcium-containing group. The median values for the TAWSS, OSI and RRT were computed for both groups per artery. With these values the relative difference between the sectors was calculated, using the calcium-free sectors as reference. From the individual medians, an overall median was determined for all hemodynamic parameters to obtain an aggregated result for the TAWSS, OSI and RRT.

For the secondary analysis, the calcium presence and hemodynamics were investigated per anatomical segment. The percentage of areas exposed to calcium was determined for the C2, C3, C4, C5, and C6 ICA segments for all arteries. In addition, the TAWSS, OSI and RRT were determined for these segments. For each segment, the median value per parameter, per artery was determined. These results were aggregated to obtain the median values per hemodynamic parameter for each segment across all analysed arteries.

3

Results

3.1. Illustrative example

In the next sections, an illustrative example is first described to discuss the hemodynamics in more detail. The artery for the example is described as Artery 2R and is a right-sided intracranial carotid artery. The size of this artery resembled the mean size compared to the other five arteries, therefore, this artery was chosen as an illustrative case. The results for the other arteries can be found in Appendix E.

3.1.1. Blood velocity and flow patterns

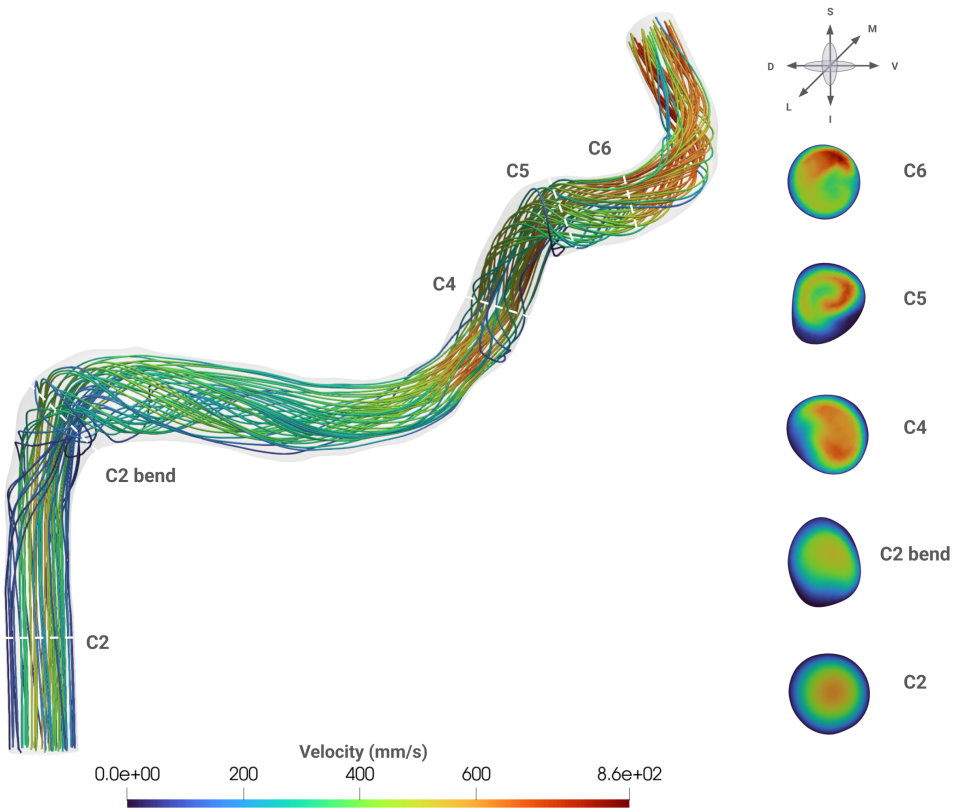

Figure 3.1: Streamlines and velocity planes during peak-systole. The beginning of segments C2, C4, C5, and C6 are highlighted in the figure. Corresponding axial velocity planes were retrieved, showing a developed flow profile at C2 and skewed profiles until C6. For the cuts at C2 and C4, in clockwise direction, the sides correspond with the medial (M), ventral (V), lateral (L), and dorsal (D) side of the artery. For the other cuts, sides correspond with the superior (S), medial (M), inferior (I), and lateral (L) side of the artery.

In Figure 3.1, the streamlines and velocity planes at peak-systole are shown. The velocity stayed relatively low in segments C2 and C3. At the inlet, the flow streamlines were mainly parallel to each other and did not deviate from the longitudinal direction. This changed once the fluid reached the bend of C2. A helical flow pattern was seen at the inner curve in this region. Compared to the upstream part, the streamlines seemed to follow a direction tangent to the cross section of the lumen. After this bend, the flow recovered to the parallel streamline pattern until it reached segment C4. Here, the flow formed helices again and the velocity started to increase. From this segment onwards, the maximum velocity increased from 671 mm/s to 860 mm/s at the end of segment C6.

The cross-sectional slices at the beginning of each segment show the velocity distribution locally. All cuts were made from a downstream viewpoint. For the cuts at C2 and C4, the left side corresponded with the dorsal side of the artery, while the top side corresponded with the medial side of the artery. For the other segments, the left side of the cut corresponded with the lateral side of the artery, while the top side corresponded with the superior side.

The cut at C2 showed a parabolic velocity profile indicative of developed flow, with an increased velocity at the centre of the slice. At the bend of C2, which showed helical flow, the velocity was relatively low and was slightly skewed towards the superior side of the artery. The cross-sectional slices at C4, C5 and C6 also showed a skewed velocity pattern, with the highest values towards the ventral side, the medial side and the superior side, respectively. The C5 slice even showed a spiralling band of increased velocity towards the centre of the cut.

The calcium-containing segments C5 and C6, were thus characterised by relatively high flow velocities compared to the upstream segments. Similar to the upstream segments, some helical flow was present.

3.1.2. Calcium location

In this model, one calcium body was identified, located at the distal end of the artery as shown in Figure 3.2a. 45 sectors contained calcium and 571 sectors were without any calcium, shown in Figure 3.2b. Most of the calcium was located in segment C6, where 56% of the sectors contained calcium. In segment C5, 13% of the sectors were marked by calcium presence.

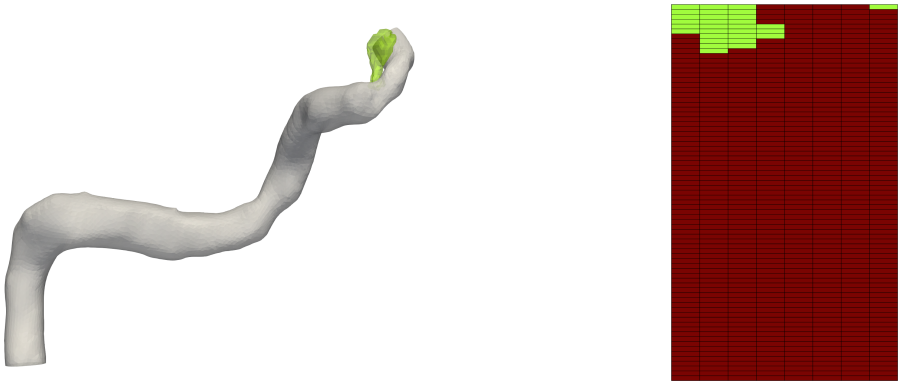

(a) (b)

Figure 3.2: Registration of calcium presence for Artery 2R. a) The calcified artery, with one calcium body at the end of the artery, shown in lime. b) The corresponding 2D map, the sectors colored in lime were affected by calcium.

3.1.3. Hemodynamics

Time-averaged wall shear stress

The time-averaged wall shear stress distribution of Artery 2R is shown in Figure 3.3. The TAWSS ranged from 0.05 Pa to approximately 5.6 Pa, after exclusion of outliers. On the left, the 3D model including the inlet and outlet extensions is shown. On the right, the corresponding 2D map shows the TAWSS in the artery excluding the inlet and outlet extensions.

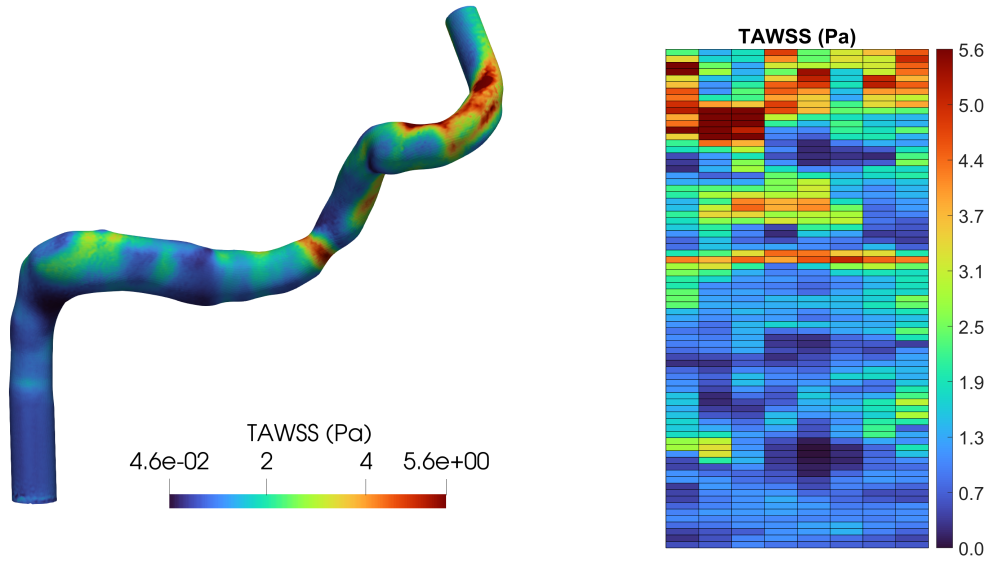

Figure 3.3: TAWSS in Pa in Artery 2R.

In the upstream part, the TAWSS stayed relatively low. Upon visual inspection, a local decrease in TAWSS was found along the inner curve of the first bend. Downstream from this bend, the TAWSS remained low, with locally some areas of slight increase in TAWSS. A distinct band of higher TAWSS was found in the area where C3 transitions into C4. This band is displayed in the 2D map, where a horizontal line of TAWSS values greater than 3 Pa is seen. In the 3D model, a decrease in lumen circumference was seen in this area.

In segment C4, increased values were observed on the medial side of the lumen. The highest TAWSS values were observed at the transition from segment C5 to segment C6. An area with increased TAWSS values was seen at the inner curve of the bend. Directly after this area, the TAWSS decreased again, which is more clearly shown in the 2D map. The area with increased TAWSS can be recognised by the clustered sectors with TAWSS values close to 5 Pa. Downstream from this cluster, sectors with values of 2 Pa and lower are found. In this area, calcification was present. In the calcium containing sectors, a median TAWSS of 3.3 (IQR 4.2 – 2.2) Pa was found. In segment C5, the median of the calcium containing sectors was 6.4 (IQR 5.8 – 7.3) Pa. The median TAWSS in the other sectors was 2.7 (IQR 1.9 – 4.2) Pa. Segment C6 contained the most calcium, as was already shown in Figure 3.2b. In this segment, a median TAWSS of 3.2 (IQR 2.1 – 4.1) Pa was found in the calcium-containing sectors. The median in the calcium-free sectors was 3.4 (IQR 3.0 – 3.7) Pa in this segment, shown in Table 3.1.

Table 3.1: TAWSS in Pa in Artery 2R. For each segment the overall median, the calcium-free median and the calcium-containing median of the TAWSS is given.

Segment	Overall	Calcium-free	Calcium-containing
C2	1.00 [0.75 – 1.25]	1.00 [0.75 – 1.25]	
C3	1.67 [1.14 – 2.52]	1.67 [1.14 – 2.52]	
C4	1.58 [1.21 – 2.17]	1.58 [1.21 – 2.17]	
C5	3.00 [1.95 – 5.95]	2.73 [1.93 – 4.17]	6.37 [5.84 – 7.27]
C6	3.34 [2.64 – 3.94]	3.38 [3.00 – 3.74]	3.24 [2.14 – 4.07]

Oscillatory shear index

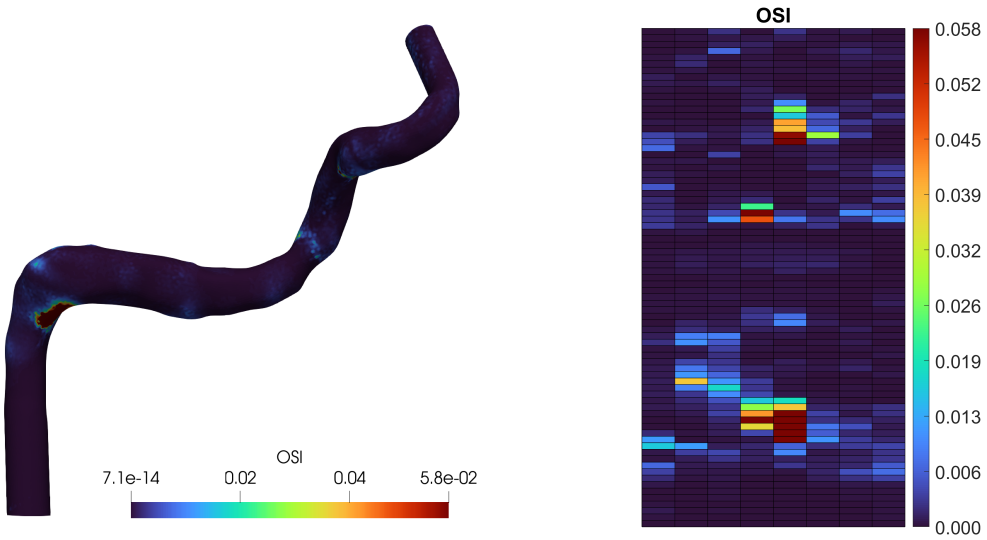

Figure 3.4: OSI in Artery 2R.

The OSI revealed generally low values with only some minor areas of increase, shown in Figure 3.4. The median OSI in the total artery was 0.69 x 10^{-3} (IQR 0.29 – 1.9 x 10^{-3}). Areas of increased OSI were seen along the inner curve of the bend in segment C2, along the outer curve of the bend at C3, and along the inner curve of the bend between C4 and C5. The greatest median OSI value was found in segment C4, followed by segment C2. In the calcium area, the OSI was low. In segment C5, the median OSI was 0.46 x 10^{-3} (IQR 0.15 – 0.63 x 10^{-3}) in the calcium-containing sectors and 0.63 x 10^{-3} (IQR 0.17 – 1.3 x 10^{-3}) in the calcium-free sectors. In segment C6, the median OSI was 0.61 x 10^{-3} (IQR 0.34 – 0.92 x 10^{-3}) in the calcium-containing sectors and 0.45 x 10^{-3} (IQR 0.31 – 0.88 x 10^{-3}) in the calcium-free sectors. The median values per segment are displayed in Table 3.2.

Table 3.2: OSI x 10^{-3} in Artery 2R . For each segment the overall median, the calcium-free median and the calcium-containing median of the OSI is given.

Segment	Overall	Calcium-free	Calcium-containing
C2	0.76 [0.30 – 2.85]	0.76 [0.30 – 2.85]	
C3	0.66 [0.27 – 1.51]	0.66 [0.27 – 1.51]	
C4	1.01 [0.37 – 1.91]	1.01 [0.37 – 1.91]	
C5	0.56 [0.16 – 1.04]	0.63 [0.17 – 1.28]	0.46 [0.15 – 0.63]
C6	0.56 [0.34 – 0.90]	0.45 [0.31 – 0.88]	0.61 [0.34 – 0.92]

Relative residence time

In Figure 3.5, the distribution of the RRT is shown. In general, the RRT did not reach large values and was low along all segments, represented by a median value of 0.84 (IQR 0.52 – 1.2). Apart from local increased areas, the RRT decreased in the downstream direction. In segment C2, a median RRT of 1 (IQR 0.86 – 1.6) was found. In the following segments, the median RRT values were 0.69 (IQR 0.46 – 0.96), 0.72 (IQR 0.54 – 1.0), 0.42 (IQR 0.19 – 0.54) and 0.35 (IQR 0.27 – 0.46), shown in Table 3.3. However, similar to the OSI, some local increased areas were seen: along the inner curve of the bend in segment C2, along the outer curve of the bend at C3, and along the inner curve of the bend between C4 and C5. Especially along the inner curve of C2, a local cluster of sectors with RRT values close to 5.5 was found. With regard to the calcium-containing sectors, median RRT values were 0.19 (IQR 0.16 – 0.19) and 0.37 (IQR 0.26 – 0.57) in the calcium-containing sectors of C5 and C6, respectively. The calcium-free sectors had median RRT values of 0.43 (IQR 0.27 – 0.55) and 0.32 (IQR 0.27 – 0.40) in segments C5 and C6, respectively.

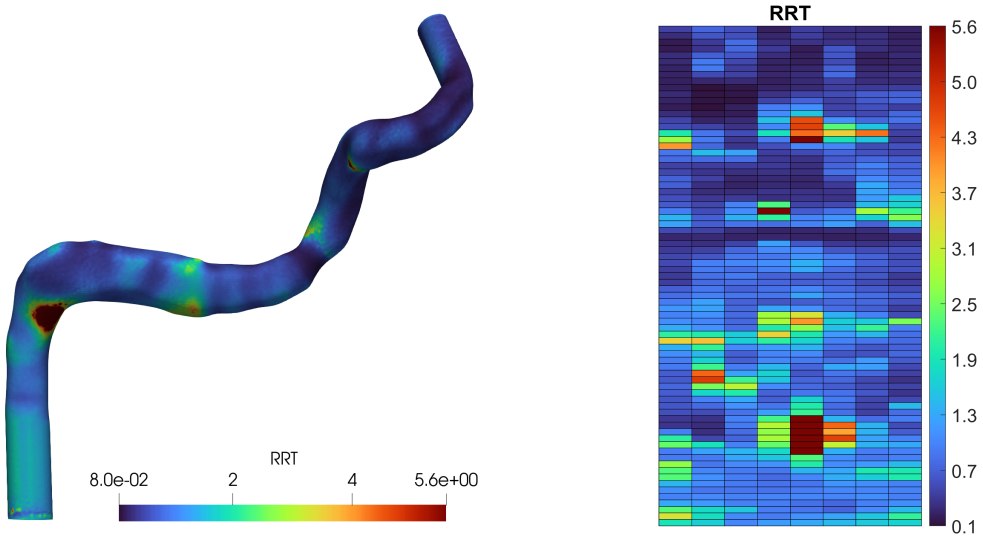

Figure 3.5: RRT in Artery 2R.

Table 3.3: RRT in Artery 2R. For each segment the overall median, the calcium-free median and the calcium-containing median of the RRT is given.

Segment	Overall	Calcium-free	Calcium-containing
C2	1.04 [0.86 – 1.57]	1.04 [0.86 – 1.57]	
C3	0.69 [0.46 – 0.96]	0.69 [0.46 – 0.96]	
C4	0.72 [0.54 – 1.04]	0.72 [0.54 – 1.04]	
C5	0.42 [0.19 – 0.54]	0.43 [0.27 – 0.55]	0.19 [0.16 – 0.19]
C6	0.35 [0.27 – 0.46]	0.32 [0.27 – 0.40]	0.37 [0.26 – 0.5]

3.2. Reconstructed lumens

From the stenosed arteries dataset (n=23), a subset of eight arteries was selected for reconstruction. The selected arteries represented a range of anatomical and pathological characteristics, including both left and right-sided arteries, variation in artery diameter, tortuosity, and differences in the amount of calcifications. Key characteristics were comparable between the subset and the stenosed dataset, suggesting that the subset provided a reasonable representation of the overall population. Average maximum, mean, and minimum diameters for the stenosed dataset were 5.9 (SD = 1.0) mm, 3.9 (SD = 0.72) mm, and 1.7 (SD = 0.54) mm. Average maximum, mean, and minimum diameters for the subset (n=8) were 5.4 (SD = 0.92) mm, 3.6 (SD = 0.65), and 0.67 (SD = 0.39) mm. In addition, the average lengths from segment C2 up until segment C6 were 74 (SD = 6.1) mm and 72 (SD = 7.0) mm, for the stenosed dataset and the subset, respectively. The median number of calcium bodies was 4 (IQR 3 – 5.3) in the stenosed dataset and 4 (IQR 1.8 – 4.3) in the subset. The subset contained four left-sided arteries and four right-sided arteries.

Following the approaches mentioned in subsection 2.2.1, the scaling approach **A1** was performed on all eight arteries. The interpolation approach **A2** was performed on two arteries: Artery 1L and 3L. The copying approach **A3** was performed on two arteries as well: 2R and 5L. The scaling approach was applied after the other adjustments were performed, in case of approaches **A2** and **A3**. This combined method was used when some stenosed sections in the artery could not be recovered through scaling alone. The reconstruction resulted in a mean increase in lumen volume of 9.3% compared to the calcified arteries. The mean volume of the reconstructed arteries was 899 (SD = 507) mm^3, while the mean volume of the calcified arteries was 823 (SD = 396) mm^3. Figure 3.6 shows an example of the resulting healthy lumen after reconstruction. All other results of the reconstructions can be found in Appendix D.

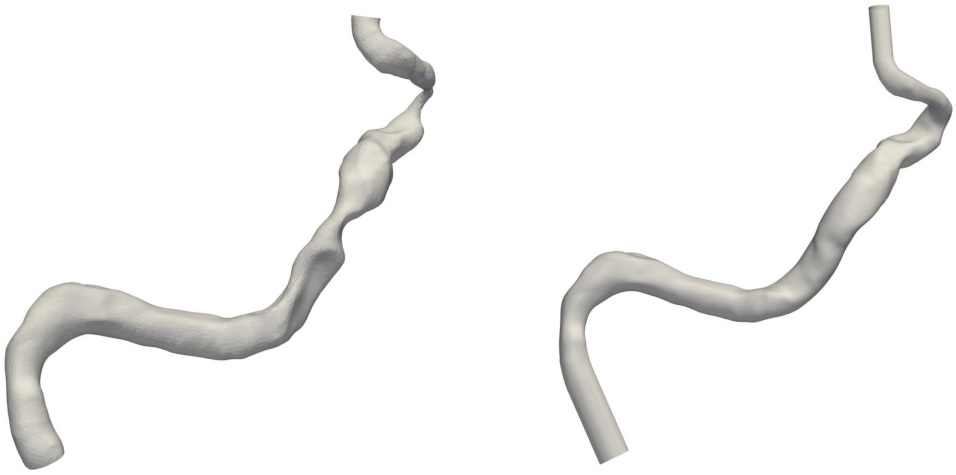

Figure 3.6: Artery 1L before and after reconstruction of the lumen. Displayed on the left, the artery before reconstruction contained areas with a decreased diameter for segment C3 up until segment C6. On the right, the reconstructed artery is shown, the stenosed areas have been replaced to generate a non-obstructed lumen.

Due to complications in the CFD analyses, 2 arteries could not be included. Therefore, six arteries remained for the primary and secondary analysis, displayed in Figure 3.7. The first two arteries, 1L and 1R belonged to the same subject and represent the left and right-sided intracranial ICA. All other arteries belonged to different subjects. Three arteries were right-sided, while the other three were left-sided. In total, 4216 sectors were generated from the 2D mapping process. The average number of sectors was 703 (SD = 74); depending on the length of the artery, the number was smaller or greater.

3.3. Calcium location

The number of calcium bodies per artery ranged from one to five. A median value of 3 (IQR 1 – 4) calcium bodies was found when combining the individual data. Following the 2D mapping, a total of 907 out of 4216 sectors contained calcium. The localisation and extent of the calcium differed across ICA segments. Per segment, the percentage of sectors that contained calcium was retrieved. As shown in Table 3.4, there was no calcium present in the sectors of the C2 segment in the arteries. On the other hand, each artery contained sectors with calcium in segment C6.

Overall, segments C4 and C5 were mostly affected by calcium bodies. Especially segment C4, with 61% of all sectors within this segment containing calcium when all data was combined. In segment C5, 53% of the sectors contained calcium.

Table 3.4: The percentage of calcium-containing sectors was retrieved for all arteries, for segments C2 up to C6. In segment C2, none of the arteries contained calcium sectors. In segments C3 to C6, calcium was found to a varying extent, depending on the artery.

Artery	Calcium bodies	Calcium sectors(%)				
		C2	C3	C4	C5	C6
1L	5	0	73	79	92	24
1R	4	0	25	62	63	16
2R	1	0	0	0	13	56
3L	1	0	0	0	0	8
4R	4	0	8	61	69	13
5L	2	0	37	80	44	11
Average	3	0	17	61	53	15

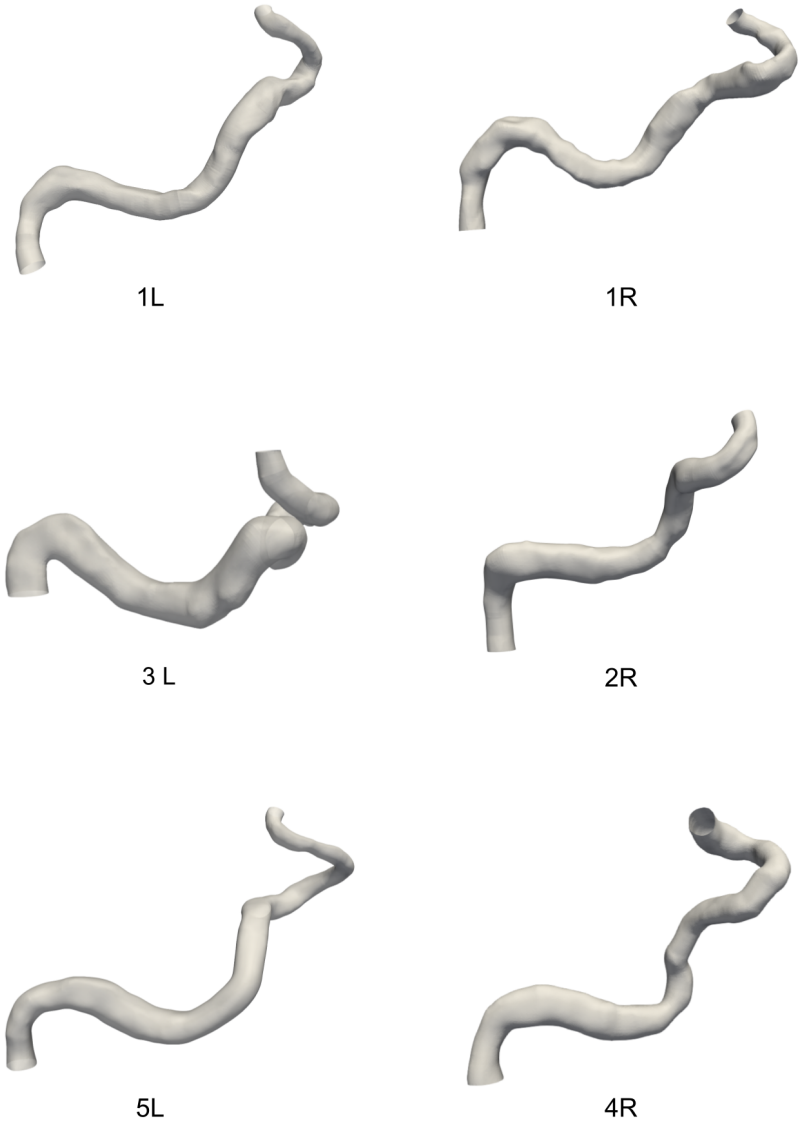

Figure 3.7: The six reconstructed healthy arteries for the CFD simulations. Arteries 1L and 1R corresponded to the same subject. Arteries 1L, 3L, and 5L were left-sided, while arteries 1R, 2R, and 4R were right-sided.

3.4. Hemodynamics in calcified and non-calcified groups

The total number of sectors was 4216, of which 907 were calcium-containing and 3309 were calcium-free. For each artery, the calcium-containing sectors were separated from the calcium-free sectors. Per group, the median TAWSS, OSI and RRT were retrieved.

In four of six arteries, the TAWSS was higher in the calcium-containing sectors, as shown in Figure 3.8. This difference was especially evident for Artery 2R, with a percentage change of 171.3% between the calcium and non-calcium group. Patients 1L and 1R both showed a lower median TAWSS in the calcium group. However, the percentage change between the calcium-containing and calcium-free groups was small, -5.8% and -5.7%, respectively. The combined artery data showed a median TAWSS in the calcium-containing group of 2.76 (IQR 2.48 – 3.34) Pa, while the median TAWSS in the calcium-free sectors was 1.98 (IQR 1.23 – 2.63) Pa. Corresponding to a percentage change of 39.6% in favor of the calcium-containing group.

Regarding the OSI, three out of six arteries had higher values for the OSI in the calcium-containing groups compared to the calcium-free groups. The other half of the arteries had higher OSI values in the calcium-free groups. Arteries 3L and 5L demonstrated the greatest difference between the two groups,

both showing greater OSI values in the calcium-free group. With artery 3L having a percentage change of -73.6%, indicating that the calcium-containing group contained lower OSI values. The median OSI for this artery was 1.8 x 10^{-3} (IQR 0.61 – 6.3 x 10^{-3}) in the calcium-free group, while the median OSI was 0.48 x 10^{-3} (IQR 0.30 – 0.92 x 10^{-3}) in the calcium-containing group. The aggregated result also showed the highest median OSI in the calcium-free group, with a value of 0.96 x 10^{-3} (IQR 0.72 – 1.1 x 10^{-3}). In contrast, the aggregated result of the calcium-containing group demonstrated a median OSI of 0.74 x 10^{-3} (IQR 0.48 – 0.011 x 10^{-3}). However, the difference between both groups was smaller, compared to Arteries 3L and 5L.

For the RRT, Arteries 1L and 1R, showed higher values in the calcium-containing group compared to the calcium-free group. However, similar to the results of the TAWSS, this difference was little for artery 1R. All other arteries, as well as the aggregated result, showed lower RRT values in the calcium-containing group. The median RRT ranged from 0.25 to 0.88 in the calcium-containing groups. The aggregated result for the calcium groups had a median RRT of 0.43 (IQR 0.36 – 0.48). In the calcium-free group, the aggregated result showed a median RRT of 0.57 (IQR 0.45 – 0.88). The median RRT ranged from 0.42 to 1.77 in the calcium-free groups, when all arteries were considered.

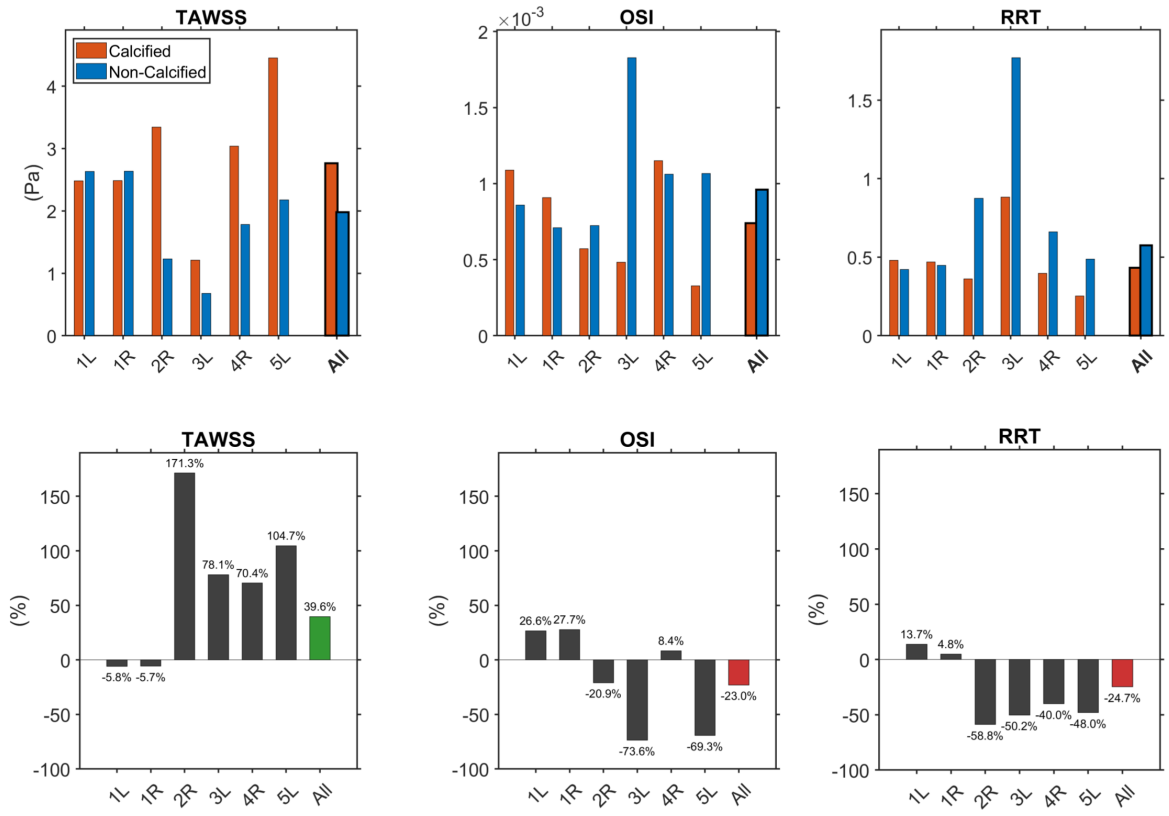

Figure 3.8: TAWSS, OSI, and RRT for all arteries for the calcium-containing (orange) and the calcium-free (blue) group. In the top panel, the median values for both groups are displayed for all three parameters. Values are shown for the individual arteries and the aggregated result. Compared to the calcium-free sectors, TAWSS was greater in four out of six arteries, while the RRT was lower in the corresponding arteries. The OSI was greater in the calcium-containing sectors for half of the arteries. The aggregated result showed a higher TAWSS, lower OSI, and lower RRT in the calcium containing sectors. Shown in the lower subpanel, the percent change was positive in the majority of the arteries for the TAWSS. The OSI and RRT demonstrated predominantly negative percentage change values.

3.5. Hemodynamics per segment

In the secondary analysis, the TAWSS, OSI and RRT were evaluated for the separate segments C2, C3, C4, C5 and C6. In the first part of the analysis, no distinction between calcium-containing and calcium-free sectors was made. In the second part, each segment was grouped based on calcium-containing

or calcium-free sectors, similar to the primary analysis. In total, the number of sectors per segment was C2 = 1560, C3 = 648, C4 = 888, C5 = 416, and C6 = 680. In Appendix F, the segment-wise results for the hemodynamic parameters are shown for the individual arteries.

As shown in Figure 3.9, segment C2 demonstrated the lowest TAWSS and the lowest OSI among all segments. The TAWSS value was found to be 1.47 Pa. An OSI of 0.72 x 10^{-3} was found. The highest RRT value was observed in segment C2. This maximum value of 0.8 decreased in the downstream direction. No calcium was present in this segment.

Segment C3 had an overall TAWSS of 1.95 Pa, which did not differ much between the calcium-containing and calcium-free sectors. The OSI was small, 1.25 x 10^{-3}, and the RRT was 0.61. Greater RRT values were found in the calcium-containing sectors compared to the calcium-free sectors.

In segments C4 and C5, the TAWSS values were 2.01 Pa and 4.43 Pa. In both segments, the TAWSS was greater in the calcium-containing sectors compared to the calcium-free sectors. The largest OSI value was present in segment C5, with a value of 1.28 x 10^{-3}. In segments C4 and C5, the RRT was smaller in the calcium-containing sectors compared to the calcium-free sectors.

The TAWSS reached the highest value of 5.63 Pa in segment C6. Between both groups, this parameter was greater in the calcium-free sectors. RRT was lowest in the calcium-free sectors. In general, the lowest RRT was found in this segment, which was 0.25. Similar to the other segments, the OSI was small.

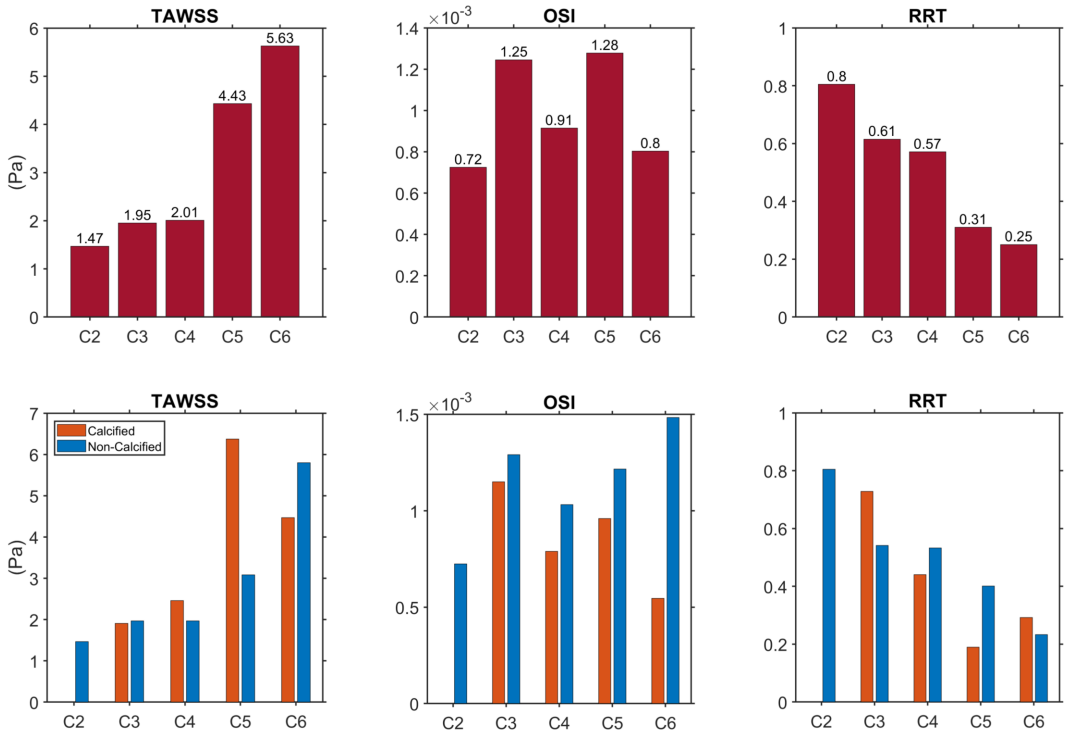

Figure 3.9: The TAWSS, OSI, and RRT per segment for the aggregated results. The TAWSS increased in the downstream direction whereas the RRT decreased. The OSI did not show a similar trend with the median OSI per segment remaining low. However, for all segment the OSI was higher in the calcium-free sectors (blue) compared to the calcium-containing sectors (orange).

4

Discussion

In this thesis, a pilot study was performed to investigate hemodynamic behaviour in the intracranial carotid artery in areas where calcifications were known to develop. To realise this, a pipeline was created to generate healthy reconstructions of calcified arteries. Starting from segmented contours retrieved from CTA imaging, stenosed contours were identified and corrected to develop a healthy surrogate for the calcified artery. CFD models of the ICA were developed in the finite element software FEBio. CFD simulations were run on the healthy lumens to study the time-averaged wall shear stress, oscillatory shear index and relative residence time.

Following the simulations, the majority of the arteries showed increased TAWSS and decreased RRT in areas where calcifications were known to develop. Overall, the OSI was lower in the areas which would be affected by calcifications. In addition, the TAWSS increased towards the distal end of the arteries, while the RRT decreased in this direction. The OSI showed some local differences, but remained low along the complete artery. In the following paragraphs, these results will be discussed in more detail.

4.1. Areas prone to develop calcifications

Out of all six arteries, the segments mainly affected by calcifications were segments C4 and C5. The largest segment C2, which covered 1560 of 4216 sectors, was not affected by any calcifications in any artery. This pattern was also found in previous studies [20] [41]. Both studies studied the distribution of calcifications along the carotid siphon in adults aged 40 years or older, using cone-beam computed tomography. They found the lowest percentage of calcifications in the petrous (C2) segment, followed by the lacerum (C3) segment. Paknahad et al. reported an increased incidence of calcifications with increasing age, irrespective of gender. They discovered the highest prevalence of calcifications in the cavernous (C4) segment, followed by the ophthalmic and clinoid (C5/C6) segments [41]. Findings by Berghout et al. showed similar results, with 56% of calcifications being present in the C4 segment, followed by the C5 segment (24%) and the C6 segment (16%) [8]. Thus, segments C4, C5 and C6 are especially of interest when considering the hemodynamics.

4.2. Hemodynamics

The cut-off values commonly used in literature are a TAWSS smaller than 0.4 Pa [37] and an OSI greater than 0.2 [42]. Values below or above the cut-off are observed in areas with atherosclerosis. This has been shown for the carotid bifurcation [33] [24] [43] [61] and in cerebral arteries, such as the MCA [17]. An absolute cut-off value for the RRT is less common in literature, however relatively high RRT values are commonly reported in atherosclerotic regions. Since the RRT is derived from the OSI and the TAWSS, a high RRT will exist if the OSI is high and the TAWSS is low.

From the primary analysis, it is evident that the TAWSS in all six arteries was greater than 0.4 Pa. Interestingly, the median TAWSS was larger in the calcium-containing sectors compared to the calcium-free sectors for the combined result. However, the values of 2.76 Pa and 1.98 Pa, respectively, were both above the cut-off value. Only in one artery did the median TAWSS approach the cut-off value,

with a median TAWSS of 0.71 Pa. However, this value was seen in the calcium-free sectors. Following the segment analysis, the TAWSS was low in the segments which where the least affected by calcium. Segments C4, C5 and C6 demonstrated the greatest TAWSS values and the lowest RRT values.

Few studies have investigated blood flow in the carotid siphon. An experimental study by Takeuchi et al. showed that atherosclerotic wall thickening was prevalent on the inner walls at curved segments of the carotid siphon. Here, they found that the flow was either slow or disturbed with the formation of slow secondary and recirculation flows [51]. In the illustrative example discussed in subsection 3.1.1, some helical flow was seen at the curved region of segments C2, C4, and C5. At the inner curve of segment C2 the OSI was increased locally, indicating that the flow deviated from its mean direction. However, in this area of disturbed flow, no stenoses or calcifications were found, contrary to the findings of Takeuchi et al. In addition, the increased OSI did not attain large values with a median of 0.76 x 10^{-3}.

A CFD analysis by Zhang et al. showed low TAWSS at the outer walls of the siphon (C4) and the inner wall of segment C6. They computed the stenosis risk for the low TAWSS areas and found that this resembled the incidence of stenoses in these areas. In addition, they found high OSI values in the stenosis areas [62]. However, they only compared their findings to stenosis incidence and also did not provide whether this stenosis was caused by atherosclerotic plaques or purely by calcifications. Nonetheless, both studies demonstrated that arteriosclerosis was more prevalent in areas with slow flow or low TAWSS.

The TAWSS, derived from the WSS, is dependent on the radius of the artery (Equation 2.7). Therefore, the elevated TAWSS values observed in the reconstructed arteries may partially result from the reconstruction procedure itself. The corrected contours were scaled based on the upstream and downstream physiological contours surrounding the stenosed region. Although this approach restored lumen continuity, it may have underestimated the local lumen radius in some regions, thereby leading to an overestimation of the physiological TAWSS magnitude.
However, such reconstruction effects would primarily influence the absolute magnitude of the TAWSS rather than the overall spatial distribution along the artery. Across all reconstructions, the intracranial ICA still demonstrated tapering, consistent with physiological anatomy. Consequently, the observation of increasing TAWSS towards the distal segments may still reflect an underlying anatomical trend rather than solely a reconstruction artefact.

Regarding the oscillatory shear index, in none of the arteries was an OSI found that approached a value of 0.2. The highest OSI was found in the non-calcified sectors of Artery 3L. However, the value of 0.0018 was still below the cut-off. The secondary analysis also showed that the OSI was greater in the non-calcified sectors, independent of the segment. Nonetheless, no matter the presence of calcium, the OSI remained close to 0 for all sectors. Therefore the differences found might be considered negligible. The finding of low OSI values in all sectors indicated that the WSS direction remained consistent during the cardiac cycle. The blood flow was consistently in the downstream direction and reverse, negative flow or transverse flow was very little. Often, studies of the ICA report high OSI in areas of low TAWSS [33] [43]. This trend was also not observed.

Lastly, the relative residence time revealed a trend of decreasing values in the downstream direction. Since the RRT is inversely related to the TAWSS, this trend aligns with the expectations. An increase in RRT is often reported in atheroprone regions of the arteries, indicating an increased duration of time that the particles in the blood flow can stay close to the arterial wall. The simulations revealed that the RRT demonstrated the highest value in the segment where no calcium was found. The current exploratory findings thus do not align with the hypothesis that low TAWSS, high OSI and high RRT create an atheroprone environment.

The characteristics of low TAWSS and high OSI are predominantly proven for atherosclerosis and intimal calcification. As mentioned in the introduction, little research has been performed linking non-atherosclerotic calcium presence in the vascular wall to hemodynamics. Therefore, it is unclear whether the atheroprone cut-off values for TAWSS and OSI are also associated with calcium development. However, mechanisms related to endothelial dysfunction and vascular calcification have been studied. In fact, in response to altered shear stress and turbulent flow, endothelial cells (ECs) have been shown to exhibit different behaviour. Enzymes associated with nitric oxide (NO) production decreased when ECs were exposed to oscillating, slow flow [11]. NO is an important factor in maintaining the contractile

phenotype of VSMCs. In addition, altered flow stimulates ECs to produce osteogenic factors which induces a change in VSMCs from the contractile phenotype to an osteogenic phenotype. This results in VSMCs behaving similar to osteoblasts, cells involved in bone formation [56].

These findings seem to point towards a connection between altered blood flow and non-atherosclerotic calcium development. However, the interplay between TAWSS and OSI and non-atherosclerotic calcium development might be more subtle compared to atherosclerotic calcification. In addition, due to the amount of mechanisms involved, assuming hemodynamics as a major initiator of calcium development might not be reasonable. Instead, the scope might need to be broadened and other unique aspects of the intracranial ICA should be considered.

For example, a point of consideration is the fact that the intracranial ICA is very different from the common arteries investigated in CFD analyses. Not only is the ICA partially encapsulated by rigid bone, it is also very tortuous and curved compared to coronary arteries or the extracranial part of the ICA. A study by de Jong et al. [30] described the characteristics of the carotid siphon based on the anatomical surroundings of the segments. They mentioned the carotid canal surrounding segments C2 and C3, which inhibits these segments from free movement and pulsation. Segments C4 and C5 are intracranial and hence can move more freely. They postulated that the curvature and flexibility of C4 and C5 lead to energy deposition in the arterial wall, which in turn contributes to damage and calcification. This hypothesis is based on the fact that in curved arteries, a centripetal force is necessary to ensure continued flow. This force is generated by a pressure gradient across the lumen, with the highest pressure along the outer wall compared to the inner wall. The pressure acts as a normal load, resulting in circumferential strain within the vessel wall. Part of the flow energy is therefore transferred to the vessel wall, leading to flow attenuation.

Attenuation of pulsatile flow can be quantified using the Pulsatility Index (PI). Schubert et al. [47] examined this quantity in 17 healthy individuals, and found that the PI decreased between segments C4 and C7 of the ICA. On the contrary, between segments C1 and C3, the velocity PI has been shown to increase, suggesting that these regions contribute less to pulsatility damping and may therefore experience less cyclic wall strain [54]. Thus, the distal segments are disproportionally responsible for damping of kinetic energy and are exposed to associated wall strain. However, these findings are related to circumferential stress and strain. Therefore, the high TAWSS found in segments C4 and C5 cannot directly be explained by these results.

Aspects associated with the geometry, such as the curvature and the tortuosity, have not been studied extensively in this thesis. The initial aim was to describe the hemodynamics without directly relating it to the geometry of the arteries. However, the secondary analysis focused on anatomically defined segments, which consistently showed differences in terms of curvature, length, and size. Especially in the curved regions, the magnitudes of the TAWSS, OSI and RRT locally increased or decreased. These findings were discussed in subsection 3.1.3 on a qualitative basis. A more in-depth analysis, which would focus on the curved regions, could have provided a quantitative comparison. Other studies on blood flow in the intracranial arteries separate the curved regions into inner and outer curve or anterior and posterior prior to a quantitative analysis [17]. By doing so, a relation between curvature and hemodynamics or curvature and calcium presence could have been studied. The qualitative results of Artery 2R, showed calcium along the inner curve of segments C5 and C6, located on the posterior side. However, since these findings only represent one case, no conclusions can be drawn and more extensive research is necessary.
On a larger scale, the siphon of the ICA can be separated into four distinct shapes, the U-, C-, S- and V-shape. The different siphon shapes have been shown to be differently associated with the stenosis prevalence [63]. The current analysis did not differentiate between siphon shapes, however, such an analysis might reveal new insights on a relation between calcifications and morphology of the siphon.

4.3. Limitations

A few limitations are present in this work. The first limitation being the small number of arteries studied. With only six arteries included in the CFD analysis, it is challenging to capture the total range of the hemodynamic parameters. Although the selected arteries did resemble the broader dataset of stenosed arteries in terms of size, length and amount of calcium bodies, this does not imply that the current

selection of six arteries is an accurate representation of the general population. Especially considering the fact that the intracranial ICA shows great geometric variety, even in healthy subjects. Gender affects the size, with greater diameters of the ICA found in men compared to women [32]. The anatomical side can also have an effect on the magnitude of the hemodynamics. In the region proximal to the intracranial ICA significant left-right differences were found, with higher WSS and OSI in the left-sided carotid artery bifurcation [50]. Such differences might also be present in the areas downstream from the bifurcation. To accurately represent the intracranial ICA, all these different aspects should be proportionally covered in the dataset. Therefore, six arteries is probably not a sufficient number.

Another shortcoming of this thesis is the use of a generic flow curve for the inlet boundary condition. This flow curve was based on an internal carotid artery of an average size, and was measured at the proximal part of the ICA [34]. The range in circumference of the arteries in this thesis was quite broad. Therefore, for the arteries on the further ends of the range, the flow curve used might have been a mismatch compared to the true physiological flow curves in these arteries. The arteries which had a small inlet surface area had the highest TAWSS values. The mismatch in flow curves could be a reason for the high TAWSS found in those arteries. An improved study design would include personalised flow curves, measured for each subject individually. This could be achieved by measuring the blood flow using MRI or Doppler ultrasound. Apart from the tendency to overestimate the magnitude of the hemodynamics, the distribution of the hemodynamics was only slightly affected by the generic flow curve. Therefore, the local areas of increased and decreased values still provide valuable information, albeit that the absolute values should be treated with some caution.

Although the results with respect to the calcium location could be verified by previous research, such justification was lacking for the results of the hemodynamic parameters. Unfortunately, little research has been performed on CFD analyses of the intracranial ICA of non-stenosed arteries. This complicated the interpretation of the TAWSS, RRT and OSI values that were retrieved from the simulations. Ideally, a validation process would have been incorporated into the study design. In such a process, in vivo or in vitro measurements of the blood flow and velocity for each artery should be performed and compared to the numerical results.

The current findings seem to point out that TAWSS is high and RRT is low in areas where calcifications of the intracranial ICA will develop. This conclusion was based on the comparison of the medians for the hemodynamic parameters between calcium-containing and calcium-free sectors but the significance of these findings has not been computed. A statistical test to prove significance and test for possible correlations would have been a valuable addition. However, a standard linear regression or t-test would not be sufficient for this analysis due to the hierarchical nature of the data.
The hemodynamic measurements were retrieved for each node of the mesh, which was thereafter mapped to the 2D maps. This resulted in as many data points as sectors per patient for each parameter. Given the number of sectors in total (N = 4216), a conventional regression analysis would reveal extremely optimistic p-values, as it would assume completely independent data. To resolve this, medians of the hemodynamic parameters per patient were used to compare the data. However, this substantially reduced the amount of data available for statistical analysis. The number of observations decreased from 907 calcium-containing sectors and 3309 calcium-free sectors to only 12 observations per parameter, corresponding to one median value for calcium-containing sectors and one for calcium-free sectors for each of the six arteries. With such a limited sample size, detecting statistically significant differences becomes unlikely.
Given the nature of the data in this study, using a mixed effects model would be a more suitable method to test for significance [48]. A mixed effects model would take into account the dependencies that exist within the data. Multiple dependencies were present in the data set, such as the patient and artery. Random effects model the dependent structure of the data. Instead of testing for significance on 4126 independent data points, the test would partition variability into between-cluster and within-cluster components. For example, the data points coming from one patient would be treated as a clustered data set. In this manner, the significance testing would account for within cluster dependence, while still making use of all available data points.

Lastly, there could be an improvement in the pipeline that was established. Reconstruction of the pre-calcified lumen mainly consisted of enlarging the lumens or reshaping the lumens. Enlargement of calcified lumens was often realised through the scaling method. While this method proved successful

to enlarge the stenosed sections of the calcified contours, it sometimes would decrease the size of other contours in the calcified region. In Appendix D this can be seen for Artery 1R and 4R. For both arteries the calcified lumen contours upstream of the stenosed section were larger compared to the unaffected, healthy contours. Unfortunately, the scaling method smoothed out such areas of local enlargement. Although this does not necessarily have to mean that the reconstruction was incorrect, the approach affected the geometry of the artery more than intended.
A possibility for refinement of the reconstruction methods lies in the procedure used to select the contours for reconstruction. In the current methods, contours to be reconstructed were solely based on the presence of calcium. However, the effect of calcium presence on the contour size and shape was not equal among all calcified contours. An attempt to ensure that calcium presence was associated with substantial lumen deformation was made by only selecting arteries with at least 70% stenosis. However, even within this selection of arteries, variability in the stenosis degree along the length of each artery remained. A different selection procedure or an additional check might be useful to be more precise and create better reconstructions. Another option would be to make use of available software packages to handle the reconstruction process.

4.4. Future outlook

If a relation between hemodynamics and intracranial carotid artery calcification exists, future protocols should be developed to evaluate the patient-specific hemodynamics in vivo. This would help clinicians find people at increased risk for intracranial calcification, allowing for early prevention or coordinating scheduled surveillance. Given the number of people suffering from ICAC and associated morbidities, such developments would be a valuable addition to the current diagnostic toolbox. But before these tools could be developed, more research is necessary on hemodynamics and intracranial calcification.

The current study design offers a unique solution to investigate the relation, since it enables the evaluation of hemodynamics specifically in areas where future calcifications will develop. The raw data required are CTA images, which are often created as part of routine clinical care. Given that the analyses can be performed with commonly available data makes the developed approach rather accessible. However, the study design is still in an early phase and needs more development. The exploratory findings of this work emphasise the need for further research, since the findings seem to contradict the usual pattern of low TAWSS and OSI in atheroprone regions. The true meaning of this result should be explored through new studies employing a larger data set and the correct statistical models.

In addition to research on hemodynamics, more focus could be placed on the geometry of the intracranial ICA. The curvature and the tortuosity have not been studied in this thesis, but they might be interesting parameters to evaluate in future studies.

5

Conclusion

This thesis provided a pipeline to create reconstructed, pre-calcified 3D models, derived from 2D CTA imaging data of patients with severe stenosis of the intracranial internal carotid artery. CFD simulations on the healthy 3D models revealed high TAWSS and low RRT in areas where calcifications were known to develop. A segment-wise analysis revealed an increase in TAWSS magnitude towards the distal end of the arteries. In contrast, the RRT demonstrated decreasing magnitudes in this direction. The OSI remained low, irrespective of the future presence of calcium or the anatomical segment. These initial findings seem to contradict the classical atheroprone hemodynamic pattern, characterised by low TAWSS, high OSI and high RRT. However, due to the limited size of the dataset and the lack of a statistical analysis, these findings should be treated with caution.

The pipeline developed offered a way to study hemodynamics in healthy surrogates of potentially predisposed arteries, which only required CTA imaging data as raw data. Although the methods used should be refined more, this pipeline could serve as a starting point for future research. Future research should indicate whether hemodynamics might be a suitable biomarker for ICAC. If so, non-invasive, in vivo measurements of hemodynamics could be a new diagnostic tool to find people at risk for ICAC early on. This might lead to intensified monitoring and preventive treatment, eventually minimising the negative effects associated with ICAC.

References

[1] Abbaspur A. *What is a Courant Number? (CFL Number)*. URL: https://cfdland.com/what-is-a-courant-number-cfl-number/ (visited on 12/09/2025).

[2] James Ahrens, Berk Geveci, and Charles Law. “ParaView: An End-User Tool for Large Data Visualization”. In: *Visualization Handbook*. Elsevier, 2005. ISBN: 9780123875822.

[3] Alzheimer’s Association. *2025 Alzheimer’s Disease Facts and Figures*. [Online]. Available: https://www.alz.org/getmedia/ef8f48f9-ad36-48ea-87f9-b74034635c1e/alzheimers-facts-and-figures.pdf. Accessed: Dec. 19, 2025. 2025.

[4] Gerard A Ateshian et al. “Finite element framework for computational fluid dynamics in FEBio”. In: *Journal of biomechanical engineering* 140.2 (2018), p. 021001.

[5] Autodesk, Inc. *Meshmixer*. Version 3.5.474. 2017.

[6] Roland Bammer et al. “Time-resolved 3D quantitative flow MRI of the major intracranial vessels: initial experience and comparative evaluation at 1.5 T and 3.0 T in combination with parallel imaging”. In: *Magnetic Resonance in Medicine: An Official Journal of the International Society for Magnetic Resonance in Medicine* 57.1 (2007), pp. 127–140.

[7] Bernhard P Berghout et al. “Burden of intracranial artery calcification in white patients with ischemic stroke”. In: *European Stroke Journal* 9.3 (2024), pp. 743–750.

[8] Bernhard P Berghout et al. “Morphometry of intracranial carotid artery calcifications in patients with recent cerebral ischemia”. In: *Journal of Clinical Medicine* 14.10 (2025), p. 3274.

[9] Tim C van den Beukel et al. “Intracranial arteriosclerosis and the risk of dementia: a population-based cohort study”. In: *Alzheimer’s & Dementia* 20.2 (2024), pp. 869–879.

[10] Michaela Binder and Charlotte A Roberts. “Calcified structures associated with human skeletal remains: Possible atherosclerosis affecting the population buried at Amara West, Sudan (1300–800 BC)”. In: *International Journal of Paleopathology* 6 (2014), pp. 20–29.

[11] Brett R Blackman, Guillermo García-Cardeña, and Michael A Gimbrone Jr. “A new in vitro model to evaluate differential responses of endothelial cells to simulated arterial shear stress waveforms”. In: *J. Biomech. Eng.* 124.4 (2002), pp. 397–407.

[12] Daniel Bos et al. “Atherosclerotic calcification relates to cognitive function and to brain changes on magnetic resonance imaging”. In: *Alzheimer’s & Dementia* 8 (2012), S104–S111.

[13] Daniel Bos et al. “Intracranial carotid artery atherosclerosis and the risk of stroke in whites: the Rotterdam Study”. In: *JAMA neurology* 71.4 (2014), pp. 405–411.

[14] Daniel Bos et al. “Intracranial carotid artery atherosclerosis: prevalence and risk factors in the general population”. In: *Stroke* 43.7 (2012), pp. 1878–1884.

[15] Alain Bouthillier, Harry R Van Loveren, and Jeffrey T Keller. “Segments of the internal carotid artery: a new classification”. In: *Neurosurgery* 38.3 (1996), pp. 425–433.

[16] Claudio Carallo et al. “Carotid endothelial shear stress reduction with aging is associated with plaque development in twelve years”. In: *Atherosclerosis* 251 (2016), pp. 63–69.

[17] Yuwen Chen et al. “Non-invasive assessment of intracranial wall shear stress using high-resolution magnetic resonance imaging in combination with computational fluid dynamics technique”. In: *Fundamental Research* 2.2 (2022), pp. 329–334.

[18] Zimo Chen et al. “Characteristics of wall shear stress and pressure of intracranial atherosclerosis analyzed by a computational fluid dynamics model: a pilot study”. In: *Frontiers in neurology* 10 (2020), p. 1372.

[19] Merih Cibis et al. “Relation between wall shear stress and carotid artery wall thickening MRI versus CFD”. In: *Journal of biomechanics* 49.5 (2016), pp. 735–741.

[20] Spyros Damaskos, Heraldo LD da Silveira, and Erwin WR Berkhout. “Severity and presence of atherosclerosis signs within the segments of internal carotid artery: CBCT’s contribution”. In: *Oral surgery, oral medicine, oral pathology and oral radiology* 122.1 (2016), pp. 89–97.

[21] Giuseppe De Nisco et al. “Modelling blood flow in coronary arteries: Newtonian or shear-thinning non-Newtonian rheology?” In: *Computer Methods and Programs in Biomedicine* 242 (2023), p. 107823.

[22] Heng Du et al. “Intracranial arterial calcification and intracranial atherosclerosis: close but different”. In: *Frontiers in neurology* 13 (2022), p. 799429.

[23] Gionata Fragomeni et al. “Newtonian and non-Newtonian blood model, a comparative study on large and small vessels”. In: *Proceedings of the International Conference on Modeling and Applied Simulation (MAS), Athens, Greece*. 2023, pp. 18–20.

[24] Diego Gallo et al. “Segment-specific associations between local haemodynamic and imaging markers of early atherosclerosis at the carotid artery: an in vivo human study”. In: *Journal of The Royal Society Interface* 15.147 (2018).

[25] Agostino Gnasso et al. “Association between intima-media thickness and wall shear stress in common carotid arteries in healthy male subjects”. In: *Circulation* 94.12 (1996), pp. 3257–3262.

[26] GridPro. *Different Types of Meshes in CFD*. URL: `https://gridpro.com/different-types-of-meshes-in-cfd` (visited on 05/23/2026).

[27] Krishnendu GS. *Understanding the CFL Number: Physical significance and Best Practices*. Feb. 26, 2025. URL: `https://www.flowthermolab.com/understanding-the-cfl-number-physical-significance-and-best-practices/`.

[28] Eline MJ Hartman et al. “Lipid-rich plaques detected by near-infrared spectroscopy are more frequently exposed to high shear stress”. In: *Journal of Cardiovascular Translational Research* 14.3 (2021), pp. 416–425.

[29] Richard Izzo et al. “The Vascular Modeling Toolkit: A Python Library for the Analysis of Tubular Structures in Medical Images”. In: *Journal of Open Source Software* 3.25 (2018), p. 745. DOI: `10.21105/joss.00745`. URL: `https://doi.org/10.21105/joss.00745`.

[30] Pim A de Jong et al. “The Carotid Siphon as a Pulsatility Modulator for Brain Protection: Role of Arterial Calcification Formation”. In: *Journal of Personalized Medicine* 15.8 (2025), p. 356.

[31] Muhsin Kizhisseri, Saleh Gharaie, and Jorg Schluter. “An analytical method informed by clinical imaging data for estimating outlet boundary conditions in computational fluid dynamics analysis of carotid artery blood flow”. In: *Scientific Reports* 13.1 (2023), p. 14973.

[32] Jaroslaw Krejza et al. “Carotid artery diameter in men and women and the relation to body and neck size”. In: *Stroke* 37.4 (2006), pp. 1103–1105.

[33] D N Ku et al. “Pulsatile flow and atherosclerosis in the human carotid bifurcation. Positive correlation between plaque location and low oscillating shear stress.” In: *Arteriosclerosis: An Official Journal of the American Heart Association, Inc.* 5.3 (1985), pp. 293–302. DOI: `10.1161/01.ATV.5.3.293`. eprint: `https://www.ahajournals.org/doi/pdf/10.1161/01.ATV.5.3.293`. URL: `https://www.ahajournals.org/doi/abs/10.1161/01.ATV.5.3.293`.

[34] Sang-Wook Lee et al. “Geometry of the carotid bifurcation predicts its exposure to disturbed flow”. In: *Stroke* 39.8 (2008), pp. 2341–2347.

[35] Thomas S Lee et al. “Management of carotid artery trauma”. In: *Craniomaxillofacial trauma & reconstruction* 7.3 (2014), pp. 175–189.

[36] S. A. Maas et al. “FEBio: Finite Elements for Biomechanics”. In: *Journal of Biomechanical Engineering* 134.1 (2012), p. 011005. DOI: `10.1115/1.4005694`.

[37] Adel M Malek, Seth L Alper, and Seigo Izumo. “Hemodynamic shear stress and its role in atherosclerosis”. In: *Jama* 282.21 (1999), pp. 2035–2042.

[38] Stephan Meckel et al. “Intracranial artery velocity measurement using 4D PC MRI at 3 T: comparison with transcranial ultrasound techniques and 2D PC MRI”. In: *Neuroradiology* 55.4 (2013), pp. 389–398.

[39] Writing Committee Members* et al. “2025 AHA/ACC/AANP/AAPA/ABC/ACCP/ACPM/AGS/AMA/ASPC/NMA/PCNA/SGIM guideline for the prevention, detection, evaluation and management of high blood pressure in adults: a report of the American College of Cardiology/American Heart Association Joint Committee on Clinical Practice Guidelines”. In: *Circulation* 152.11 (2025), e114–e218.

[40] Kevin M Moerman. “GIBBON: the geometry and image-based bioengineering add-on”. In: *Journal of Open Source Software* 3.22 (2018), p. 506.

[41] Maryam Paknahad et al. “Evaluation of the prevalence of atherosclerosis within the course of internal carotid artery in cone beam computed tomography images”. In: *Indian Journal of Otolaryngology and Head & Neck Surgery* 74.Suppl 3 (2022), pp. 5242–5251.

[42] Peter Patalano. “An oscillatory shear index-based model to describe progressive carotid artery stenosis”. In: *Vascular and Endovascular Surgery* 57.1 (2023), pp. 26–34.

[43] Jianxun Quan et al. “The role of hemodynamics in the formation of atherosclerotic plaques”. In: *Physics of Fluids* 37.1 (2025).

[44] Pritesh Ramya. “Reduced Order Modelling of Cerebral Vasculature”. MA thesis. Delft: Delft University of Technology, Aug. 2024.

[45] Paul Schoenhagen et al. “Arterial remodeling and coronary artery disease: the concept of “dilated” versus “obstructive” coronary atherosclerosis”. In: *Journal of the American College of Cardiology* 38.2 (2001), pp. 297–306.

[46] Jonas Schollenberger et al. “A combined computational fluid dynamics and arterial spin labeling MRI modeling strategy to quantify patient-specific cerebral hemodynamics in cerebrovascular occlusive disease”. In: *Frontiers in Bioengineering and Biotechnology* 9 (2021), p. 722445.

[47] T Schubert et al. “Dampening of blood-flow pulsatility along the carotid siphon: does form follow function?” In: *American journal of neuroradiology* 32.6 (2011), pp. 1107–1112.

[48] Leda Tomiko Yamada da Silveira, Juliana Carvalho Ferreira, and Cecilia Maria Patino. “Mixed-effects model: a useful statistical tool for longitudinal and cluster studies”. In: *Jornal Brasileiro de Pneumologia* 49.2 (2023), e20230137.

[49] Christoph Strecker et al. “Carotid geometry and wall shear stress independently predict increased wall thickness—a longitudinal 3D MRI study in high-risk patients”. In: *Frontiers in Cardiovascular Medicine* 8 (2021), p. 723860.

[50] Christoph Strecker et al. “Carotid geometry is an independent predictor of wall thickness – a 3D cardiovascular magnetic resonance study in patients with high cardiovascular risk”. In: *Journal of Cardiovascular Magnetic Resonance* 22.1 (2020), p. 67. ISSN: 1097-6647. DOI: https://doi.org/10.1186/s12968-020-00657-5. URL: https://www.sciencedirect.com/science/article/pii/S1097664723003198.

[51] Shigekazu Takeuchi and Takeshi Karino. “Flow patterns and distributions of fluid velocity and wall shear stress in the human internal carotid and middle cerebral arteries”. In: *World neurosurgery* 73.3 (2010), pp. 174–185.

[52] The MathWorks, Inc. *MATLAB*. Version 23.2.0.2859533 (R2023b). Natick, Massachusetts, 2023.

[53] George B Thurston. “Rheological parameters for the viscosity viscoelasticity and thixotropy of blood”. In: *Biorheology* 16.3 (1979), pp. 149–162.

[54] Rick J van Tuijl et al. “Velocity pulsatility and arterial distensibility along the internal carotid artery”. In: *Journal of the American Heart Association* 9.16 (2020), e016883.

[55] Tim C Van Den Beukel et al. “Morphological subtypes of intracranial internal carotid artery arteriosclerosis and the risk of stroke”. In: *Stroke* 53.4 (2022), pp. 1339–1347.

[56] Bernard J van Varik et al. “Mechanisms of arterial remodeling: lessons from genetic diseases”. In: *Frontiers in genetics* 3 (2012), p. 290.

[57] Annelotte Vos et al. “Risk factors for atherosclerotic and medial arterial calcification of the intracranial internal carotid artery”. In: *Atherosclerosis* 276 (2018), pp. 44–49.

[58] Xiao-Bing Wu et al. “Hemodynamics combined with inflammatory indicators exploring relationships between ischemic stroke and symptomatic middle cerebral artery atherosclerotic stenosis”. In: *European Journal of Medical Research* 28.1 (2023), p. 378.

[59] Shuwan Xu et al. “Mechanism analysis of vascular calcification based on fluid dynamics”. In: *Diagnostics* 13.16 (2023), p. 2632.

[60] Wen-Jie Yang et al. “Postmortem study exploring distribution and patterns of intracranial artery calcification”. In: *Stroke* 49.11 (2018), pp. 2767–2769.

[61] C K Zarins et al. “Carotid bifurcation atherosclerosis. Quantitative correlation of plaque localization with flow velocity profiles and wall shear stress.” In: *Circulation Research* 53.4 (1983), pp. 502–514. DOI: 10.1161/01.RES.53.4.502. eprint: https://www.ahajournals.org/doi/pdf/10.1161/01.RES.53.4.502. URL: https://www.ahajournals.org/doi/abs/10.1161/01.RES.53.4.502.

[62] Chi Zhang et al. “Flow patterns and wall shear stress distribution in human internal carotid arteries: the geometric effect on the risk for stenoses”. In: *Journal of biomechanics* 45.1 (2012), pp. 83–89.

[63] Chi Zhang et al. “Geometric classification of the carotid siphon: association between geometry and stenoses”. In: *Surgical and radiologic anatomy* 35.5 (2013), pp. 385–394.

A

Boundary Conditions

A.1. Outlet pressure

At the outlet, a fluid resistance boundary condition was applied. In total, four different arrangements were tested on Artery 2R to select the most suitable boundary condition. Since Artery 2R represented the average size of the six arteries, this artery was chosen. All of these options ensured that the fluid pressure changed in response to the blood flow. Apart from the pressure BC, all other boundary conditions were kept similar between the different models.

For the first three options, the pressure was derived from the following equation:

$$P = RQ + P_o \tag{A.1}$$

With parameter R as a measure to describe the resistance of the fluid to flow. For the first option, this parameter was retrieved from a study by Kizhisseri et al. [31]. They analytically derived the fluid resistance value using geometry data of clinical images. For the second option, the value was calculated using a method described by P. Ramya [44]. Following this method, Equation A.1 is formulated twice, first using a systolic pressure (120 mmHg) and the maximum flow rate for P and Q, and second using a diastolic pressure (80 mmHg) and the minimum flow rate. The values for P_o and R are derived by solving this linear system of equations. The third option was provided by a F.Fontana, who had computed the values using the aforementioned method. Thus, options 2 and 3 used the same approach, but different values were assumed for P_o and R. The calculated offset pressures from options 2 and 3 were 75 mmHg and 115 mmHg, respectively. Both were reasonably within the range of physiological values (80-120 mmHg).

For the last option, the pressure was derived from the three-element Windkessel model (Equation A.2). This equation describes fluid flow using an electrical circuit analogy. Compared to Equation A.1, this equation accounted for differences in fluid resistance between the proximal and distal vasculature with respect to the outlet of the artery. Here R_P represents the proximal fluid resistance while R_d represents the distal fluid resistance. The values for both resistance values were retrieved from an in vivo study by Schollenberger et al.[46].

$$Q(1 + \frac{R_P}{R_d}) + CR_P\frac{dQ}{dt} = \frac{P}{R_d} + C\frac{\Delta P}{dt} \tag{A.2}$$

Due to the nature of CFD simulations, the walls of the artery and the distal vasculature, which was not included in the model, were considered rigid. Therefore, the capacitance (C) was set to zero. In FEBio, the fluid RCR setting was used at the outlet. Since options 1 and 4 did come with an offset value, a value of 10640 Pa was set, corresponding to 80 mmHg. The parameters and corresponding values for all four options are shown in Table A.1.

Table A.1: Parameter values for the pressure boundary conditions at the outlet. Options 1–3 use a resistance model, Option 4 uses an RCR model.

	R (kg/m^{4}s)	**R_d (kg/m^{4}s)**	**P_o (Pa)**
Option 1	5.98 x 10^7		10640
Option 2	1.13 x 10^9		15500
Option 3	6.67 x 10^8		10000
Option 4	9.66 x 10^8	8.90 x 10^8	10640

The pressure drop (ΔP) was determined for all four simulations. By subtracting the pressure values at the outlet from the values at the inlet, the pressure drop was computed. For all simulations, the maximum pressure drop and minimum pressure drop were selected, corresponding to the pressure drop at peak-systole (ΔP_{sys}) and end-diastole (ΔP_{dia}), respectively. A slight pressure drop was expected due to the tortuosity of the artery and the viscosity of blood, leading to frictional forces. However, a ΔP greater than 10 mmHg would suggest inaccuracies in the boundary conditions. Therefore, options resulting in pressure drop values above 1330 Pa were considered too large and not suitable for the simulations.

Table A.2: Pressure drop values for all four options. The values were measured at peak-systole and end-diastole.

	ΔP_{sys} (Pa)	**ΔP_{dia} (Pa)**
Option 1	872	161
Option 2	748	161
Option 3	741	160
Option 4	745	161

As demonstrated in Table A.2, all pressure drop values were below the cut-off value. An additional analysis was performed to establish whether the resulting pressures corresponded to physiological values. Pressure values were deemed physiological if they ranged from 80 mmHg at diastole to 120 mmHg at systole [39].

Table A.3: Maximum absolute pressure values at systole and diastole for all four options.

	P_o (mmHg)	**Max P_{sys} (mmHg)**	**Max P_{dia} (mmHg)**
Option 1	80	88	82
Option 2	112	154	130
Option 3	75	100	83
Option 4	80	123	104

Only options 1, 3, and 4 were within the physiological range, as shown in Table A.3. Option 2 demonstrated values above 120 mmHg and was therefore not suitable as a BC for a healthy simulation. Option 1 fell within the specified range, but the difference between the systolic and diastolic pressure was minimal. Therefore, this option was also deemed not representable for a healthy artery. Options 3 and 4 both showed acceptable values. Thus, for the final simulations, option 3 was selected.

A.2. Inlet velocity

At the inlet, two different pulsatile velocity curves were considered. The first velocity curve was based on an average pulsatile flow curve described by Lee et al.[34]. From the flow curve, velocity values were retrieved by dividing the flow magnitudes by the size of the inlet area of the artery.

The second velocity curve was derived from in vivo MRI measurements by Bammer et al.[6]. They measured the blood velocity at the C2 segment of the ICA in healthy people. This curve was directly

applied as the inlet condition. Compared to the first curve, the Bammer curve shows lower velocity values. Both curves are shown in Figure A.1.

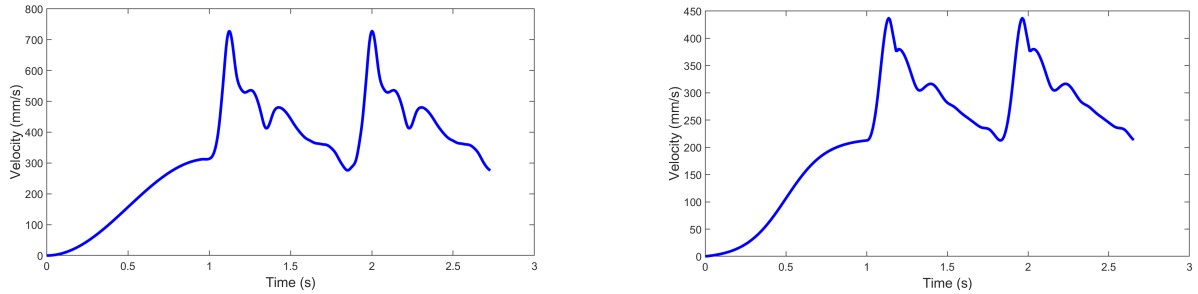

(a) Lee curve

(b) Bammer curve

Figure A.1: The Lee curve and Bammer curve over two cardiac cycles. A sigmoid curve was used to gradually reach the minimum velocity of the velocity curve.

To determine which of the two velocity curves was most suitable for the simulations, two test runs were performed on Artery 2R. For both runs, the outlet pressure condition of Option 3, as mentioned in Table A.1, was prescribed. Velocity values at different locations along the ICA were retrieved and compared to velocity values reported by literature, shown in Table A.4.

For segments C2, C5 and C6, the maximum blood velocity was retrieved at the peak of systole and the end of diastole. At end-diastole, the Lee and Bammer curves were both close to the velocity values found in literature. However, at peak-systole, the Bammer curve resulted in velocity values much lower than the literature values. The Lee curve also seemed to underestimate the velocity values. However, the measured velocities deviated less from the literature values. Therefore, the Lee curve was chosen as the inlet condition for the final simulations.

Table A.4: The maximum velocities during peak-systole (v_{sys}) and end-diastole (v_{dia}) in segments C2, C5, and C6 of the internal carotid artery. The literature values were measured in healthy subjects.

Segment	$\mathbf{v_{dia}}$ (mm/s)			$\mathbf{v_{sys}}$ (mm/s)		
	Literature	*Lee*	*Bammer*	*Literature*	*Lee*	*Bammer*
C2	209±47[6]	174	221	384±102[6]	595	441
C5	150–250[38]	282	265	700–900[38]	682	518
C6	200–300[38]	312	291	800–1000[38]	954	611

A.3. Effect of adjusted flow curve

To examine the effect of adjusting the flow curve to the size of the individual artery, an additional simulation was performed. Following the method of Lee et al., the average curve was scaled using the following equation:

$$Q_{artery} = Q_{avg} * \frac{A_{artery}}{A_{avg}}$$

Here, Q_{avg} was the flow curve of an average-sized artery, as provided by Lee et al. A_{artery} was the cross-sectional surface area at the inlet of the individual artery, and A_{avg} was the average cross-sectional surface area of the internal carotid artery. Artery 5L was used for this simulation because it exhibited the largest TAWSS magnitude of all arteries when the average flow curve was used. A_{5L} at the inlet was 10 mm^2. For A_{avg}, a value of 17 $mm2^2$ was used, which corresponded to a mean diameter of the ICA in women [32].

In Table A.5, the resulting differences in maximum inlet flow (Q_{max}), maximum inlet velocity (v_{max}), and maximum time-averaged wall shear stress ($TAWSS_{max}$) are shown.

Table A.5: The resulting maximum flow rate, velocity and TAWSS corresponding to the average and the adjusted flow curve.

Flow curve	Q_{max} inlet (mm^3/s)	v_{max} inlet (mm/s)	$TAWSS_{max}$ (Pa)
Q_{avg}	7589	728	70
Q_{5L}	4648	447	34

The adjusted curve resulted in lower maximum values for the hemodynamic parameters. However, the 2D maps revealed minimal change in the distribution of the hemodynamic parameters along the artery, as shown in Figure A.2. Therefore, the original flow curve corresponding to the average-sized ICA was eventually used.

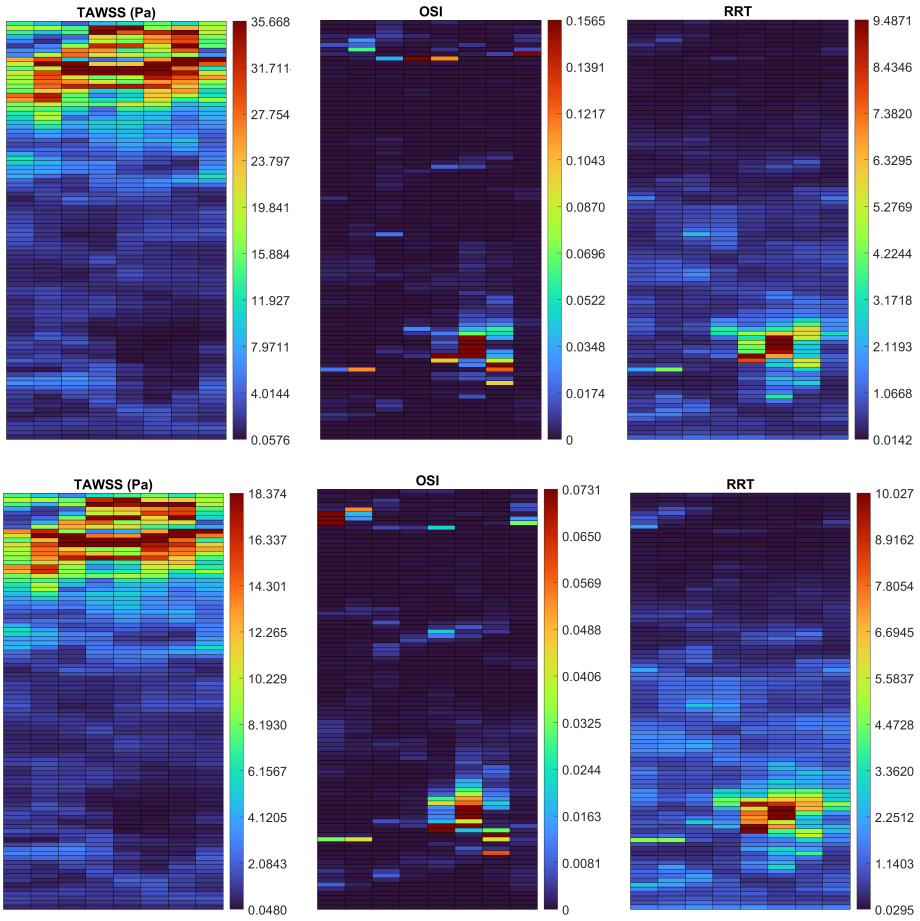

Figure A.2: 2D maps of the TAWSS, OSI and RRT from simulations run with the average and the adjusted flow curve.

B

Mesh convergence analysis

The mesh convergence analysis was performed on the global and local mesh. The global mesh was used for the majority of the arterial lumen, while the local mesh was used in the boundary layer.

A simpler model was used to determine the effect of the mesh properties on the output variables. For this model, Artery 5L was used. The inlet velocity was kept constant at 250 mm/s and the pressure was fixed at 13300 Pa (corresponding to 100 mmHg) at the outlet. The time step used was 0.001 seconds.

Quantities of interest were related to the blood velocity at the inlet and outlet of the artery, as well as the fluid pressure. The effect of larger element sizes was quantified by computing the percentage change between the least coarse mesh and the coarse mesh of interest, as shown in Equation B.1. With M_f and M_c being the outcome quantities of the the fine and the coarse mesh, respectively.

$$\Delta\% = \frac{|M_f - M_c|}{\frac{M_f + M_c}{2}} * 100\% \tag{B.1}$$

A percentage change of 1-5$\%$ was deemed an acceptable value. Values above 5$\%$ were deemed too far off the least coarse mesh. Hence, meshes that resulted in a percentage change >5$\%$ were qualified as too coarse and not suitable for the simulation.

B.1. Global mesh

To determine the effect of the element size, simulations were run with prescribed element sizes of 0.15, 0.2, 0.25, 0.3, and 0.35 millimeters, while keeping the boundary layer mesh unchanged. Table B.1 illustrates the edge lengths that correspond with the different element sizes.

Table B.1: Element size settings for the tetrahedra elements of the different global meshes.

Element size	No. of elements	Average edge length (mm)	Max edge length (mm)
0.35	165 874	0.333	0.477
0.30	242 377	0.289	0.412
0.25	382 397	0.243	0.357
0.20	677 508	0.197	0.290
0.15	1 445 637	0.149	0.221

Pressure drop, inlet pressure, and the blood velocity were analysed for all of the global mesh runs. By subtracting the pressure values at the outlet from the values at the inlet, the pressure drop was computed. In Table B.2, the results are shown. The mesh with the largest element size of 0.35 mm did not reach convergence, and the simulation resulted in an error termination. The meshes with smaller

element sizes all converged and demonstrated a small effect on the quantities of interest. Only the 0.3 mesh demonstrated a percentage change >5% for the pressure drop. The 0.2 and 0.25 mesh both demonstrated percentage changes within the acceptable range for all the quantities of interest. Therefore, an element size of 0.25 was chosen for the final mesh.

Table B.2: Results of different element size settings for the tetrahedra elements.

Element size	v_{avg} outlet (mm/s)	△%	P_{avg} inlet (Pa)	△%	△P (Pa)	△%
0.35						
0.30	913.76	1.21	16 514	1.24	3212	6.46
0.25	906.60	0.42	16 461	0.92	3161	4.86
0.20	906.35	0.39	16 380	0.43	3080	2.27
0.15	902.79		16 310		3011	

B.2. Local mesh

At the boundary of the lumen a local mesh was used, consisting of pentahedron elements. A layer thickness of 0.1 mm was set, with a bias value of 2. This ensured that the boundary layers increased in thickness closer to the centre of the lumen. To analyse the boundary layer mesh, the number of boundary layers was altered to compare three different meshes. The element size of the global mesh was kept at 0.25 mm. The effects of changes in the local mesh were analysed by looking at the average velocity at the outlet of the artery, as well as the average pressure at the inlet and the pressure drop. The results of the three different local meshes are shown in Table B.3.

Table B.3: Results of the boundary layer refinement.

Layers	v_{avg} outlet (mm/s)	△%	P_{avg} inlet (Pa)	△%	△P (Pa)	△%
4	910.45	0.38	16 536	0.30	3234	1.69
5	913.76	0.02	16 514	0.18	3212	0.97
6	913.90		16 485		3183	

As evident from Table B.3, the amount of boundary layers exerts a minimal effect on the outcome measures. With all outcomes being well within the acceptable range of the percentage change, the final amount of boundary layers was set at five.

C

Time step

To determine an appropriate size for the time step, the Courant-Friedrichs-Lewy(CFL) number was first determined. The CFL number is a dimensionless number which must stay beneath a value of 1 to ensure stability and accuracy of a numerical simulation. When this condition is violated, information, such as the velocity or pressure, travels more than one mesh element per time step. Such a phenomenon could lead to inaccurate results and divergence.
The cut-off value is used a strong limit for explicit solvers, while the limit is more loose in case of an implicit solver. For implicit solvers, this number can be in the range of 5-50 [1]. The CFL-number is derived from the maximum velocity through a mesh element multiplied by the time step and the inverse of the characteristic length of an element, as shown in Equation C.1. With dt = time step in seconds, U = maximum velocity in m/s and dx = the edge length of an element in meters.

$$CFL = U \cdot \frac{dt}{dx} \tag{C.1}$$

To estimate the size of the time step, the maximum velocity measured in Artery 5L was used as an input. This artery was selected because it had a relatively small lumen, thus velocities were expected to reach high values. For dx, the average edge length of the global mesh was chosen. A CFL-number of 1 was used for a conservative estimation of the time step. This resulted in dt = 0.00005 s. However, since FEBio utilises an implicit solver, the CFL-number was allowed to be greater than than 1. Therefore, a few larger time steps were also analysed: 0.01, 0.001, 0.0001 s.

Table C.1: The effect of using different time step sizes on velocity and pressure values at the in- and outlet of the artery.

Time step (s)	v_{avg} inlet (mm/s)	v_{avg} outlet (mm/s)	P_{avg} inlet (Pa)	$\triangle$P (Pa)
0.01	250	914	16 514	3212
0.001	250	914	16 514	3212
0.0001	250	914	16 514	3212
0.000 05	250	914	16 514	3212

As evident from Table C.1, increasing the time step size did not affect the velocity and pressure values. However, the time step of 0.01 seconds did lead to divergence issues. Therefore, to increase the stability of the simulations while minimising computational costs, a time step size of 0.001 seconds was chosen, corresponding to a CFL-number of 20.

D

Reconstructions

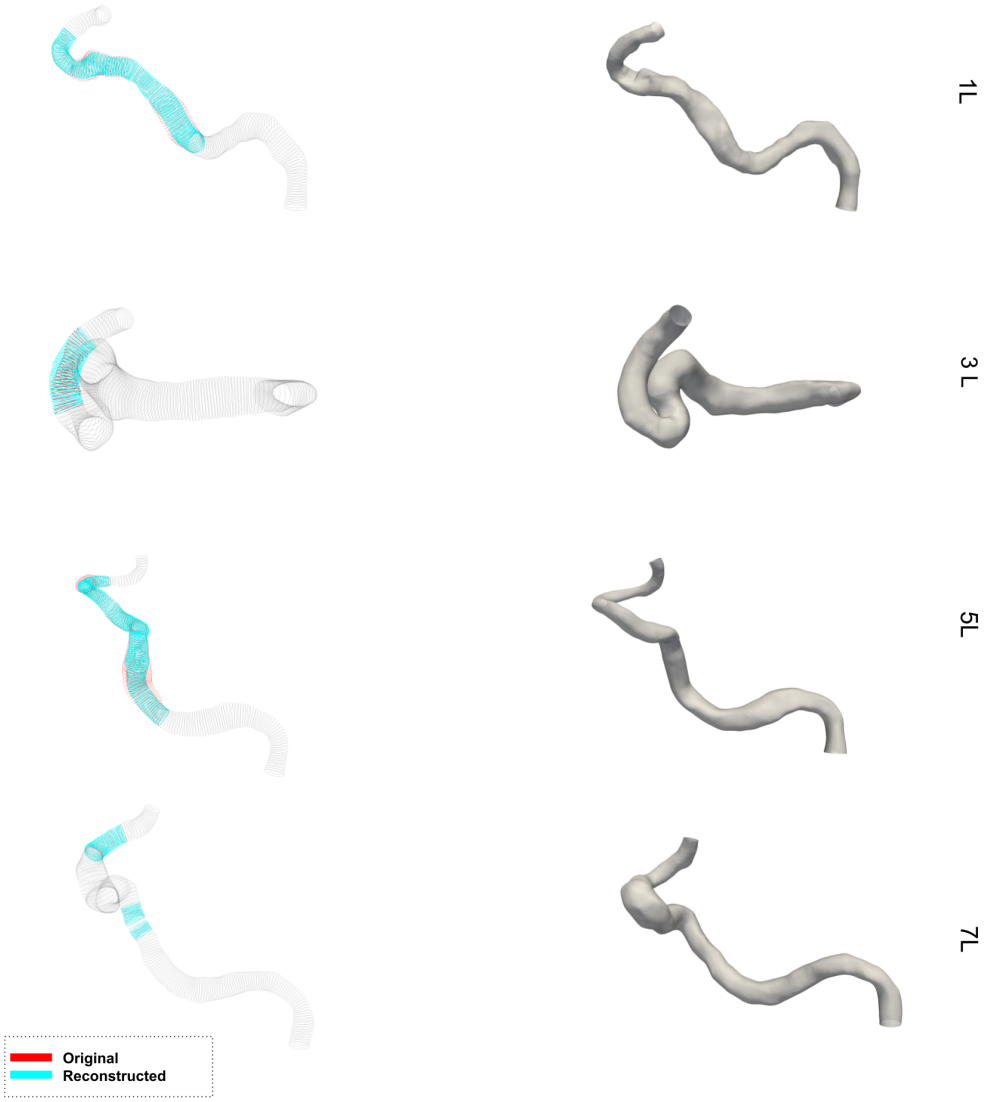

Figure D.1: Reconstruction results for the left arteries, lateral view. On the left, the lumen contours are shown. Grey = original unaffected contours; Red = original contours affected by calcium; Cyan = reconstructed contours. On the right, the final reconstructed lumens are shown. For Artery 3L, a top view is shown since this visualised the reconstructed region best.

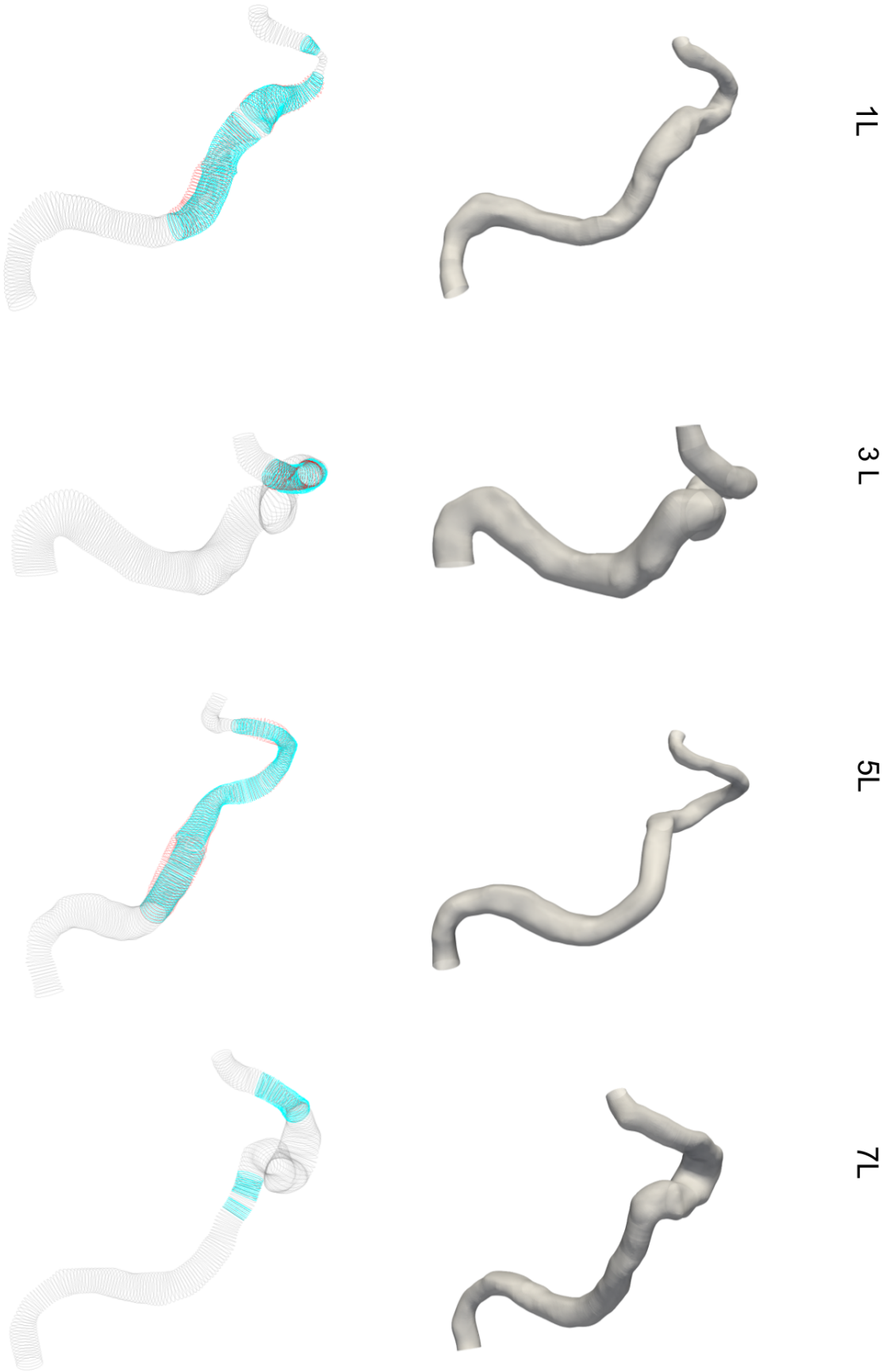

Figure D.2: Reconstruction results for the left arteries, medial view. On the left, the lumen contours are shown. Grey = original unaffected contours; Red = original contours affected by calcium; Cyan = reconstructed contours. On the right, the final reconstructed lumens are shown.

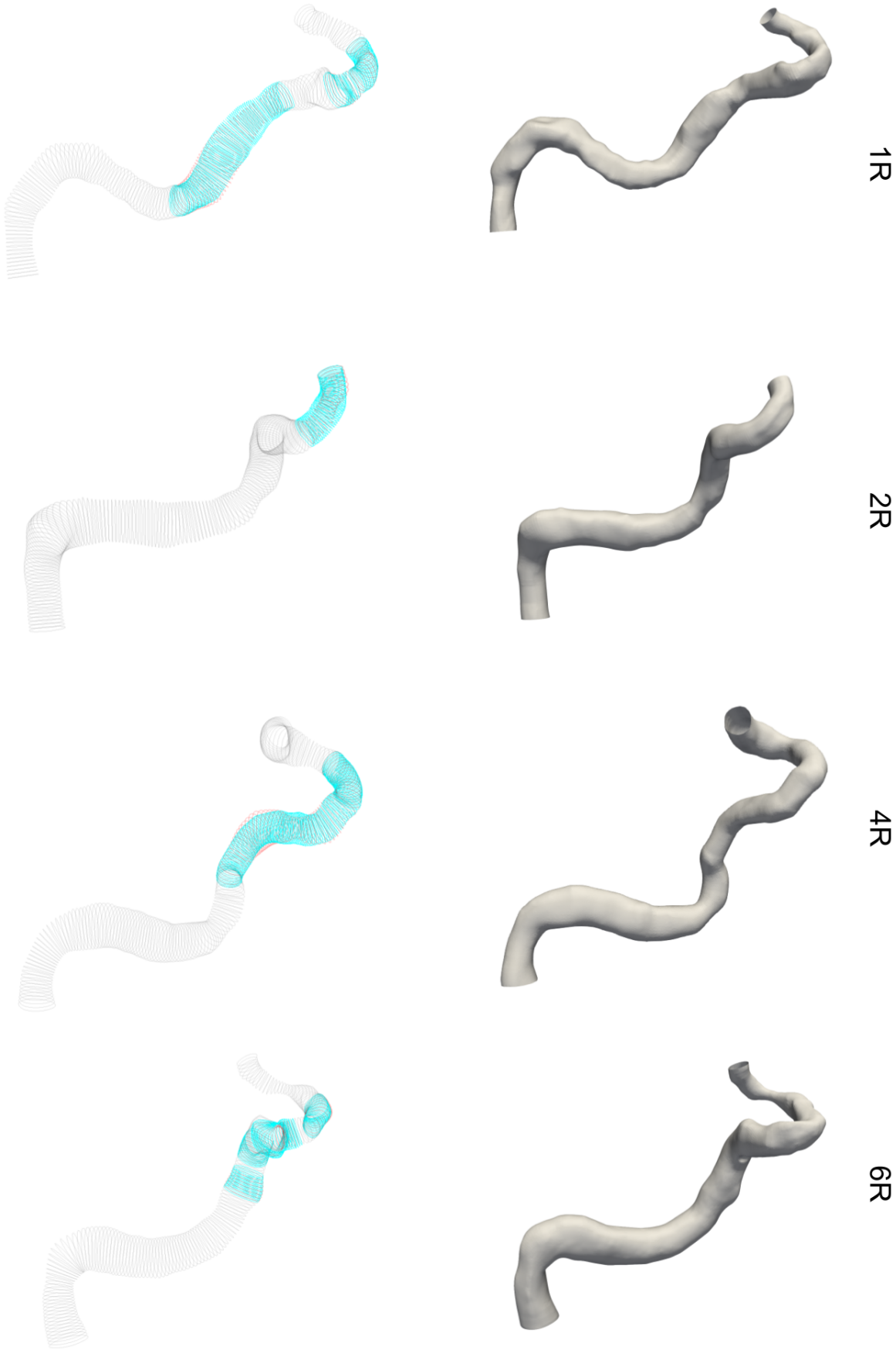

Figure D.3: Reconstruction results for the right arteries, lateral view. On the left, the lumen contours are shown. Grey = original unaffected contours; Red = original contours affected by calcium; Cyan = reconstructed contours. On the right, the final reconstructed lumens are shown.

Figure D.4: Reconstruction results for the right arteries, medial view. On the left, the lumen contours are shown. Grey = original unaffected contours; Red = original contours affected by calcium; Cyan = reconstructed contours. On the right, the final reconstructed lumens are shown.

E

Results

E.1. Artery 1R

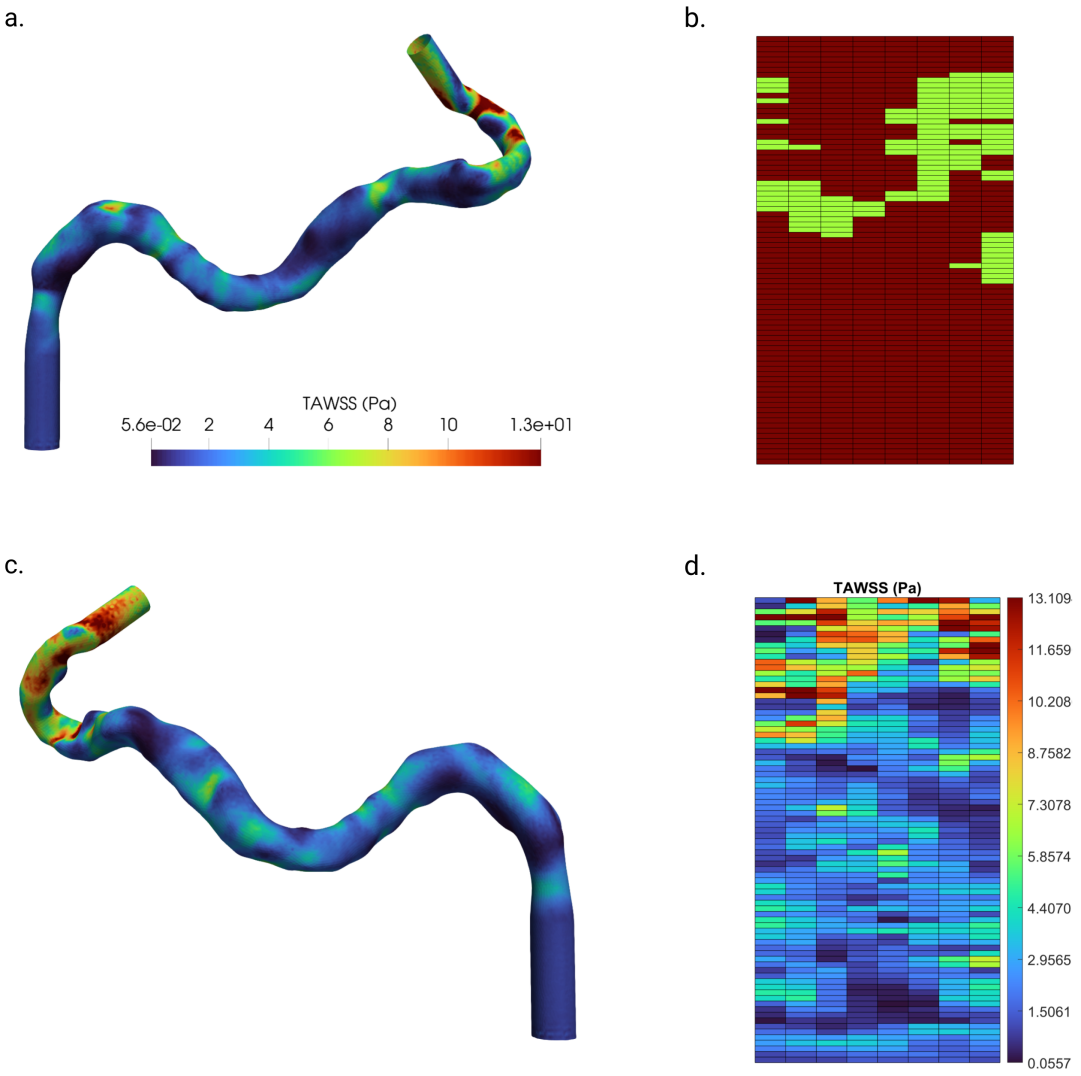

Figure E.1: TAWSS of Artery 1R in Pa. a) Lateral view of the TAWSS. b) 2D map of the calcium presence. c) Medial view of the TAWSS. d) 2D map of the TAWSS.

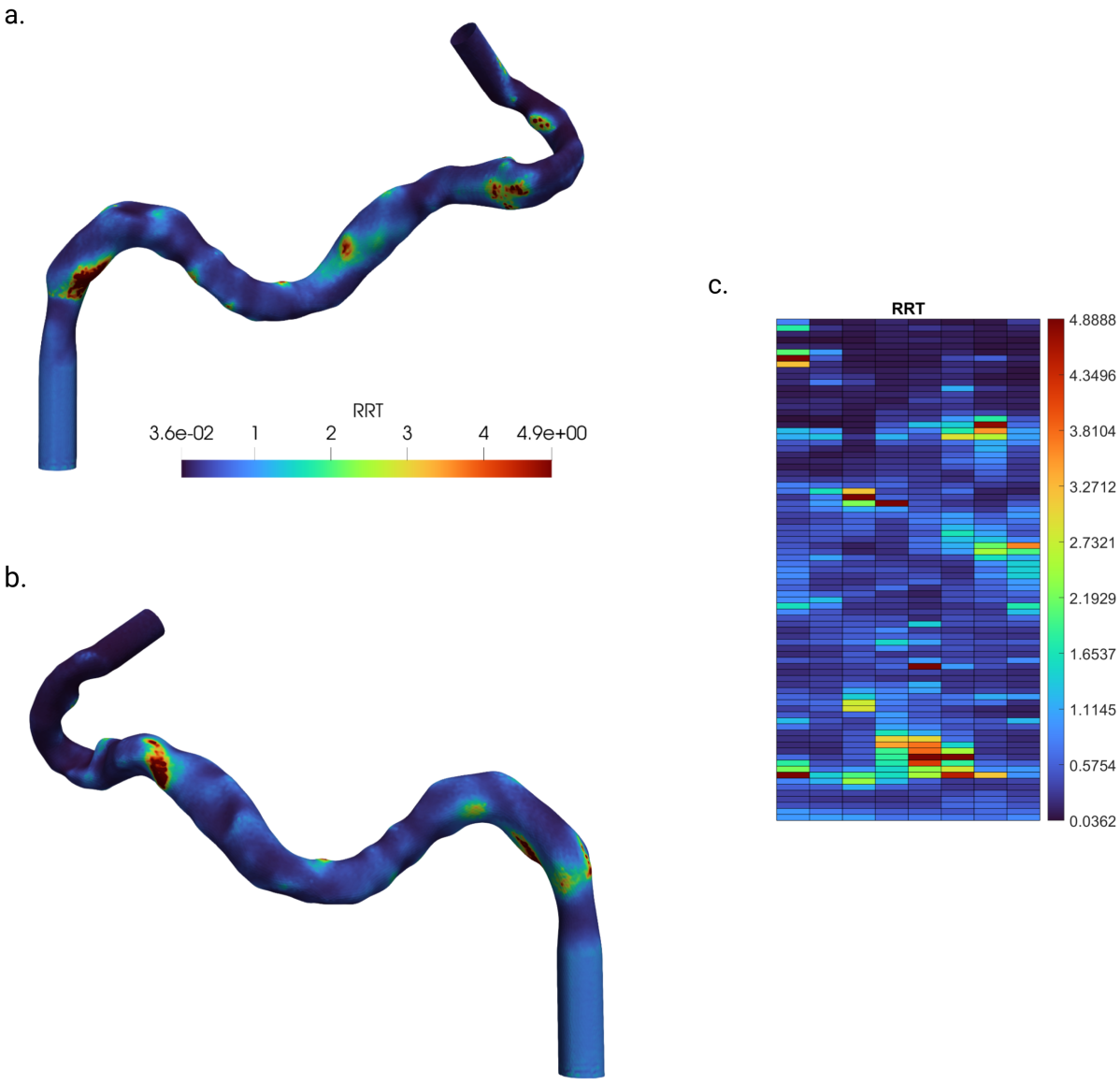

Figure E.2: RRT of Artery 1R. a) Lateral view of the RRT. b) Medial view of the RRT. c) 2D map of the RRT.

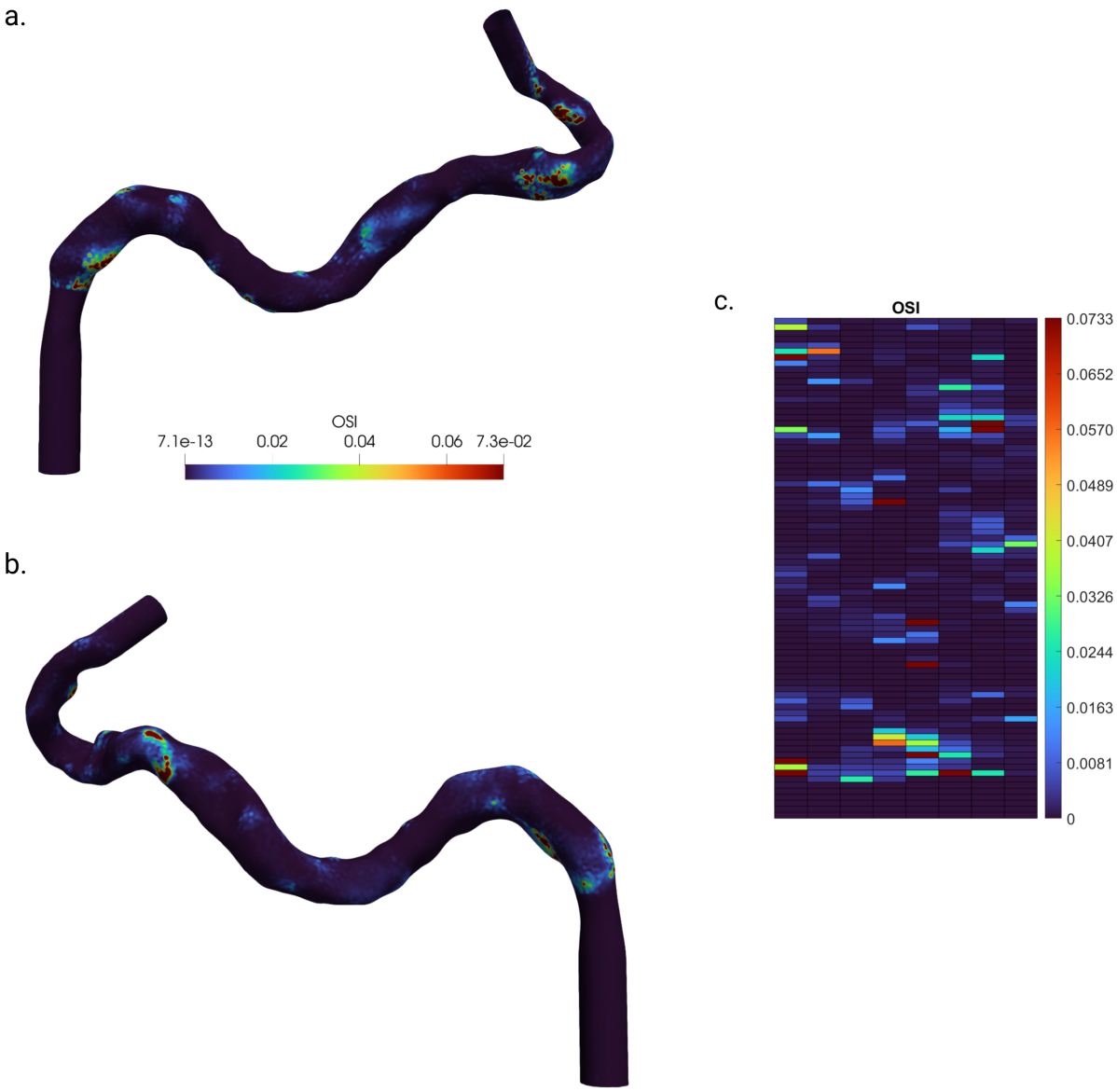

Figure E.3: OSI of Artery 1R. a) Lateral view of the OSI. b) Medial view of the OSI. c) 2D map of the OSI.

E.2. Artery 1L

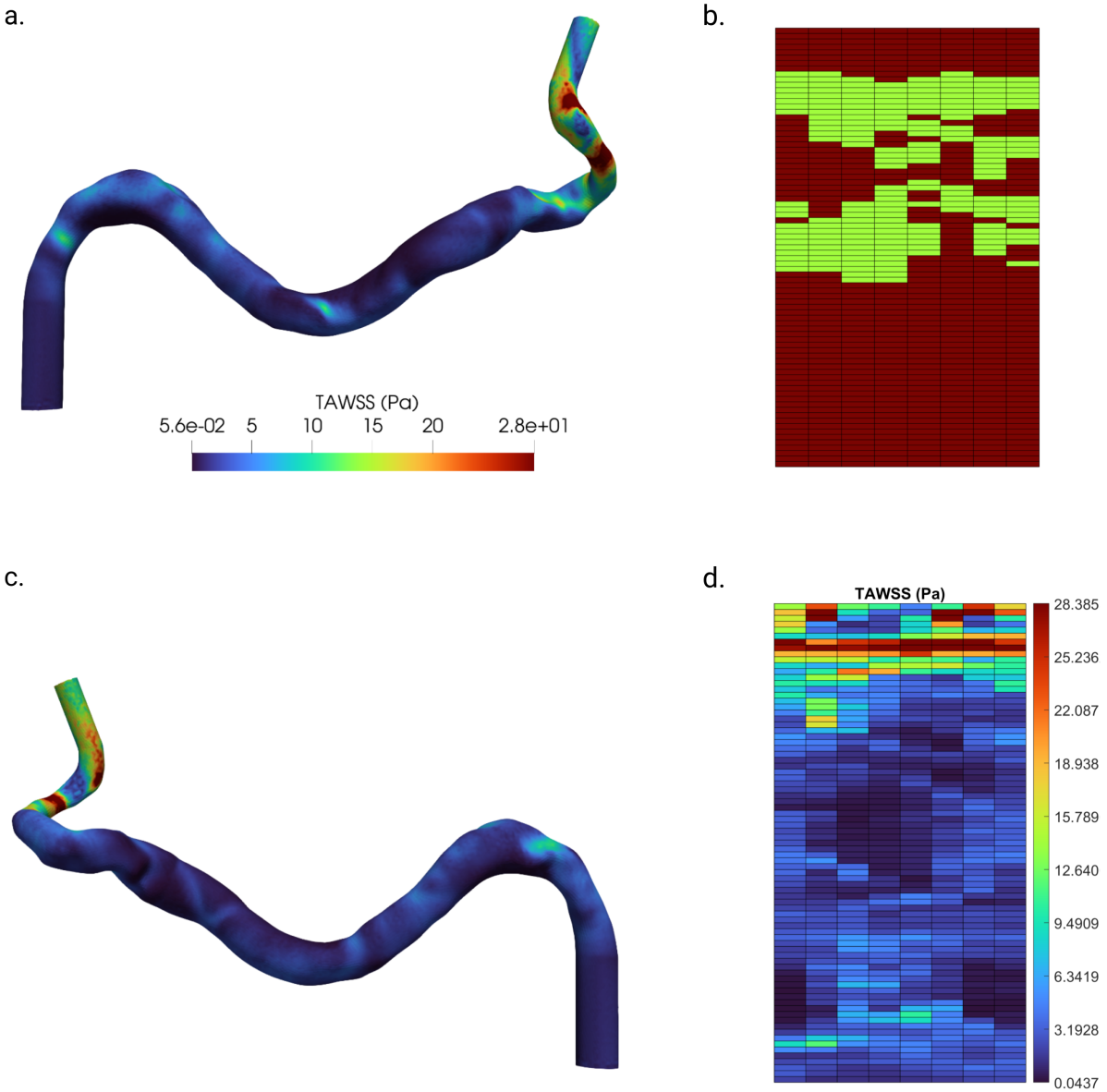

Figure E.4: TAWSS of Artery 1L in Pa. a) Medial view of the TAWSS. b) 2D map of the calcium presence. c) Lateral view of the TAWSS. d) 2D map of the TAWSS.

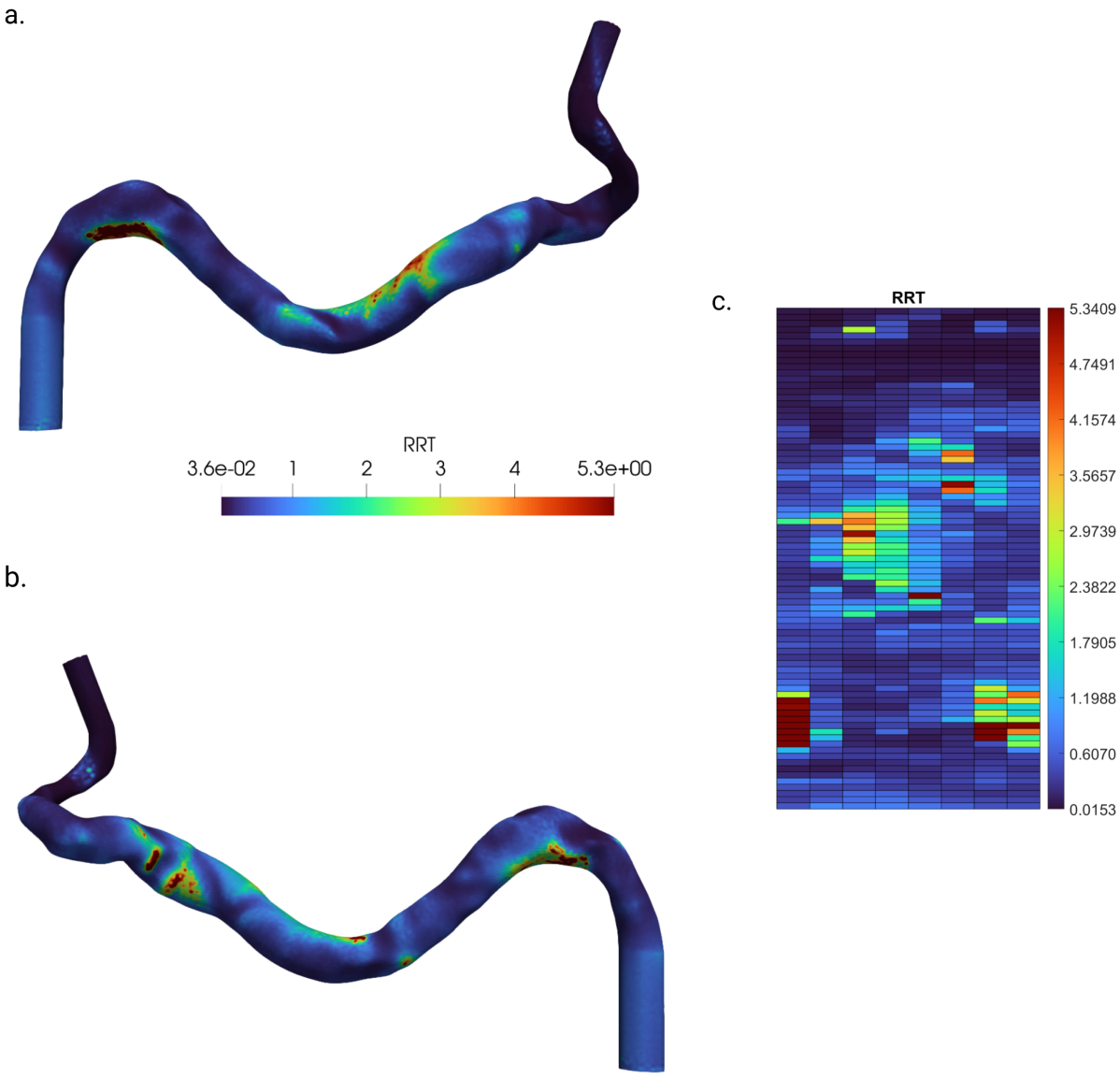

Figure E.5: RRT of Artery 1L. a) Medial view of the RRT. b) Lateral view of the RRT. c) 2D map of the RRT.

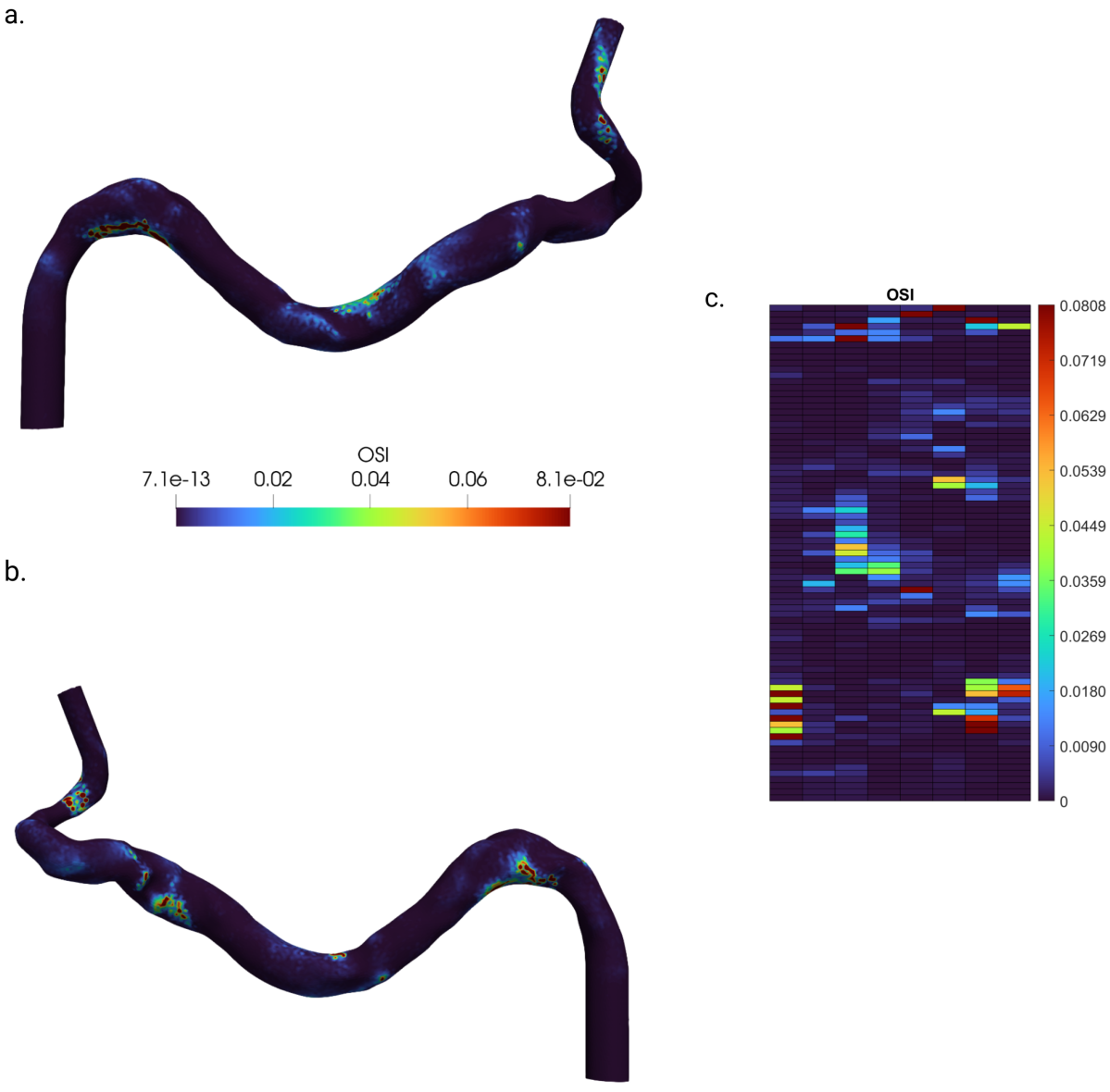

Figure E.6: OSI of Artery 1L. a) Medial view of the OSI. b) Lateral view of the OSI. c) 2D map of the OSI.

E.3. Artery 2R

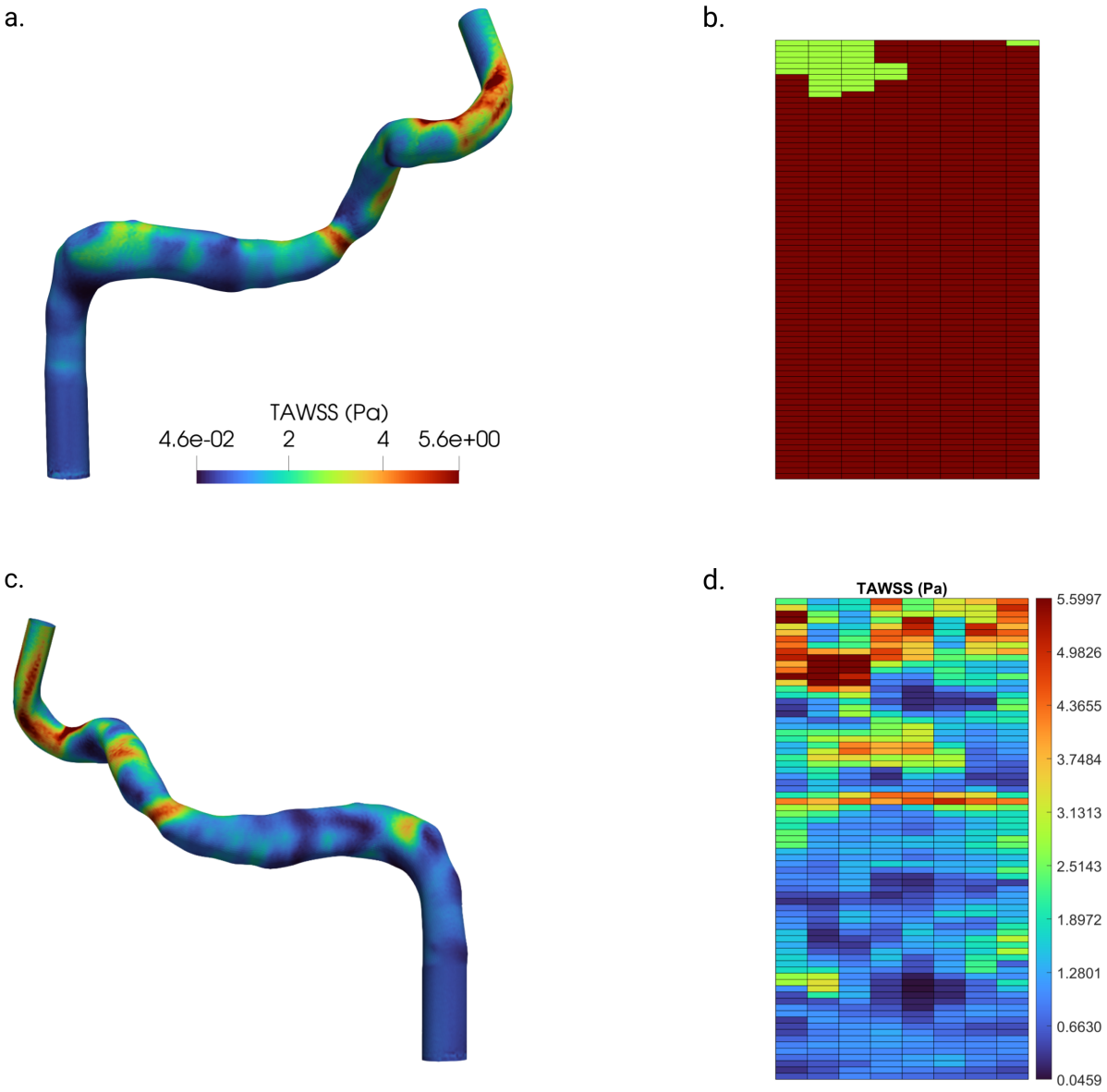

Figure E.7: TAWSS of Artery 2R in Pa. a) Lateral view of the TAWSS. b) 2D map of the calcium presence. c) Medial view of the TAWSS. d) 2D map of the TAWSS.

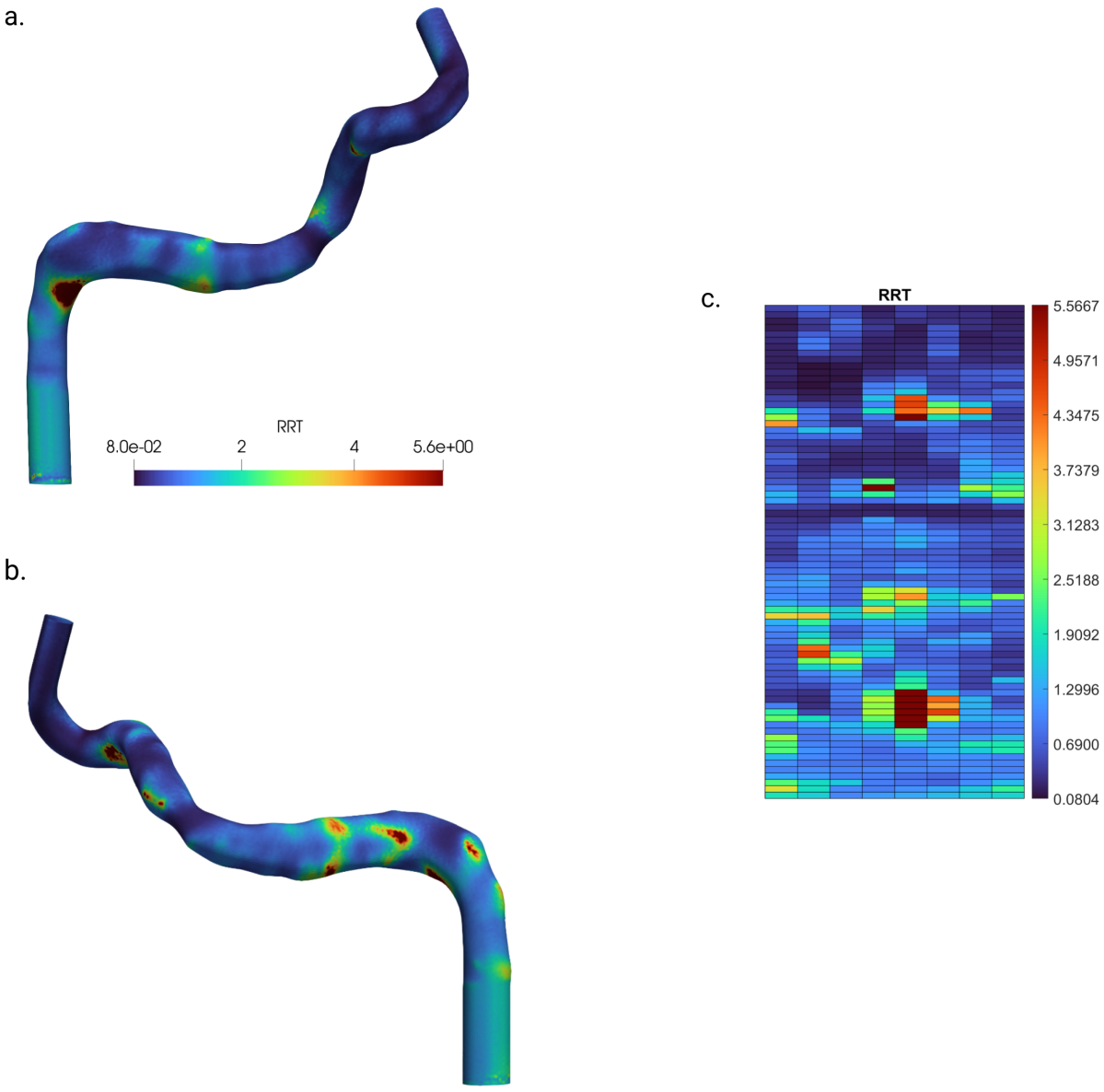

Figure E.8: RRT of Artery 2R. a) Lateral view of the RRT. b) Medial view of the RRT. c) 2D map of the RRT.

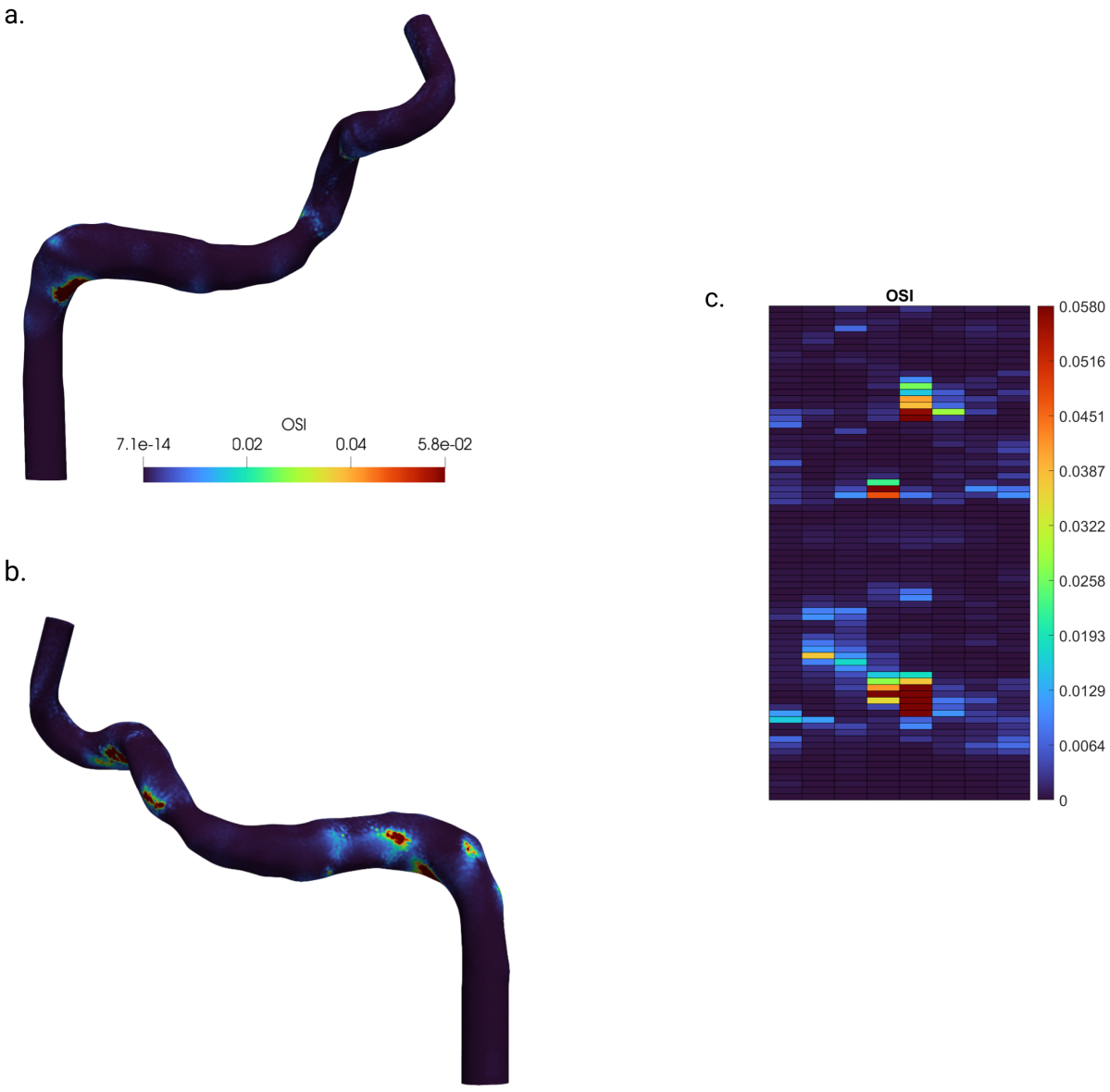

Figure E.9: OSI of Artery 2R. a) Lateral view of the OSI. b) Medial view of the OSI. c) 2D map of the OSI.

E.4. Artery 3L

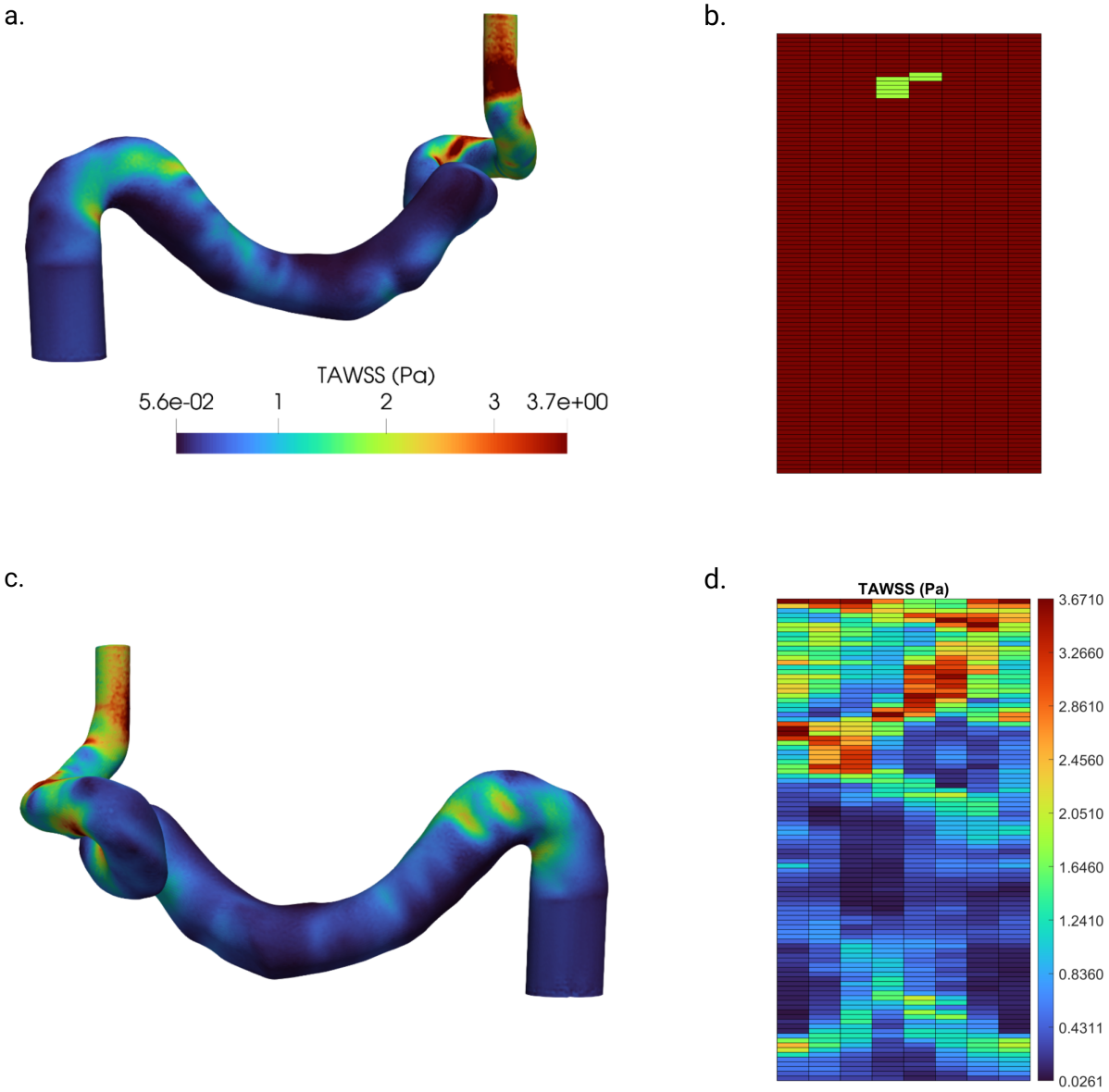

Figure E.10: TAWSS of Artery 3L in Pa. a) Medial view of the TAWSS. b) 2D map of the calcium presence. c) Lateral view of the TAWSS. d) 2D map of the TAWSS.

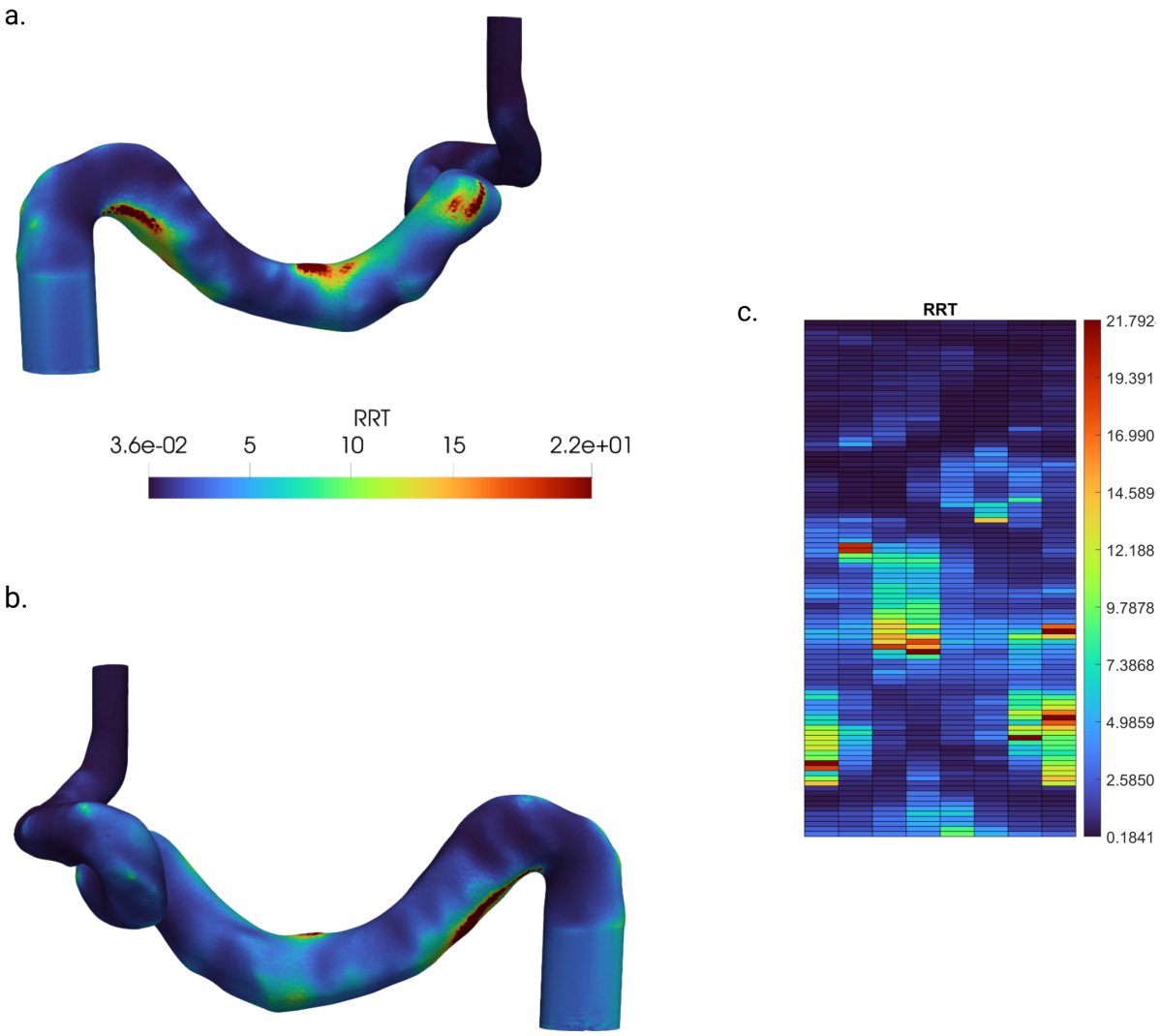

Figure E.11: RRT of Artery 3L. a) Medial view of the RRT. b) Lateral view of the RRT. c) 2D map of the RRT.

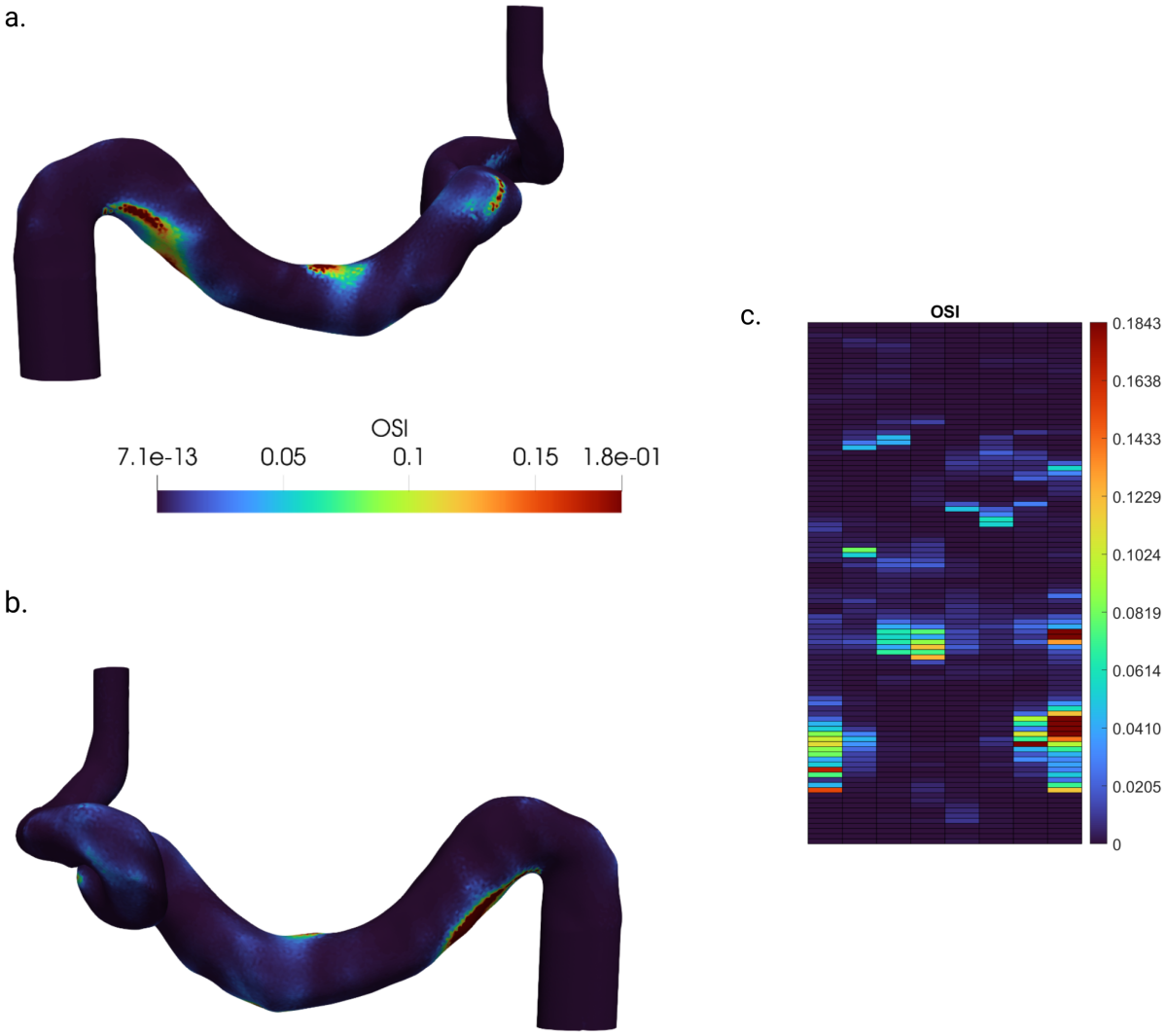

Figure E.12: OSI of Artery 3L. a) Medial view of the OSI. b) Lateral view of the OSI. c) 2D map of the OSI.

E.5. Artery 4R

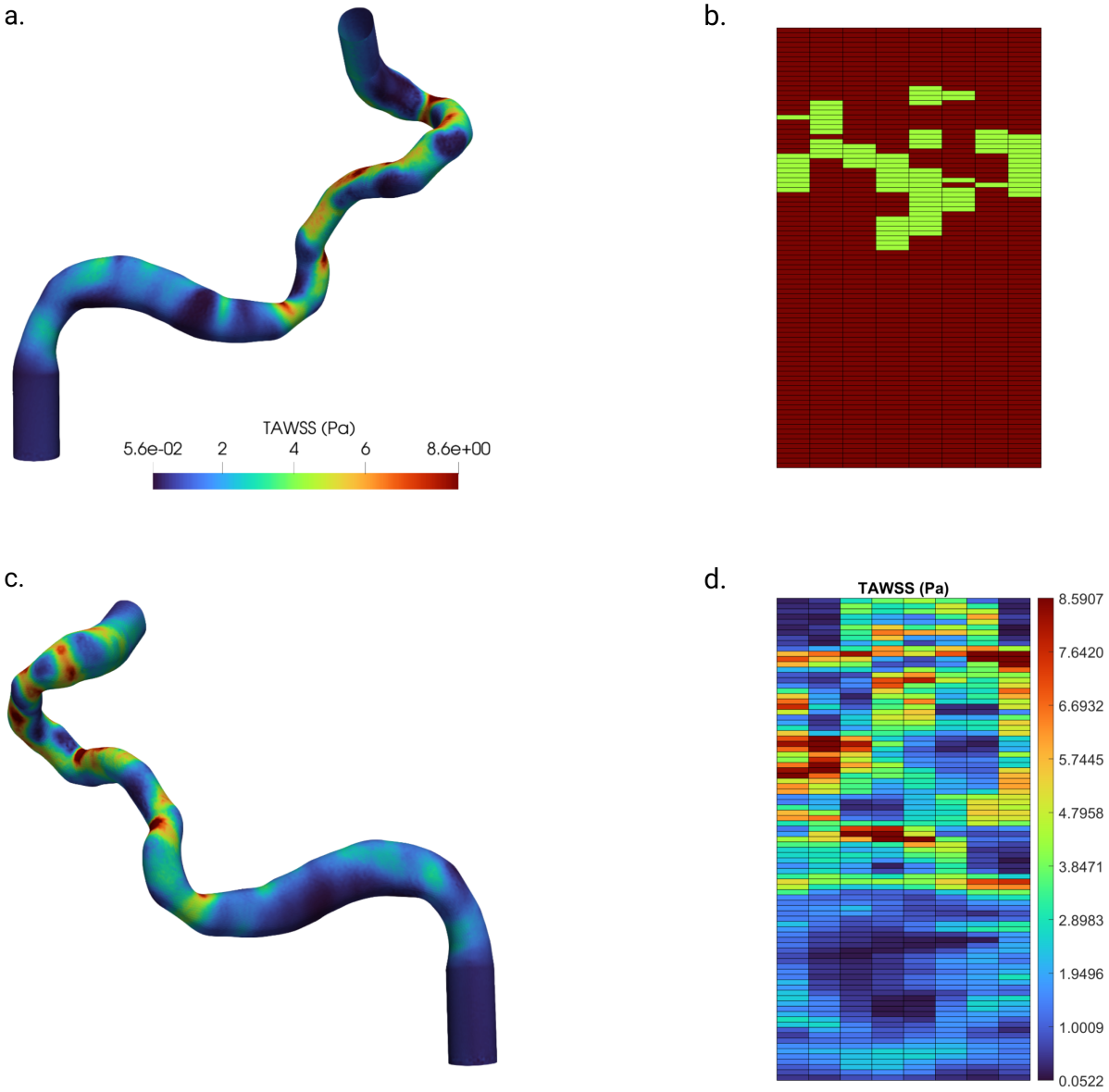

Figure E.13: TAWSS of Artery 4R in Pa. a) Lateral view of the TAWSS. b) 2D map of the calcium presence. c) Medial view of the TAWSS. d) 2D map of the TAWSS.

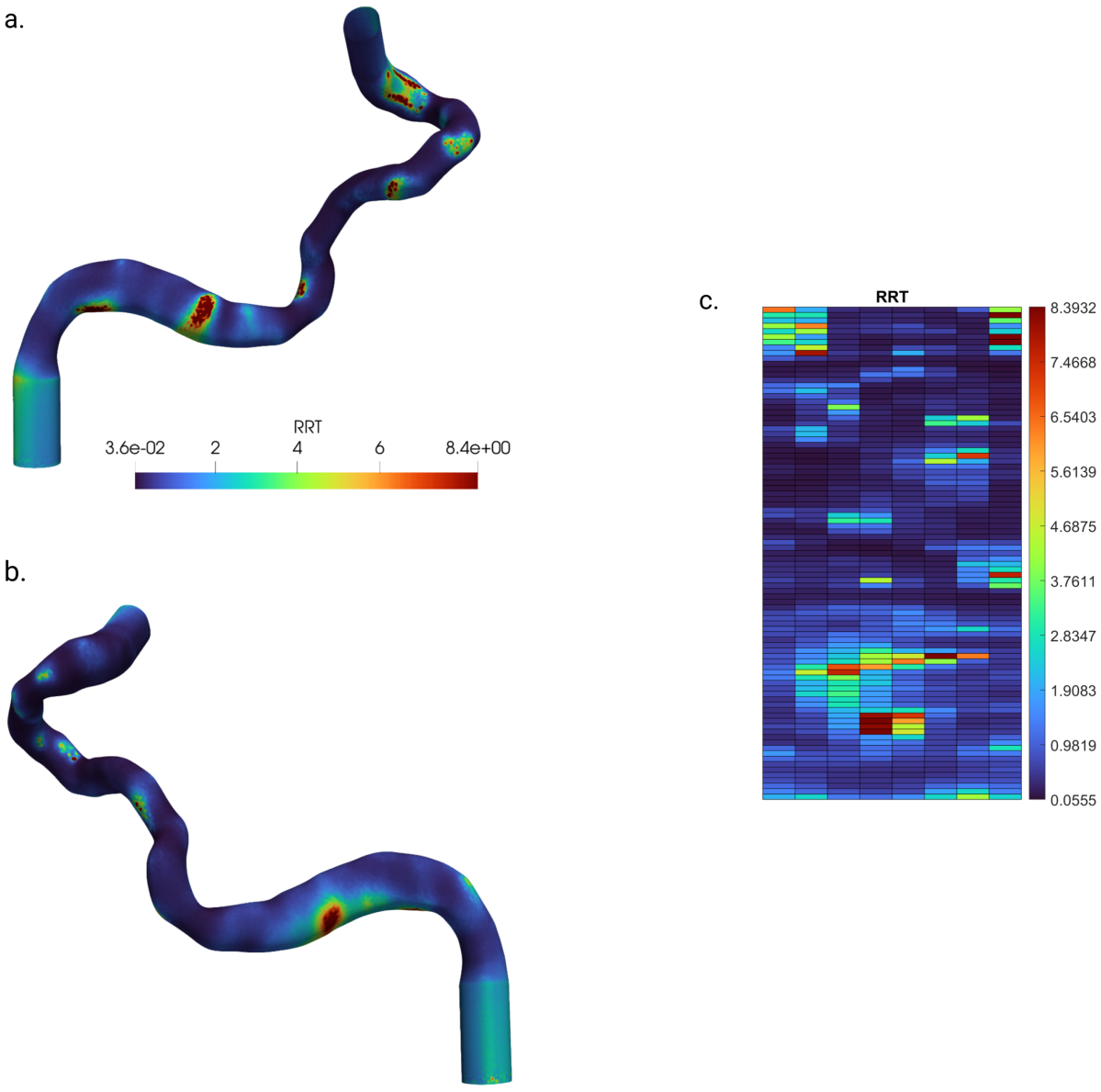

Figure E.14: RRT of Artery 4R. a) Lateral view of the RRT. b) Medial view of the RRT. c) 2D map of the RRT.

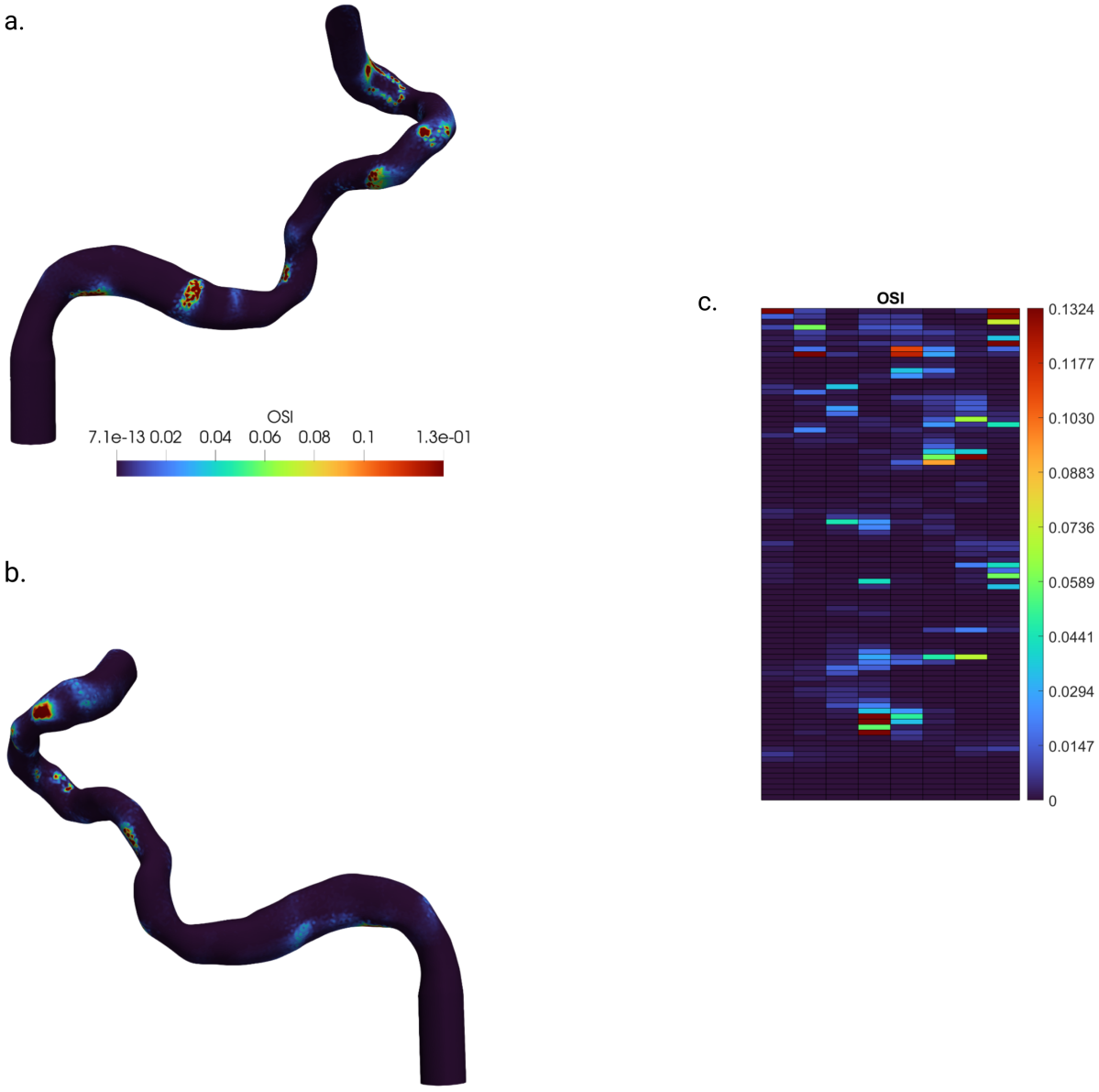

Figure E.15: OSI of Artery 4R. a) Lateral view of the OSI. b) Medial view of the OSI. c) 2D map of the OSI.

E.6. Artery 5L

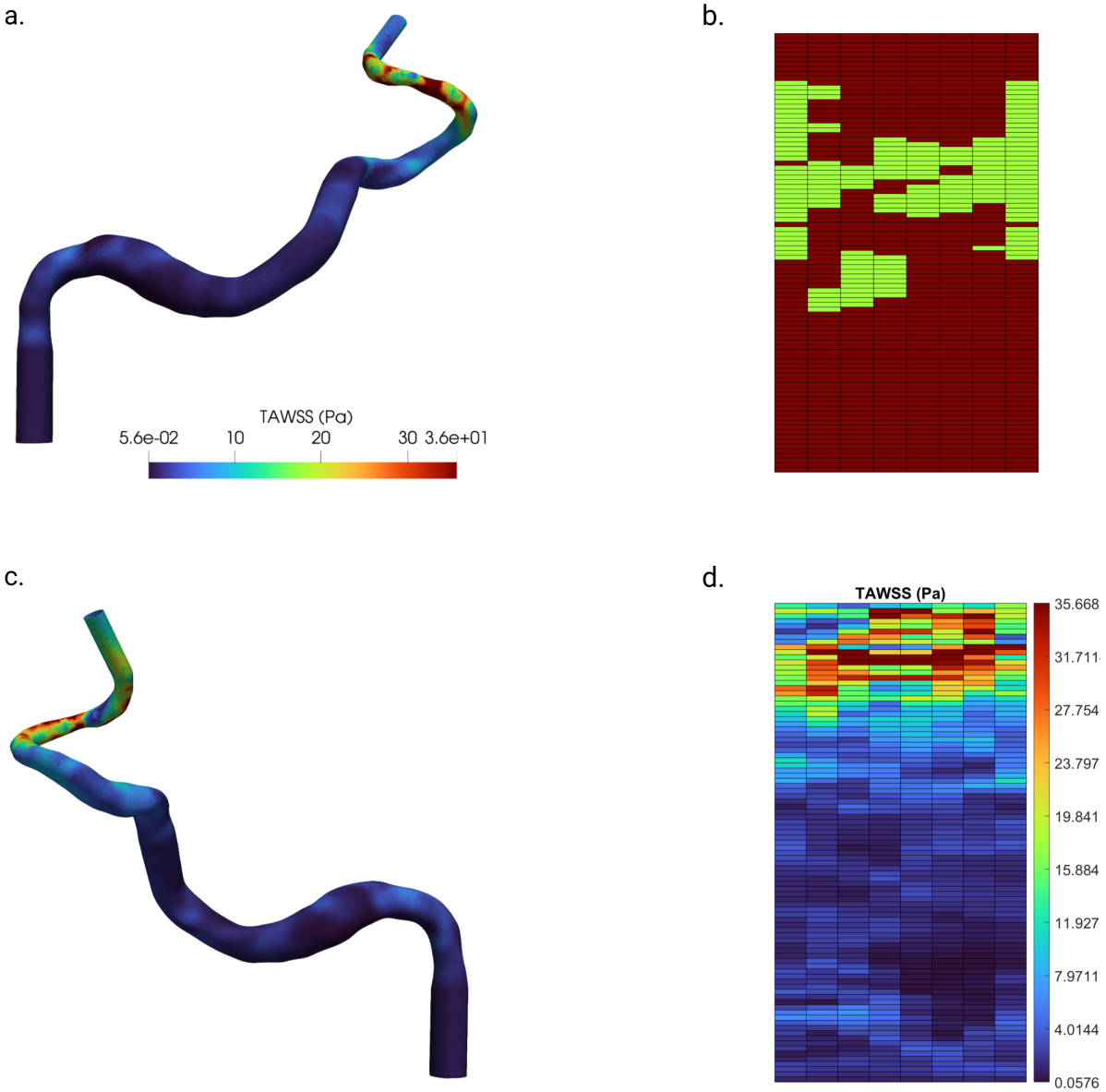

Figure E.16: TAWSS of Artery 5L in Pa. a) Medial view of the TAWSS. b) 2D map of the calcium presence. c) Lateral view of the TAWSS. d) 2D map of the TAWSS.

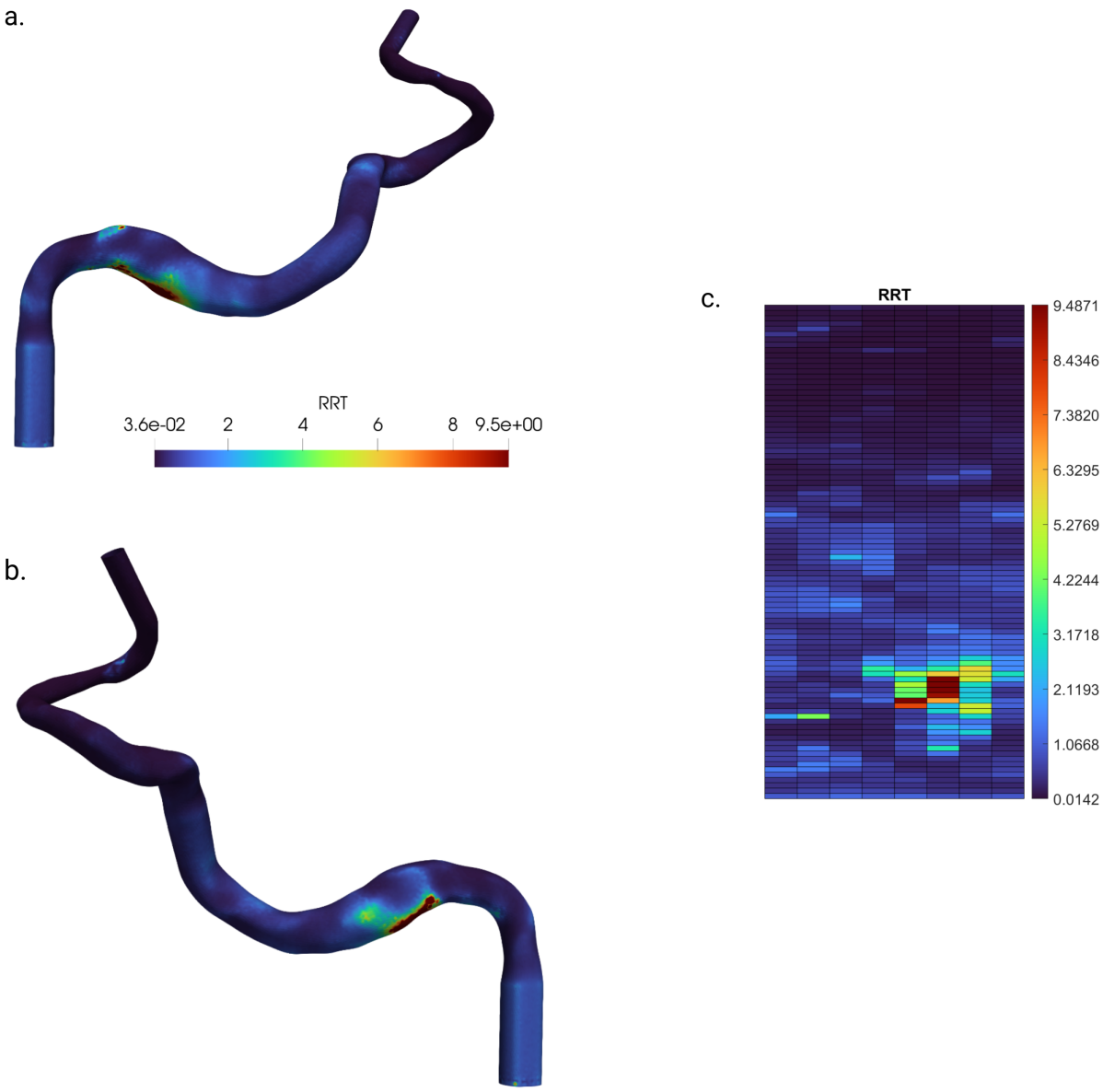

Figure E.17: RRT of Artery 5L. a) Medial view of the RRT. b) Lateral view of the RRT. c) 2D map of the RRT.

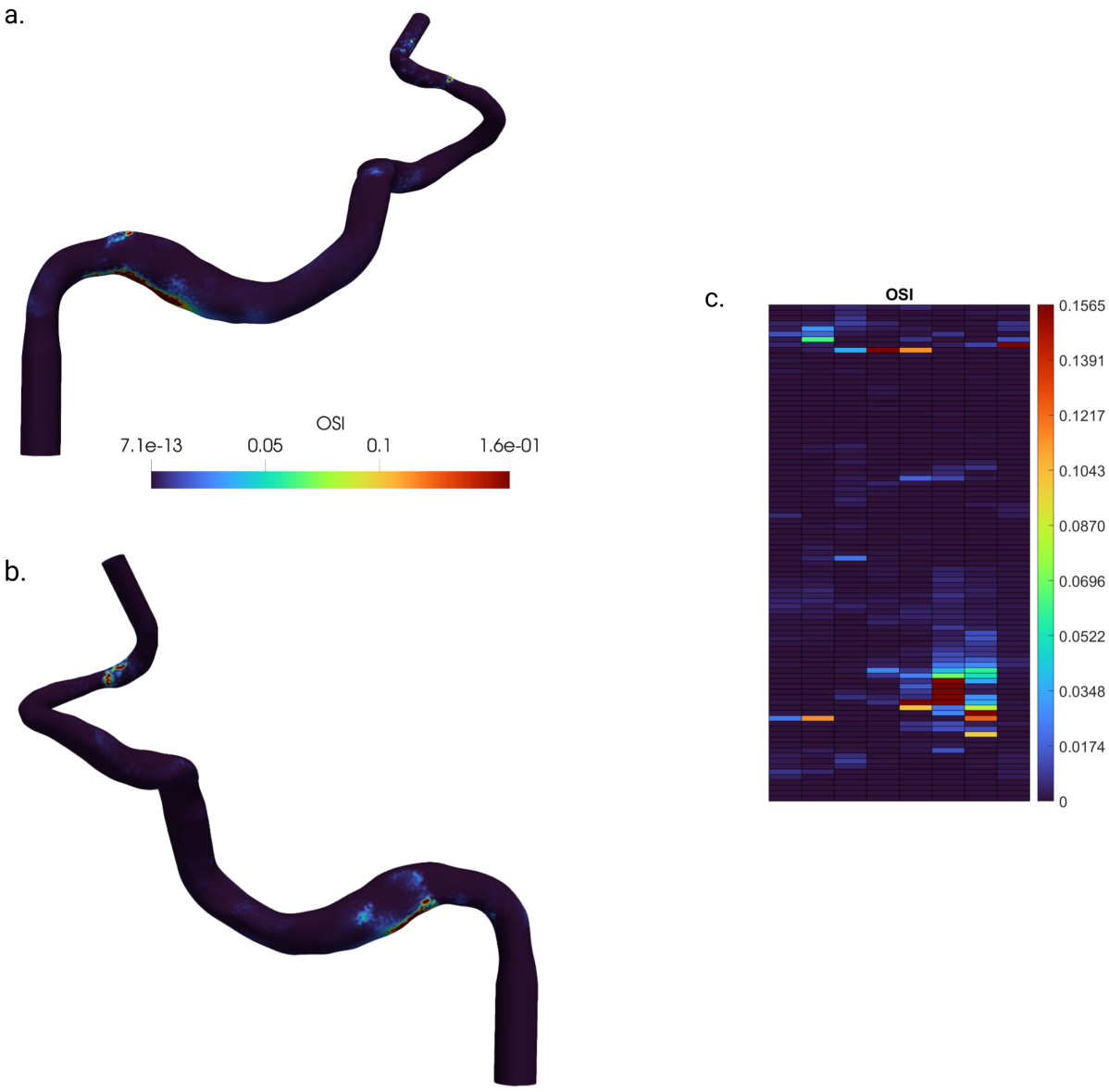

Figure E.18: OSI of Artery 5L. a) Medial view of the OSI. b) Lateral view of the OSI. c) 2D map of the OSI.

F

Segment analysis

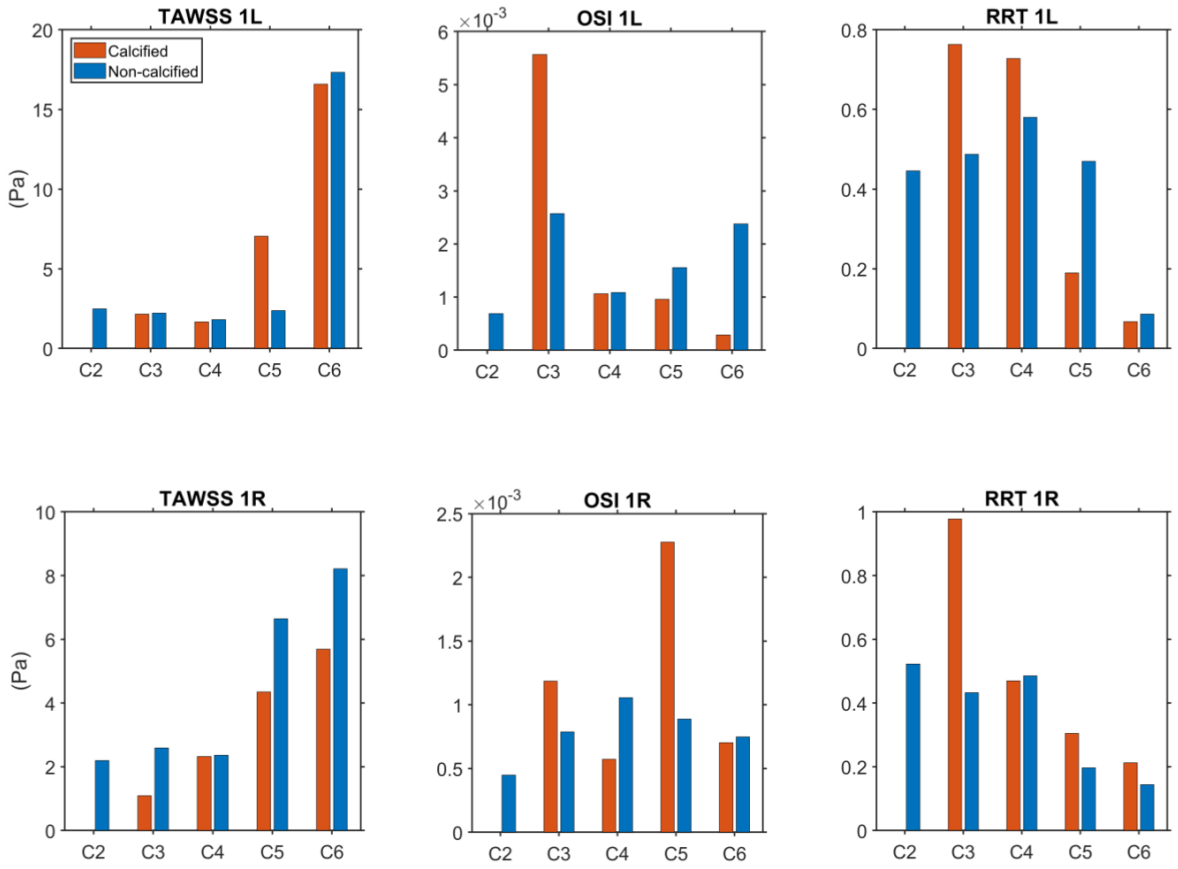

Figure F.1: TAWSS, OSI and RTT from the segment analysis, shown for the individual arteries. From top to bottom: Artery 1L and Artery 1R.

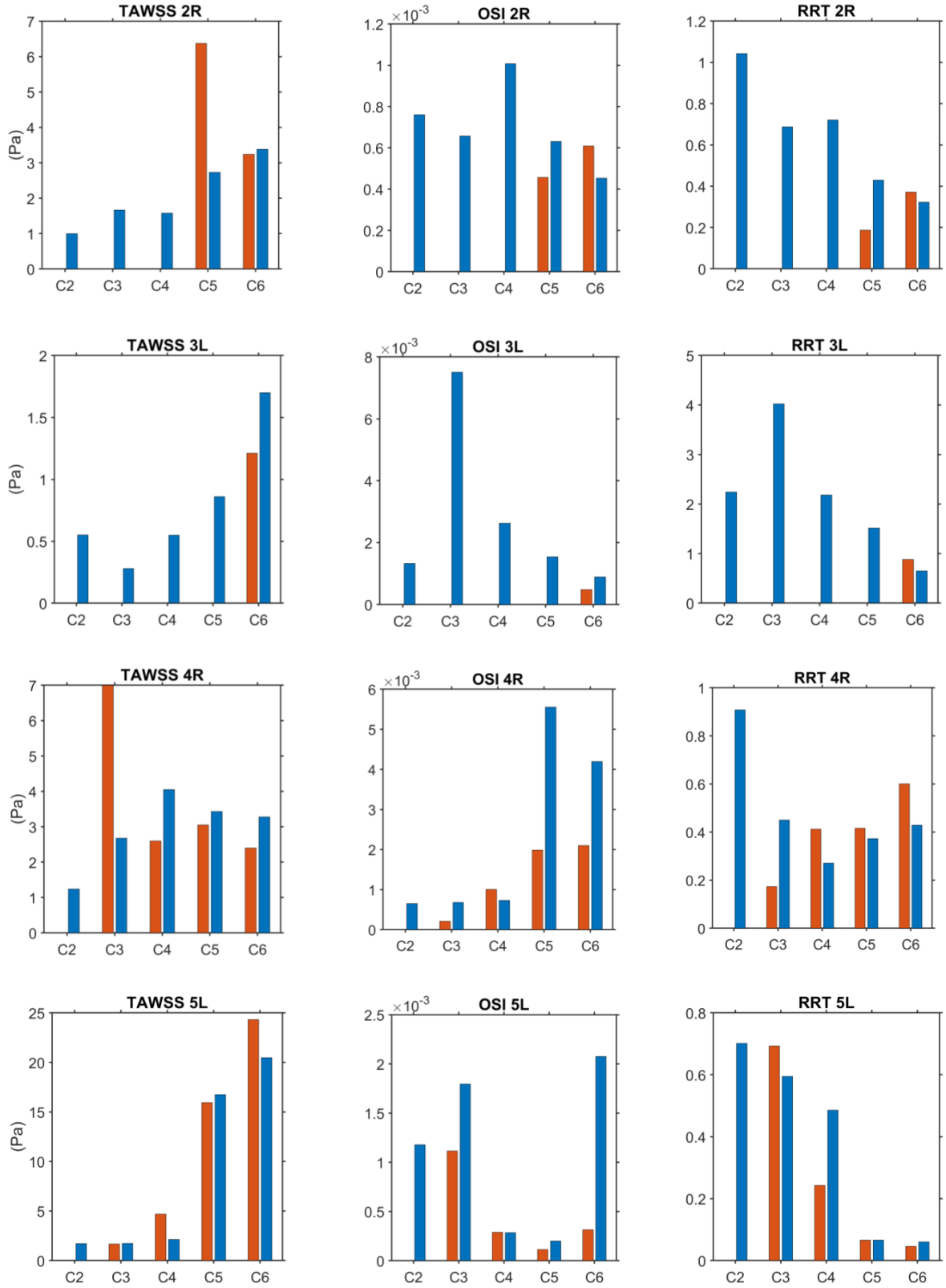

Figure F.2: TAWSS, OSI and RTT from the segment analysis, shown for the individual arteries. From top to bottom: Artery 2R, Artery 3L, Artery 4R, and Artery 5L.